

PREPARATION AND OPERATIONS OF THE MISSION PERFORMANCE
CENTRE (MPC) FOR THE COPERNICUS SENTINEL-3 MISSION

S3-A OLCI Cyclic Performance Report

Cycle No. 024

Start date: 27/10/2017

End date: 23/11/2017



*Mission
Performance
Centre*



Ref.: S3MPC.ACR.PR.01-024

Issue: 1.0

Date: 30/11/2017

Contract: 4000111836/14/I-LG

Customer: ESA	Document Ref.: S3MPC.ACR.PR.01-024
Contract No.: 4000111836/14/I-LG	Date: 30/11/2017
	Issue: 1.0

Project:	PREPARATION AND OPERATIONS OF THE MISSION PERFORMANCE CENTRE (MPC) FOR THE COPERNICUS SENTINEL-3 MISSION		
Title:	S3-A OLCI Cyclic Performance Report		
Author(s):	OLCI ESLs		
Approved by:	L. Bourg, OLCI ESL Coordinator	Authorized by	Frédéric Rouffi, OPT Technical Performance Manager
Distribution:	ESA, EUMETSAT, S3MPC consortium		
Accepted by ESA	S. Dransfeld, MPC Deputy TO for OPT P. Féménias, MPC TO		
Filename	S3MPC.ACR.PR.01-024 - i1r0 - OLCI Cyclic Report 024.docx		

Disclaimer

The work performed in the frame of this contract is carried out with funding by the European Union. The views expressed herein can in no way be taken to reflect the official opinion of either the European Union or the European Space Agency.





Table of content

TABLE OF CONTENT IV

LIST OF FIGURES V

1 INSTRUMENT MONITORING 1

1.1 CCD TEMPERATURES..... 1

1.2 RADIOMETRIC CALIBRATION 2

1.2.1 *Dark Offsets [OLCI-L1B-CV-230]* 4

1.2.2 *Instrument response and degradation modelling [OLCI-L1B-CV-250]*..... 9

1.2.3 *Ageing of nominal diffuser [OLCI-L1B-CV-240]*..... 17

1.2.4 *Updating of calibration ADF [OLCI-L1B-CV-260]* 20

1.2.5 *Radiometric Calibrations for sun azimuth angle dependency and Yaw Manoeuvres for Solar Diffuser on-orbit re-characterization [OLCI-L1B-CV-270 and OLCI-L1B-CV-280]*..... 21

1.3 SPECTRAL CALIBRATION [OLCI-L1B-CV-400]..... 21

1.4 SIGNAL TO NOISE ASSESSMENT [OLCI-L1B-CV-620] 24

1.4.1 *SNR from Radiometric calibration data*..... 24

1.4.2 *SNR from EO data*..... 27

1.5 GEOMETRIC CALIBRATION/VALIDATION 27

2 OLCI LEVEL 1 PRODUCT VALIDATION31

2.1 [OLCI-L1B-CV-300], [OLCI-L1B-CV-310] – RADIOMETRIC VALIDATION 31

2.1.1 *S3ETRAC Service* 31

2.1.2 *Radiometric validation with DIMITRI* 32

2.1.3 *Radiometric validation with OSCAR* 37

2.2 [OLCI-L1B-CV-320] – RADIOMETRIC VALIDATION WITH LEVEL 3 PRODUCTS..... 39

3 LEVEL 2 LAND PRODUCTS VALIDATION40

3.1 [OLCI-L2LRF-CV-300]..... 40

3.2 [OLCI-L2LRF-CV-410 & OLCI-L2LRF-CV-420] – CLOUD MASKING & SURFACE CLASSIFICATION FOR LAND PRODUCTS 48

4 LEVEL 2 WATER PRODUCTS VALIDATION52

4.1 [OLCI-L2-CV-210, OLCI-L2-CV-220] – VICARIOUS CALIBRATION OF THE NIR AND VIS BANDS..... 52

4.2 [OLCI-L2WLR-CV-300, OLCI-L2WLR-CV-310, OLCI-L2WLR-CV-32, OLCI-L2WLR-CV-330, OLCI-L2WLR-CV-340, OLCI-L2WLR-CV-350, OLCI-L2WLR-CV-360 AND OLCI-L2WLR-CV-370] – LEVEL 2 WATER-LEAVING REFLECTANCE PRODUCT VALIDATION..... 52

4.3 [OLCI-L2WLR-CV-510 & 520] – CLOUD MASKING & SURFACE CLASSIFICATION FOR WATER PRODUCTS 57

4.4 [OLCI-L2WLR-CV530] VALIDATION OF AEROSOL PRODUCT..... 60

4.4.1 *Validation by AERONET data*..... 60

4.4.2 *Verification by OLCI image analysis* 62

4.4.3 *References:*..... 65

4.5 [OLCI-L2WLR-CV-380] DEVELOPMENT OF CALIBRATION, PRODUCT AND SCIENCE ALGORITHMS..... 66


5 VALIDATION OF INTEGRATED WATER VAPOUR OVER LAND & WATER67

5.1 HIGHLIGHT 67

5.2 PREFACE 67

5.3 VISIBLE INSPECTION 67

5.4 QUANTITATIVE VALIDATION USING GNSS..... 70

	Sentinel-3 MPC S3-A OLCI Cyclic Performance Report Cycle No. 024	Ref.: S3MPC.ACR.PR.01-024 Issue: 1.0 Date: 30/11/2017 Page: v
--	---	--

5.5	QUANTITATIVE VALIDATION USING AERONET IWV RETRIEVALS – LAND	72
5.6	VALIDATION BY AERONET IWV RETRIEVALS – OCEAN	73
5.7	SUMMARY AND RECOMMENDATIONS	74
5.8	REFERENCES:	74
6	LEVEL 2 SYN PRODUCTS VALIDATION.....	76
6.1	[SYN-L2-CV-100]	76
7	EVENTS	77
8	APPENDIX A	78

List of Figures

Figure 1:	long term monitoring of CCD temperatures using minimum value (top), time averaged values (middle), and maximum value (bottom) provided in the annotations of the Radiometric Calibration Level 1 products, for the Shutter frames, all radiometric calibrations so far.	1
Figure 2:	Same as Figure 1 for diffuser frames.	2
Figure 3:	Sun azimuth angles during acquired Radiometric Calibrations (diffuser frame) on top of nominal yearly cycle (black curve). Diffuser 1 with diamonds, diffuser 2 with crosses, 2016 acquisitions in blue, 2017 in red.	3
Figure 4:	Sun geometry during radiometric Calibrations on top of characterization ones (diffuser frame)	3
Figure 5:	Dark Offset table for band Oa06 with (red) and without (black) HEP filtering (Radiometric Calibration of 22 July 2017). The strong HEP event near pixel 400 has been detected and removed by the HEP filtering.	4
Figure 6:	Dark Offset for band Oa1 (top) and Oa21 (bottom), all radiometric calibrations so far except the first one (orbit 183) for which the instrument was not thermally stable yet.	5
Figure 7:	map of periodic noise for the 5 cameras, for band Oa21. X-axis is detector number (East part, from 540 to 740, where the periodic noise occurs), Y-axis is the orbit number. The counts have been corrected from the west detectors mean value (not affected by periodic noise) in order to remove mean level gaps and consequently to have a better visualisation of the long term evolution of the periodic noise structure. Periodic noise amplitude is high in camera 2, 3 and 4. It is lower in camera 4 and small in camera 1.	6
Figure 8:	same as Figure 7 for smear band.	6
Figure 9:	Dark Offset levels for smear band camera 5, for (left plot) first 30 WEST detectors including virtual and blind pixels, (right plot) last 30 EAST detectors including blind pixels. The colour of the curves is linked to the orbit number, from the beginning of the mission in black, to the last CALs in red. We see on the right plot that the shape of the PN for the CALs at orbit ≥ 8736 has been strongly modified by the reset of the OLCI instrument of orbit 8666 (Cycle #23). As a consequence, the global mean level of the dark offset is impacted by this change of PN, through the OCL convergence, as illustrated in the left plot.	7


	<p>Sentinel-3 MPC</p> <p>S3-A OLCI Cyclic Performance Report</p> <p>Cycle No. 024</p>	<p>Ref.: S3MPC.ACR.PR.01-024</p> <p>Issue: 1.0</p> <p>Date: 30/11/2017</p> <p>Page: vi</p>
--	--	--

Figure 10: Dark Current for band Oa1 (top) and Oa21 (bottom), all radiometric calibrations so far except the first one (orbit 183) for which the instrument was not thermally stable yet. ----- 8

Figure 11: left column: ACT mean on 400 first detectors of Dark Current coefficients for spectral band Oa01 (top) and Oa21 (bottom). Right column: same as left column but for Standard deviation instead of mean. We see an increase of the DC level as a function of time especially for band Oa21. A possible explanation could be the increase of the number of hot pixels which is more important in Oa21 because this band is made of more CCD lines than band Oa01 and thus receives more cosmic rays impacts. It is known that cosmic rays degrade the structure of the CCD, generating more and more hot pixels at long term scales. ----- 8

Figure 12: Gain Coefficients for band Oa1 (top) and Oa21 (bottom), all diffuser 1 radiometric calibrations so far except the first one (orbit 183) for which the instrument was not thermally stable yet. ----- 9

Figure 13: camera averaged gain relative evolution with respect to “best geometry” calibration (22/11/2016), as a function of elapsed time since launch; one curve for each band (see colour code on plots), one plot for each module. The star tracker anomaly fix (6/04/16) is represented by a vertical red dashed line. -----10

Figure 14: RMS performance of the Gain Model of current Processing Baseline as a function of orbit.---11

Figure 15: RMS performance of the Gain Model of previous Processing Baseline as a function of orbit. -11

Figure 16: Camera-averaged instrument evolution since channel programming change (25/04/2016) and up to most recent calibration (22/11/2017) versus wavelength.-----12

Figure 17: For the 5 cameras: Evolution model performance, as camera-average and standard deviation of ratio of Model over Data vs. wavelength, for each orbit of the test dataset, including 6 calibration in extrapolation, with a colour code for each calibration from blue (oldest) to red (most recent).-----13

Figure 18: Evolution model performance, as ratio of Model over Data vs. pixels, all cameras side by side, over the whole current calibration dataset (since instrument programming update), including 6 calibrations in extrapolation, channels Oa1 to Oa6. -----14

Figure 19: same as Figure 14 for channels Oa7 to Oa14. -----15

Figure 20: same as Figure 18 for channels Oa15 to Oa21.-----16

Figure 21: diffuser 1 ageing for spectral band Oa01. We see strong ACT low frequency structures that are due to residual of BRDF modelling. -----17

Figure 22: same as Figure 21 for spectral band Oa16. We use this band in order to normalize other bands and remove the ACT structures due to residual of BRDF modelling. Normalized curve for spectral band Oa01 is presented in Figure 23. -----18

Figure 23: same as Figure 21 after normalization by band Oa16. Ageing of the diffuser 1 is now visible in the 5 cameras.-----18

Figure 24: Diffuser 1 ageing as a function of wavelength (or spectral band). Ageing is visible in spectral band #1 to #5. -----19


	Sentinel-3 MPC S3-A OLCI Cyclic Performance Report Cycle No. 024	Ref.: S3MPC.ACR.PR.01-024 Issue: 1.0 Date: 30/11/2017 Page: vii
--	---	--

Figure 25: Camera averaged ageing (normalized by band Oa16) as a function of time. Linear fit for each camera is plotted. The slope (% loss per year) and the correlation coefficient -----19

Figure 26: Slope of ageing fit (% of loss per exposure) vs wavelengths, using all the available ageing sequence at the time of the current cycle (black curve) and at the time of cycle #20 (red curve) -----20

Figure 27: across track spectral calibration for all S02/S03 sequences since the beginning of the mission. Top plot is spectral line 1, middle plot is spectral line 2 and bottom plot spectral line 3. -----22

Figure 28: camera averaged spectral calibration as a function of orbit number (all spectral S02/S03 calibrations since the beginning of the mission are included). Top plot is spectral line 1, middle plot is spectral line 2 and bottom plot spectral line 3. -----23

Figure 29: spectral calibration as a function of time derived from all S09 sequences. From left to right column: the 5 cameras. From top to bottom: Used absorption line: 485 nm, 656 nm, 770 nm and 854 nm. -----23

Figure 30: Signal to Noise ratio as a function of the spectral band for the 5 cameras. These results have been computed from radiometric calibration data. All calibrations except first one (orbit 183) are presents with the colours corresponding to the orbit number (see legend). The SNR is very stable with time: the curves for all orbits are almost superimposed. The dashed curve is the ESA requirement. ----25

Figure 31: long-term stability of the SNR estimates from Calibration data, example of channel Oa1. ----26

Figure 32: histograms of geolocation errors for the along-track (left) and across-track (right) directions, examples of 28/10/2017 (top) and 22/11/2017 (bottom).-----28

Figure 33: georeferencing error in along-track (left) and across-track (right) directions for all the GCPs, examples of 28/10/2017 (top) and 22/11/2017 (bottom).-----29

Figure 34: time series of geolocation errors for the along-track (blue) and across-track (red) directions over 18.7 months. -----30

Figure 35: summary of S3ETRAC products generation for OLCI (number of OLCI L1 products Ingested, yellow – number of S3ETRAC extracted products generated, blue – number of S3ETRAC runs without generation of output product (data not meeting selection requirements), green – number of runs ending in error, red, one plot per site type). -----32

Figure 36: Time-series of the elementary ratios (observed/simulated) signal from S3A/OLCI for (top to bottom) bands Oa03, Oa8 and Oa17 respectively over Six PICS Cal/Val sites. Dashed-green and orange lines indicate the 2% and 5% respectively. Error bars indicate the desert methodology uncertainty. ----33

Figure 37: The estimated gain values for S3A/OLCI over the 6 PICS sites identified by CEOS over the period April 2016 – October 2017 as a function of wavelength. Dashed-green and orange lines indicate the 2% and 5% respectively. Error bars indicate the desert methodology uncertainty. -----34

Figure 38: Time-series of the elementary ratios (observed/simulated) signal from (black) S2A/MSI, (blue) S3A/OLCI, and (Cyan) MODIS-A for band Oa17 (865nm) over the LIBYA4 site. Dashed-green and orange lines indicate the 2% and 5% respectively. Error bars indicate the desert methodology uncertainty. ----35


	Sentinel-3 MPC S3-A OLCI Cyclic Performance Report Cycle No. 024	Ref.: S3MPC.ACR.PR.01-024 Issue: 1.0 Date: 30/11/2017 Page: viii
--	---	---

Figure 39: The estimated gain values (observed-signal /simulated-signal) averaged over different period from different sensors over PICS as function of wavelength. The number of used-acquisitions for each sensor within the period July 2015-October 2017 is indicated in the plot-legend. -----36

Figure 40: The estimated gain values for S3A/OLCI over the 6 Ocean CalVal sites (Atl-NW_Optimum, Atl-SW_Optimum, Pac-NE_Optimum, Pac-NW_Optimum, SPG_Optimum and SIO_Optimum) over the period December 2016 – October 2017 as a function of wavelength. Dashed-green, and orange lines indicate the 2%, 5% respectively. Error bars indicate the methodology uncertainty. -----36

Figure 41: The estimated gain values for S3A/OLCI from Glint, Rayleigh and PICS over the period April 2016 – November 2017 for PICS and December 2016-October 2017 for Glint and December 2016-November 2017 for Rayleigh methods as a function of wavelength. We use the gain value of Oa8 from PICS method as reference gain for Glint. Dashed-green and orange lines indicate the 2% and 5% respectively. Error bars indicate the methods uncertainties.-----37

Figure 42: OSCAR Rayleigh Calibration results: weighted average over all sites and standard deviation for (a) period Jan 2017 till Sept 2017 and (b) July 2017 till Sept 2017 -----38

Figure 43: RGB composites of the study sites. A) France B) Los Angles C) Queensland, Australia D) Denmark E) Greenland F) Congo G) Rondonia -----40

Figure 44: A) RGB image of the River Rhone, France (43°32'02" N, 4°43'06" E). B) Inland water flagged pixels. C) Cloud flagged Pixels. D) Pixels classified as both inland water and cloud.-----42

Figure 45: RGB and OTCI bands for Queensland Australia (17°26'04" S, 143°47'15" E).-----43

Figure 46: A) Histogram of OTCI values for cloud pixels. B) Histogram of OTCI values for bare soil pixels.43

Figure 47: Spectral signals of the different classifications within the image Queensland Australia (17°26'04" S, 143°47'15" E).-----44

Figure 48: A) RGB composite (39°39'01" N, 115°54'46" W) B) Cloud mask C) Location of Pins. D) Spectral signals of the different pins. -----45

Figure 49: RGB and OTCI bands for the Congo (0°55'28" N, 32°37'17" E). Within the RGB image the Cloud, Cloud_ambiguous and Cloud_edge masks have been turned on.-----45

Figure 50: A) Histogram of OTCI values for cloud pixels. B) Histogram of OTCI values for forest pixels. C) Histogram of OGVI values for cloud pixels. D) Histogram of OGVI values for forest pixels-----46

Figure 51: Spectral signals taken from the ROIs identified in Figure 7.-----46

Figure 52: RGB image of the ROI in Rondonia, Brazil (10°58'10" S, 64°00'12" W). -----47

Figure 53: A) Histogram of OTCI values for cloud pixels. B) Histogram of OTCI values for forest pixels. C) Histogram of OGVI values for cloud pixels. D) Histogram of OGVI values for forest pixels.-----47

Figure 54: Spectral signals of a cloud and forest pixel. -----48

Figure 55: spatial distribution of the PixBox validation dataset samples -----49

Figure 56: PixBox validation dataset samples Cloudiness classification overview-----49

Figure 57: Validation dataset Confusion Matrix for all underlying surfaces -----50


	Sentinel-3 MPC S3-A OLCI Cyclic Performance Report Cycle No. 024	Ref.: S3MPC.ACR.PR.01-024 Issue: 1.0 Date: 30/11/2017 Page: ix
--	---	---

Figure 58: Validation dataset Confusion Matrix for Land underlying surfaces -----51

Figure 59: Scatter plots of OLCI versus in situ radiometry (FR data) -----53

Figure 60: Scatter plots of OLCI versus in situ radiometry (RR data) -----54

Figure 61: OLCI and AERONET-OC radiometric time series on WaveCIS station. -----57

Figure 62: spatial distribution of the PixBox validation dataset samples -----58

Figure 63: PixBox validation dataset samples Cloudiness classification overview -----58

Figure 64: Validation dataset Confusion Matrix for all underlying surfaces -----59

Figure 65: Validation dataset Confusion Matrix for Water underlying surfaces -----60

Figure 66 Map of the U.S.A., showing the used AERONET-OC stations (red bullets) -----61

Figure 67: Comparison of AERONET and OLCI derived aerosol optical thickness at 865 nm (left) and Ångström coefficient (right); match-ups only taken when no clouds in the vicinity of 30 km. -----61

Figure 68: AERONET MAN measurements from ship cruises (red bullets). -----62

Figure 69: Comparison of AERONET and OLCI derived aerosol optical thickness at 865 nm (left) and Ångström coefficient (right). The error bars indicate the variability within a 30 km radius (OLCI) the and a 1h window (AERONET) -----62

Figure 70: OLCI scene from 6th of October 2017, arrows are pointing to study areas -----63

Figure 71: OLCI scene from 6th of October 2017 and derived properties: T865 (left), O2 A-band (middle), RGB-image (right); profile plots of T865, A865 and O2 A-band (L761/L753); see also Figure 70 for geo-location. -----64

Figure 72: OLCI scene from 6th of October 2017 and derived properties: T865 (left), O2 A-band (middle), RGB-image (right); profile plots of T865, O2 A-band (L761/L753); -----65

Figure 73: IWV, estimated from OLCI at 03/March/2017, above the Pacific, south-west of Baja California. Left: IWV from OLCI, middle: ECMWF Analysis, right: RGB. The color coding ranges from 0 kg/m² (blue) to 60 kg/m² (black). Land and clouds are masked out (black and white, resp.) -----68

Figure 74: OLCI scene from 19.10.2016 (19:05), marked in the white box (left), IWV derived from OLCI (middle), IWV estimated by ECMWF (right)-----69

Figure 75: OLCI scene from 19.10.2016 (19:05), IWV product of marked scene (left, see also figure 4), RGB image of a selected region above the Rocky Mountains (left), IWV field above the Rocky Mountains, see the lee waves in lower part of the image (right)-----69

Figure 76 : Transect along the lee waves (see Figure 75). -----70

Figure 77: Position of the GNSS stations used for the IWV validation. -----70

Figure 78: Scatter plot of the IWV products, derived from OLCI and from GNSS measurements. -----71

Figure 79: Scatter plot of the IWV products, derived from OLCI and from US GNSS measurements. -----71

Figure 80: Position of the AERONET stations used for the IWV validation. -----72


	<p>Sentinel-3 MPC</p> <p>S3-A OLCI Cyclic Performance Report</p> <p>Cycle No. 024</p>	<p>Ref.: S3MPC.ACR.PR.01-024</p> <p>Issue: 1.0</p> <p>Date: 30/11/2017</p> <p>Page: x</p>
--	--	---

Figure 81 OLCI IWV against AERONET IWV retrievals for the sites displayed in Figure 80.-----72

Figure 82: Position of the AERONET sites used for the IWV validation.-----73

Figure 83: OLCI IWV against AERONET IWV retrievals for the sites displayed in Figure 82.-----74



1 Instrument monitoring

1.1 CCD temperatures

The monitoring of the CCD temperatures is based on MPMF data extractions not yet operational. In the meantime, we monitor the CCD temperatures on the long-term using Radiometric Calibration Annotations (see Figure 1). Variations are very small (0.09 C peak-to-peak) and no trend can be identified. Data from current cycle (rightmost data points) do not show any specificity.

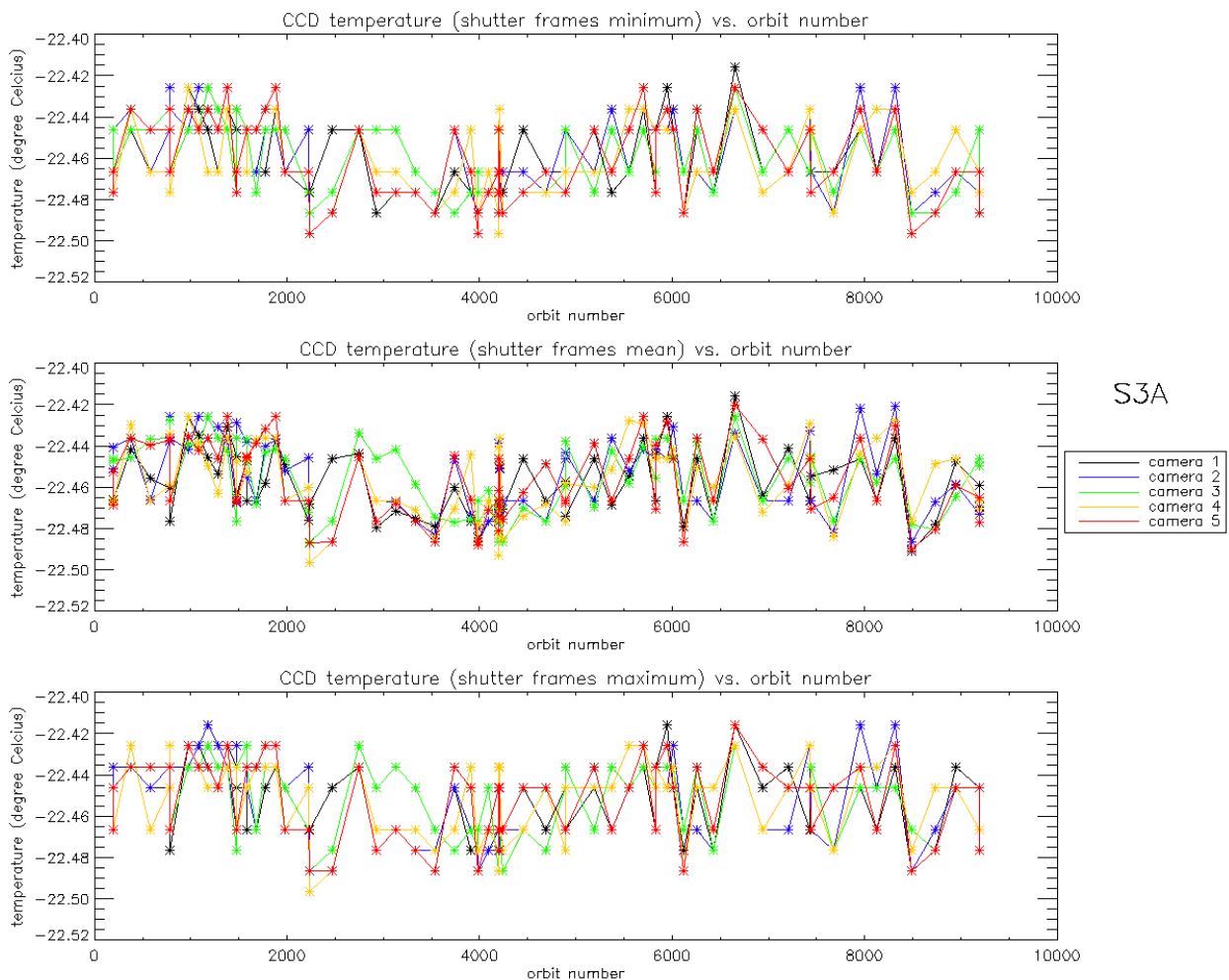


Figure 1: long term monitoring of CCD temperatures using minimum value (top), time averaged values (middle), and maximum value (bottom) provided in the annotations of the Radiometric Calibration Level 1 products, for the Shutter frames, all radiometric calibrations so far.

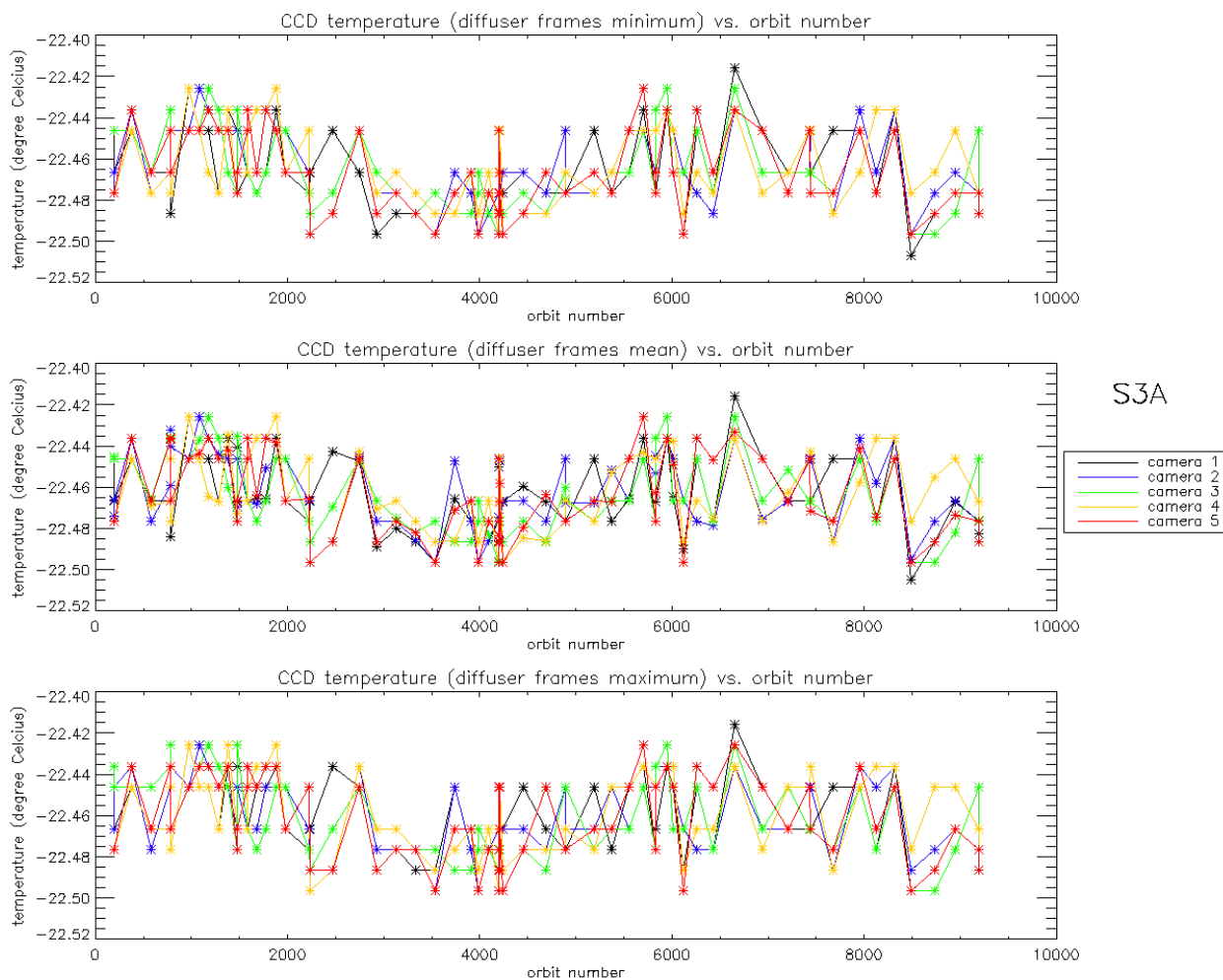


Figure 2: Same as Figure 1 for diffuser frames.

1.2 Radiometric Calibration

Three OLCI Radiometric Calibration Sequences have been acquired during Cycle 024:

- ❖ S01 sequence (diffuser 1) on 05/11/2017 04:10 to 04:11 (absolute orbit 8946)
- ❖ S04 sequence (diffuser 1) on 22/11/2017 08:33 to 08:35 (absolute orbit 9191)
- ❖ S05 sequence (diffuser 2) on 22/11/2017 10:14 to 10:16 (absolute orbit 9192)

The acquired Sun azimuth angles are presented on below, on top of the nominal values without Yaw Manoeuvre (i.e. with nominal Yaw Steering control of the satellite).

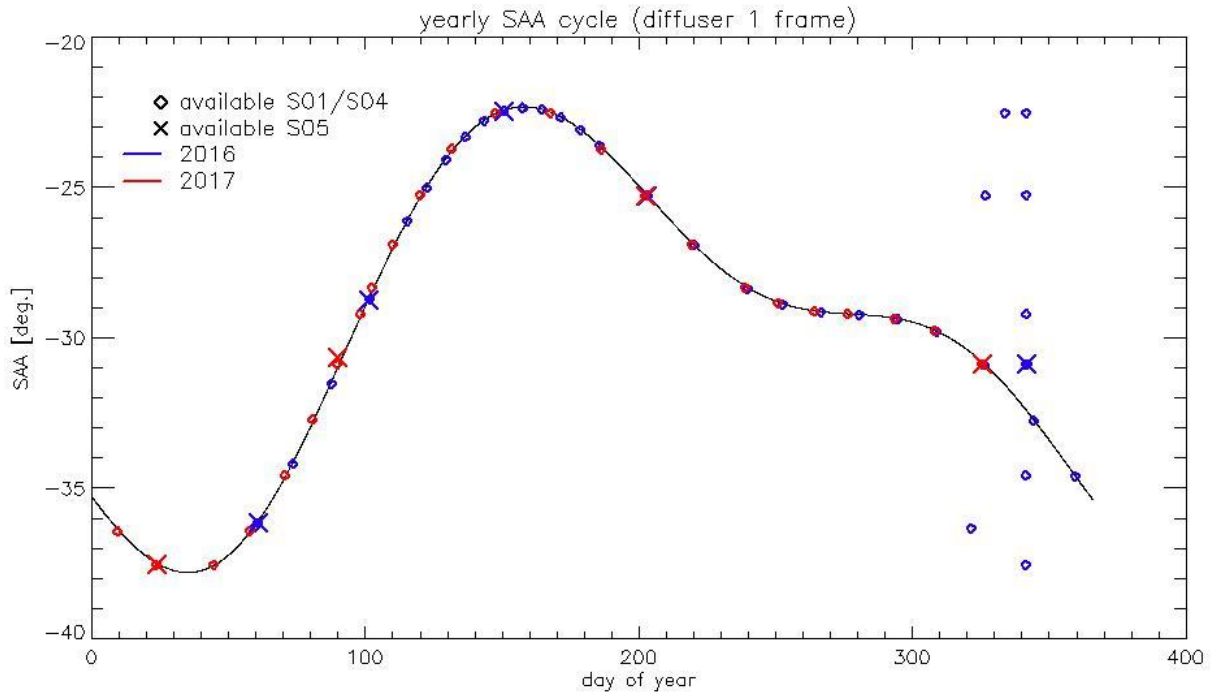


Figure 3: Sun azimuth angles during acquired Radiometric Calibrations (diffuser frame) on top of nominal yearly cycle (black curve). Diffuser 1 with diamonds, diffuser 2 with crosses, 2016 acquisitions in blue, 2017 in red.

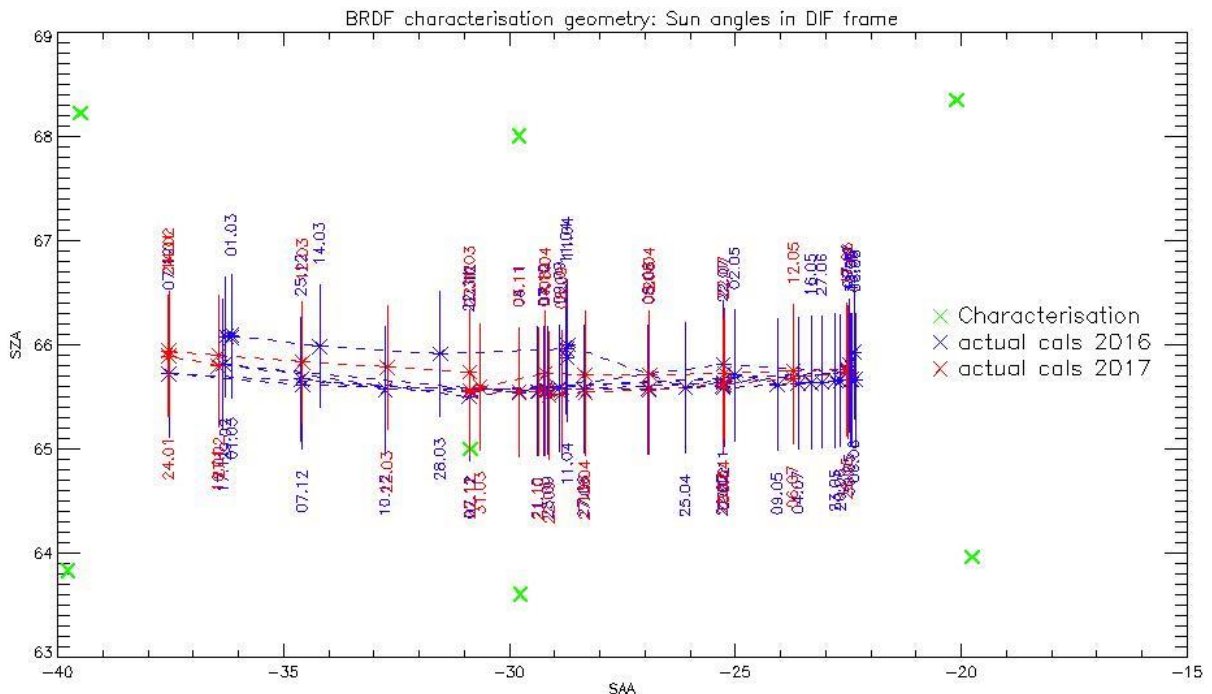


Figure 4: Sun geometry during radiometric Calibrations on top of characterization ones (diffuser frame)

This section presents the overall monitoring of the parameters derived from radiometric calibration data and highlights, if present, specificity of current cycle data.

1.2.1 Dark Offsets [OLCI-L1B-CV-230]

Note about the High Energy Particles:

The filtering of High Energy Particle (HEP) events from radiometric calibration data has been implemented (for shutter frames only) in a post processor, allowing generating Dark Offset and Dark Current tables computed on filtered data. The post-processor starts from IPF intermediate data (corrected counts), applies the HEP detection and filtering and finally computes the Dark Offset and Dark Current tables the same way as IPF. An example of the impact of HEP filtering is given in Figure 5.

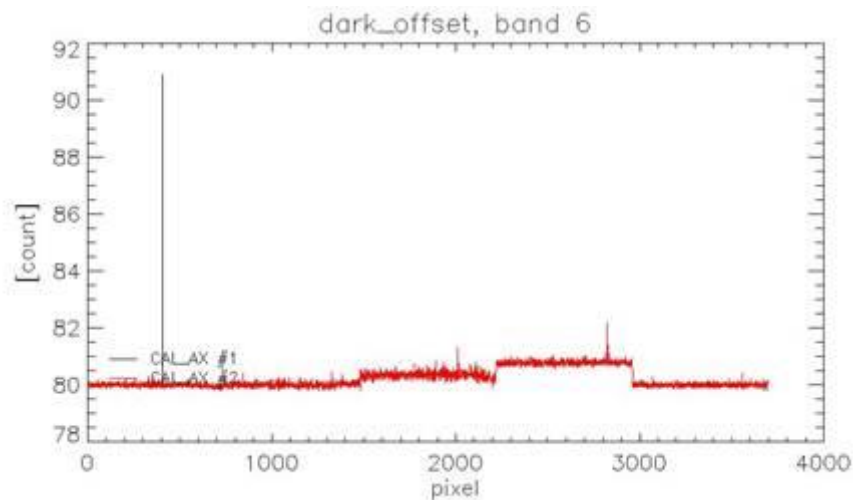


Figure 5: Dark Offset table for band Oa06 with (red) and without (black) HEP filtering (Radiometric Calibration of 22 July 2017). The strong HEP event near pixel 400 has been detected and removed by the HEP filtering.

All results presented below in this section have been obtained using the HEP filtered Dark Offset and Dark Current tables.

Dark offsets

Dark offsets are continuously affected by the global offset induced by the Periodic Noise on the OCL convergence. Current Cycle calibrations are affected the same way as others. The amplitude of the shift varies with band and camera from virtually nothing (e.g. camera 2, band Oa1) to up to 5 counts (Oa21, camera 3). The Periodic Noise itself comes on top of the global shift with its known signature: high frequency oscillations with a rapid damp. This effect remains more or less stable with time in terms of amplitude, frequency and decay length, but its phase varies with time, introducing the global offset mentioned above.



Sentinel-3 MPC
S3-A OLCI Cyclic Performance Report
Cycle No. 024

Ref.: S3MPC.ACR.PR.01-024
Issue: 1.0
Date: 30/11/2017
Page: 5

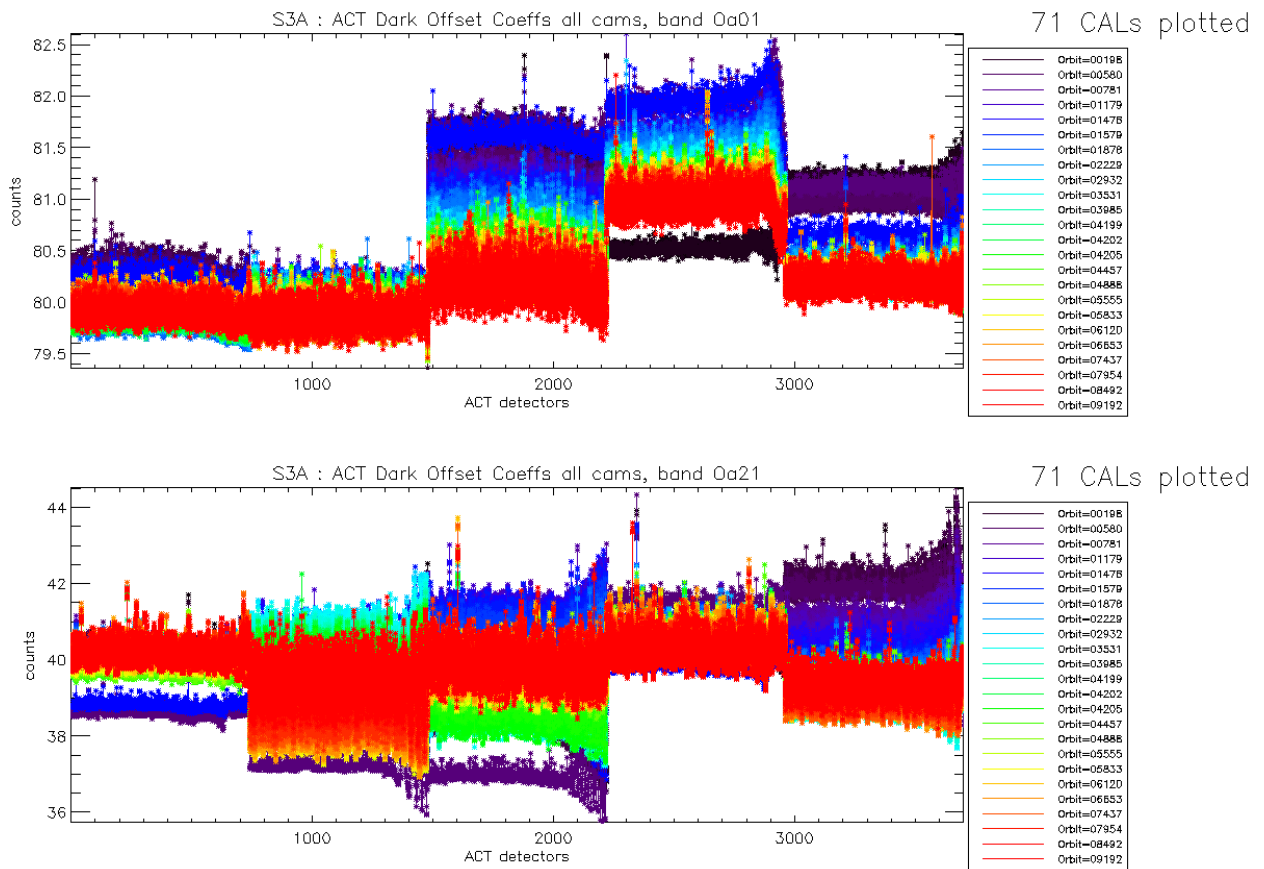


Figure 6: Dark Offset for band Oa1 (top) and Oa21 (bottom), all radiometric calibrations so far except the first one (orbit 183) for which the instrument was not thermally stable yet.

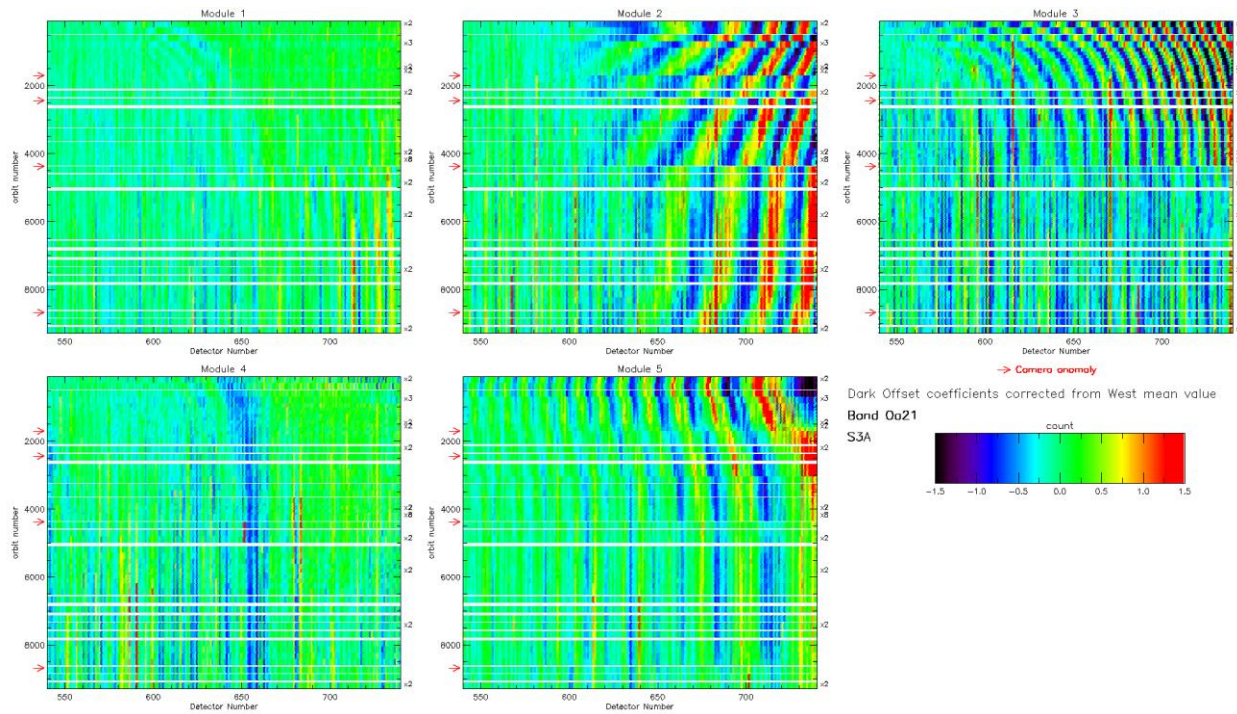


Figure 7: map of periodic noise for the 5 cameras, for band Oa21. X-axis is detector number (East part, from 540 to 740, where the periodic noise occurs), Y-axis is the orbit number. The counts have been corrected from the west detectors mean value (not affected by periodic noise) in order to remove mean level gaps and consequently to have a better visualisation of the long term evolution of the periodic noise structure. Periodic noise amplitude is high in camera 2, 3 and 4. It is lower in camera 4 and small in camera 1.

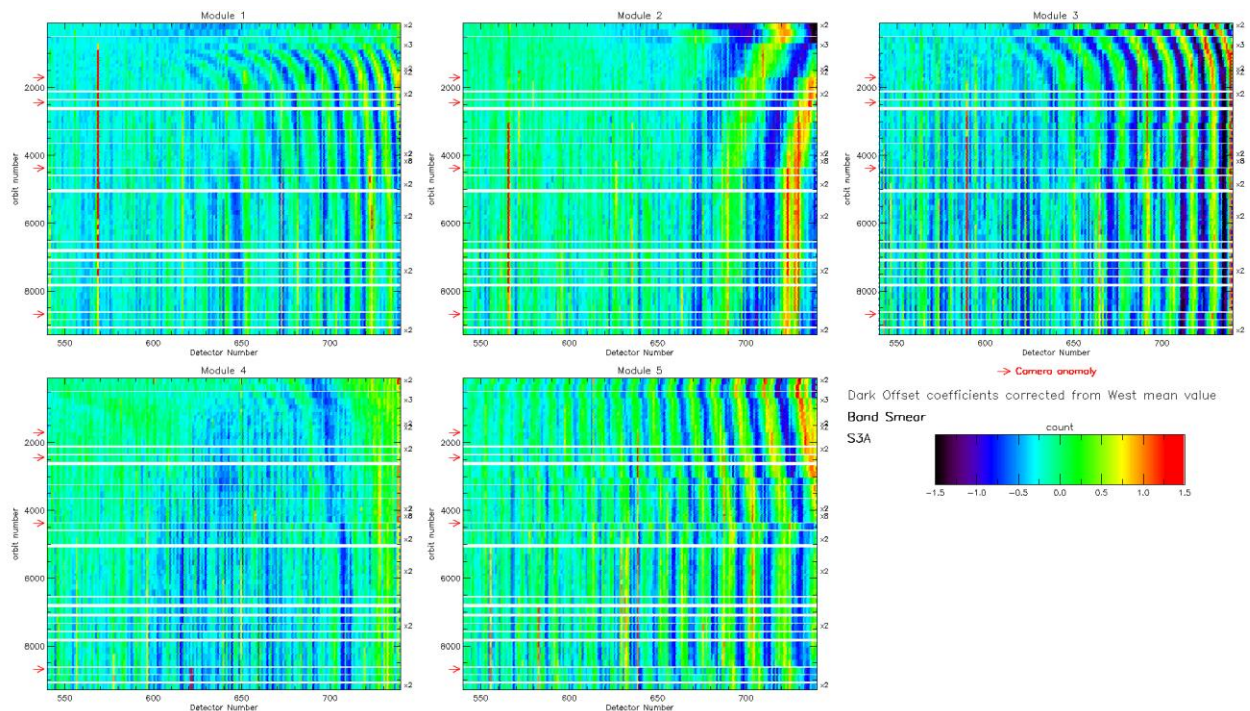


Figure 8: same as Figure 7 for smear band.



Figure 7 and Figure 8 show the so-called ‘map of periodic noise’ in the 5 cameras, for respectively band 21 and smear band. These maps have been computed from the dark offsets after removal of the mean level of the WEST detectors (not impacted by PN) in order to remove mean level gaps and consequently to highlight the shape of the PN. Maps are focused on the last 200 EAST detectors where PN occurs. We see that the reset of the OLCI instrument performed on 16 OCT 2017 – in this case a soft reset only – , orbit 8666 (cycle #23) ,following a camera anomaly, had a significant impact on the shape of the PN. The most impacted band is the smear band for camera 5 (see also Figure 9), as well as, to a lesser extent, camera 2 and 3. In band Oa21, the reset of the instrument did not seem to have a significant impact on the shape of the PN even though we can notice that the phase of the PN of camera 2 keeps on drifting since several calibrations.

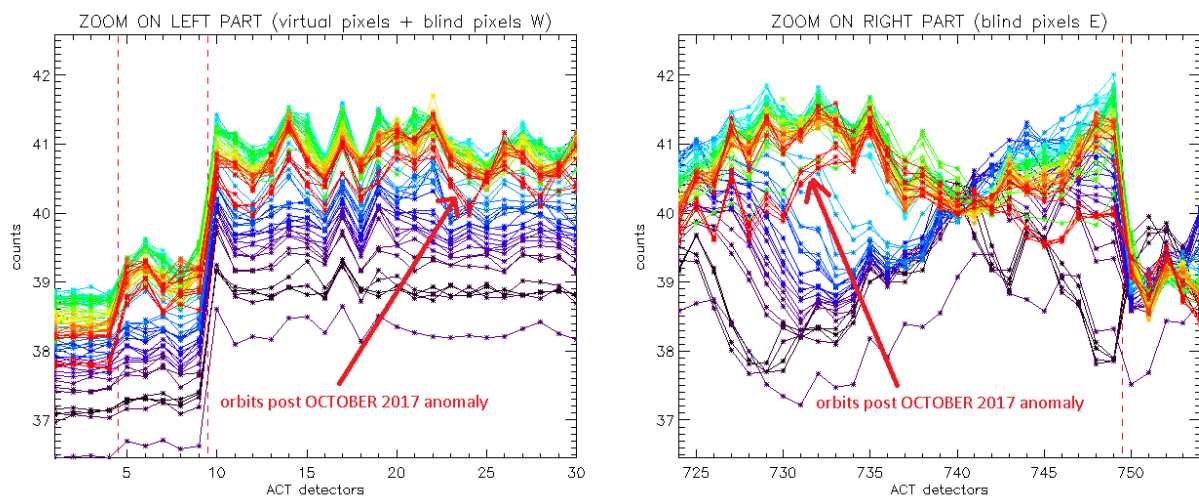


Figure 9: Dark Offset levels for smear band camera 5, for (left plot) first 30 WEST detectors including virtual and blind pixels, (right plot) last 30 EAST detectors including blind pixels. The colour of the curves is linked to the orbit number, from the beginning of the mission in black, to the last CALs in red. We see on the right plot that the shape of the PN for the CALs at orbit ≥ 8736 has been strongly modified by the reset of the OLCI instrument of orbit 8666 (Cycle #23). As a consequence, the global mean level of the dark offset is impacted by this change of PN, through the OCL convergence, as illustrated in the left plot.

Based on the results presented in Figure 8 and Figure 9, we recommend that the CAL_AX used in PDGS is updated, as soon as possible, with a dark offset table and a dark current table computed from a Calibration sequence posterior to the October 2017-anomaly. This will be implemented at the next PB update (foreseen in December).

Dark Currents

Dark Currents are not affected by the global offset of the Dark Offsets, thanks to the clamping to the average blind pixels value. However, the oscillations of Periodic Noise remain visible. There is no significant evolution of this parameter during the current cycle.

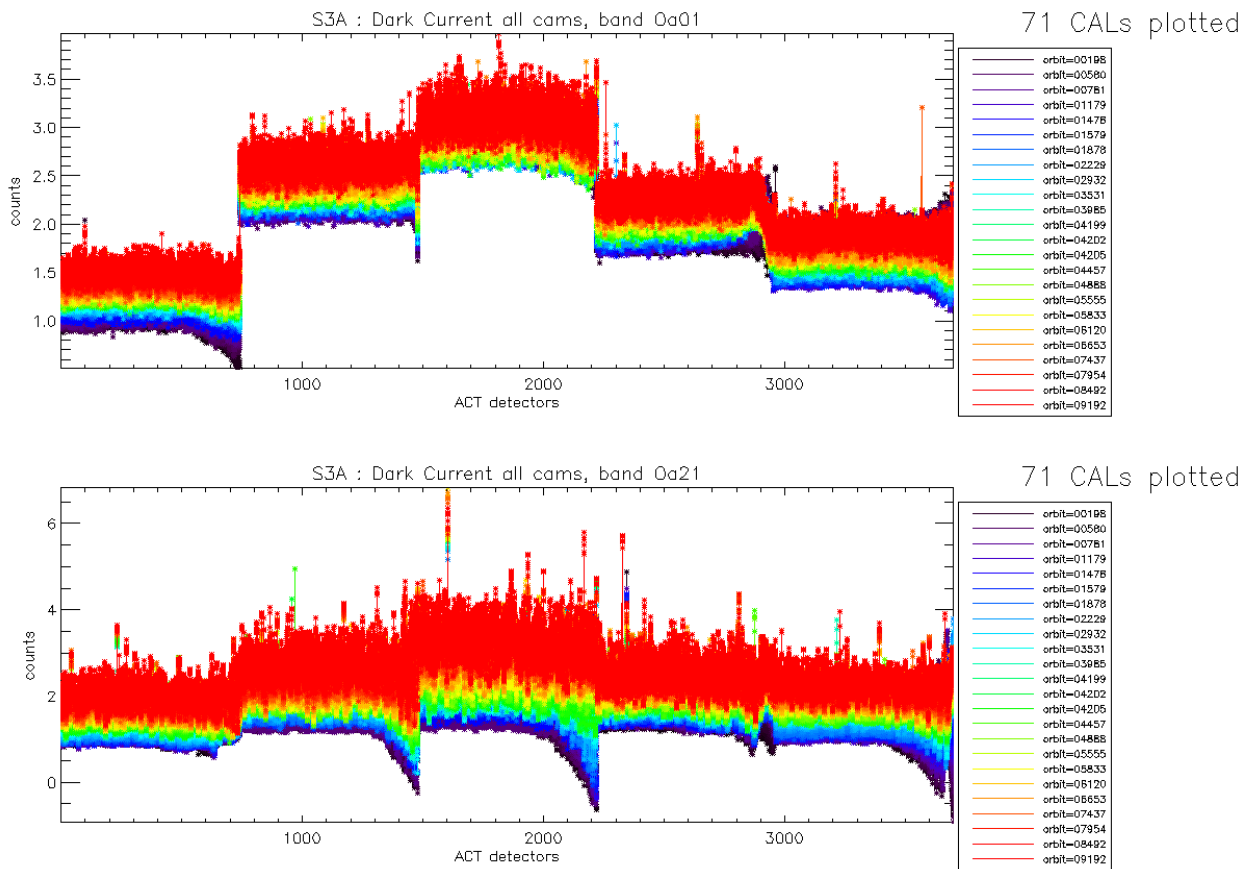


Figure 10: Dark Current for band Oa1 (top) and Oa21 (bottom), all radiometric calibrations so far except the first one (orbit 183) for which the instrument was not thermally stable yet.

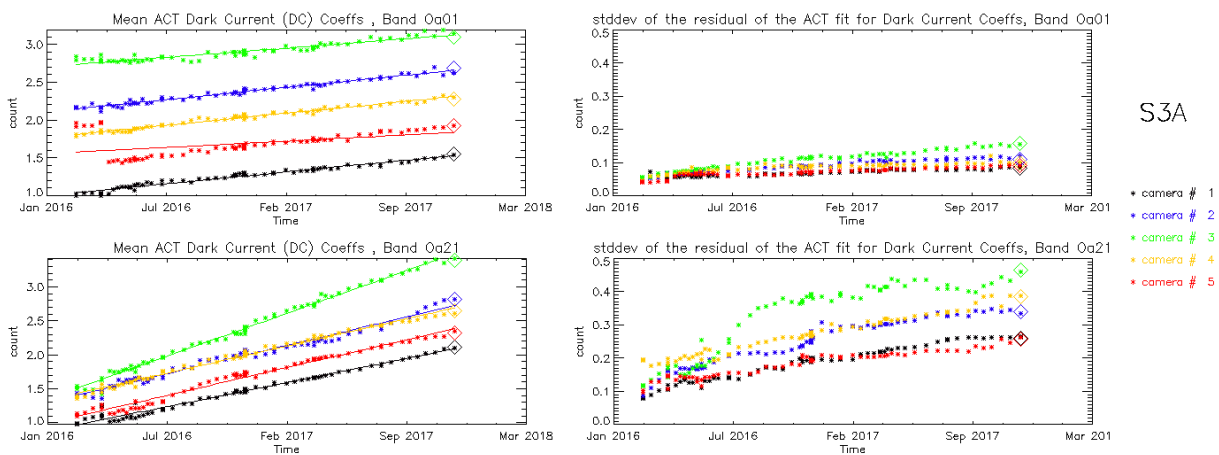


Figure 11: left column: ACT mean on 400 first detectors of Dark Current coefficients for spectral band Oa01 (top) and Oa21 (bottom). Right column: same as left column but for Standard deviation instead of mean. We see an increase of the DC level as a function of time especially for band Oa21. A possible explanation could be the increase of the number of hot pixels which is more important in Oa21 because this band is made of more CCD lines than band Oa01 and thus receives more cosmic rays impacts. It is known that cosmic rays degrade the structure of the CCD, generating more and more hot pixels at long term scales.

1.2.2 Instrument response and degradation modelling [OLCI-L1B-CV-250]

1.2.2.1 Instrument response monitoring

Figure 12 below shows the gain coefficients of every pixel for two OLCI channels, Oa1 (400 nm) and Oa21 (1020 nm), highlighting the significant evolution of the instrument response since early mission.

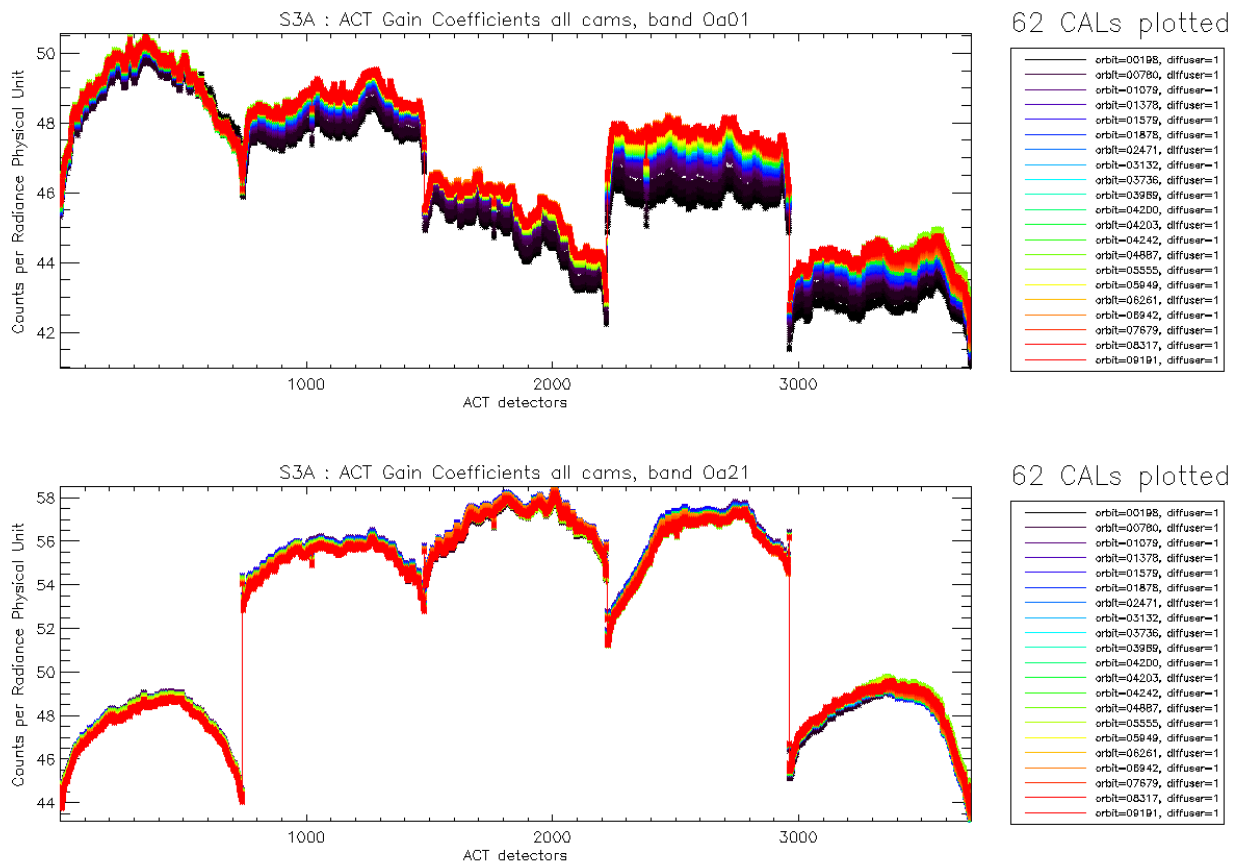


Figure 12: Gain Coefficients for band Oa1 (top) and Oa21 (bottom), all diffuser 1 radiometric calibrations so far except the first one (orbit 183) for which the instrument was not thermally stable yet.

The gains plotted in Figure 12, however are derived using the ground BRDF model – as the only one available in the operational processing software so far – which is known to suffer from illumination geometry dependent residual errors (see previous Cyclic Reports for more details). Consequently they are post-processed to replace the ground BRDF model by the in-flight version, based on Yaw Manoeuvres data, prior to determine the radiometric evolution.

Figure 13 displays a summary of the time evolution derived from post-processed gains: the cross-track average of the BRDF corrected gains is plotted as a function of time, for each module, relative to a given reference calibration (the 12/12/2016). It shows that, if a significant evolution occurred during the early mission, the trends tend to stabilize, with the exception of band 1 of camera 4.

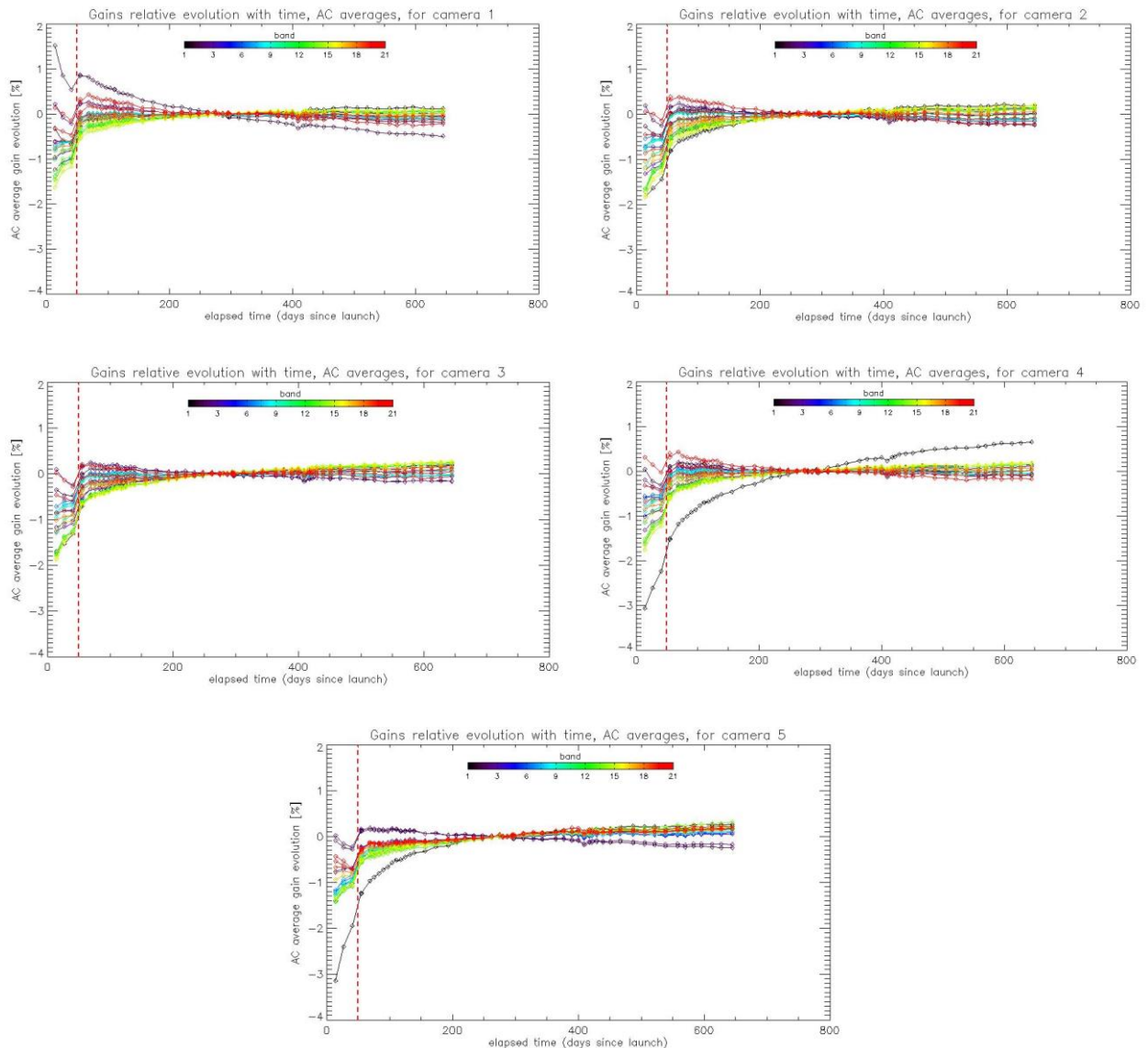


Figure 13: camera averaged gain relative evolution with respect to “best geometry” calibration (22/11/2016), as a function of elapsed time since launch; one curve for each band (see colour code on plots), one plot for each module. The star tracker anomaly fix (6/04/16) is represented by a vertical red dashed line.

The behaviour over the first two months of mission, really different and highlighted by Figure 13, is explained by the Star Tracker software anomaly during which the attitude information provided by the platform was corrupted, preventing to compute a correct illumination geometry, with a significant impact on the gain computation.

1.2.2.2 Instrument evolution modelling

As mentioned in previous cycle #22 Report, the OLCI Radiometric Model has been refreshed, and put in operations the 11/10/2017. The model has been derived on the basis of an extended Radiometric Calibration dataset (from 26/04/2016 to 27/08/2017), and includes the correction of the diffuser ageing



for the five bluest bands (Oa1 to Oa5) for which it is clearly measurable. The model performance over the complete dataset (including the 6 calibrations in extrapolation over three months) remains better than 0.1% when averaged over the whole field of view (Figure 14), while the previous model, trained on a Radiometric Dataset limited to 12/03/2017, shows a slow drift of the model with respect to most recent data (Figure 15). Comparison of the two figures shows the improvement brought by the updated Model.

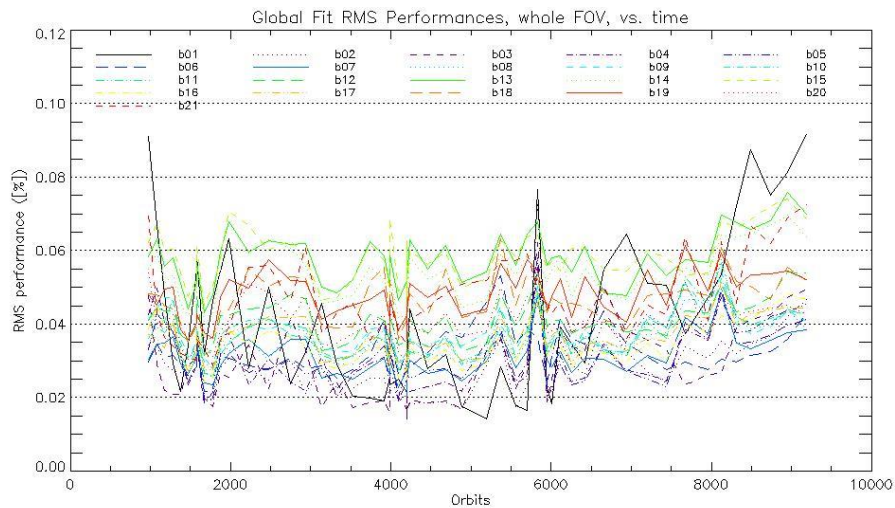


Figure 14: RMS performance of the Gain Model of current Processing Baseline as a function of orbit.

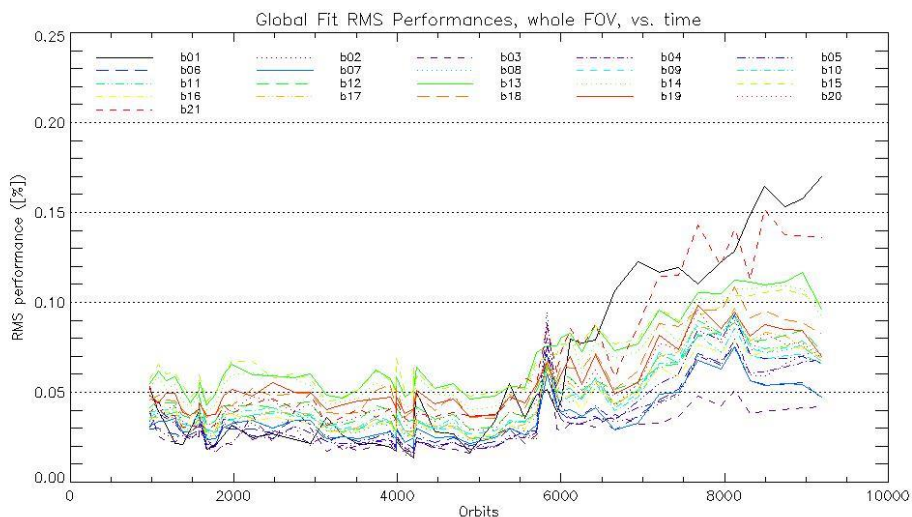


Figure 15: RMS performance of the Gain Model of previous Processing Baseline as a function of orbit.

The overall instrument evolution since channel programming change (25/04/2016) is shown on Figure 16.

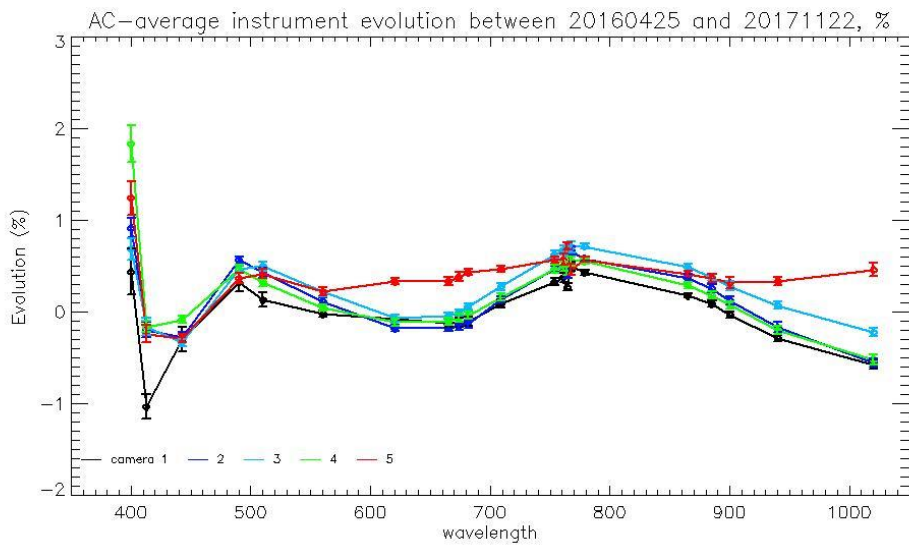


Figure 16: Camera-averaged instrument evolution since channel programming change (25/04/2016) and up to most recent calibration (22/11/2017) versus wavelength.

The overall per camera performance, as a function of wavelength, and at each orbit is shown on Figure 17 as the average and standard deviation of the model over data ratio.

Finally, Figure 18 to Figure 20 show the detail of the model performance, with across-track plots of the model over data ratios at each orbit, one plot for each channel.

Comparisons of Figure 17 to Figure 20 with their counterparts in Report of Cycle 22 clearly demonstrate the improvement brought by the new model whatever the level of detail.

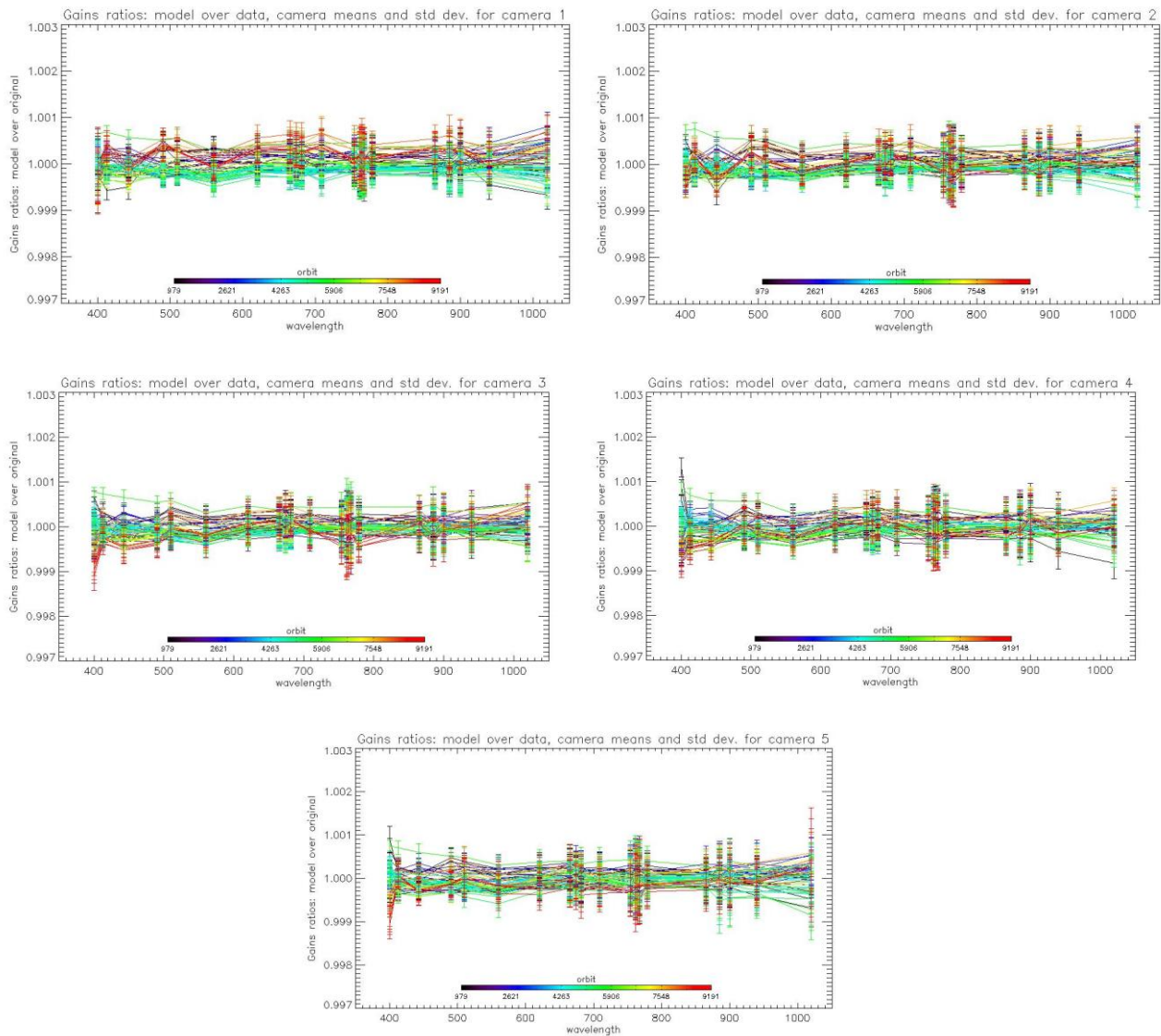


Figure 17: For the 5 cameras: Evolution model performance, as camera-average and standard deviation of ratio of Model over Data vs. wavelength, for each orbit of the test dataset, including 6 calibration in extrapolation, with a colour code for each calibration from blue (oldest) to red (most recent).

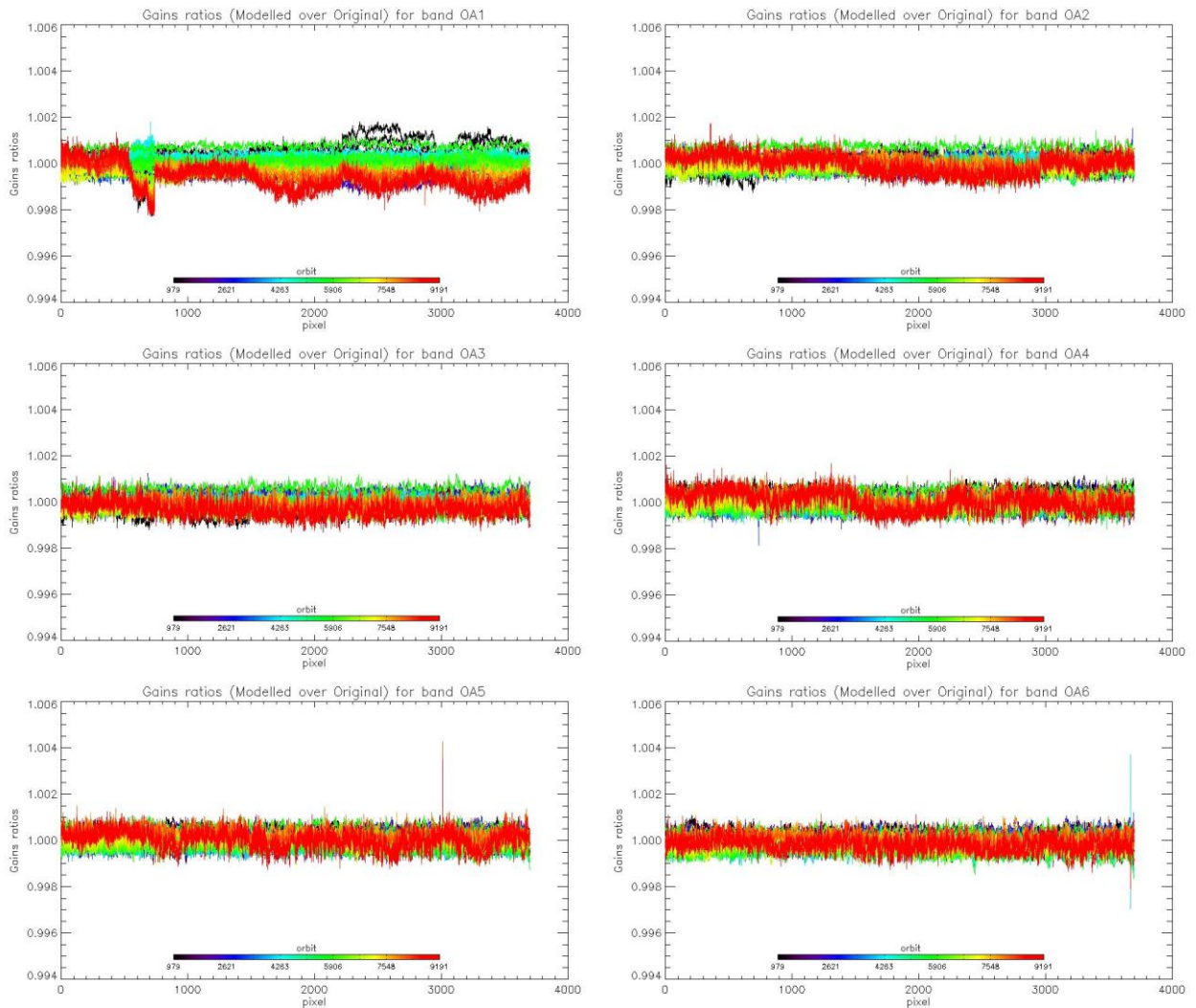


Figure 18: Evolution model performance, as ratio of Model over Data vs. pixels, all cameras side by side, over the whole current calibration dataset (since instrument programming update), including 6 calibrations in extrapolation, channels Oa1 to Oa6.



Sentinel-3 MPC
S3-A OLCI Cyclic Performance Report
Cycle No. 024

Ref.: S3MPC.ACR.PR.01-024
Issue: 1.0
Date: 30/11/2017
Page: 15

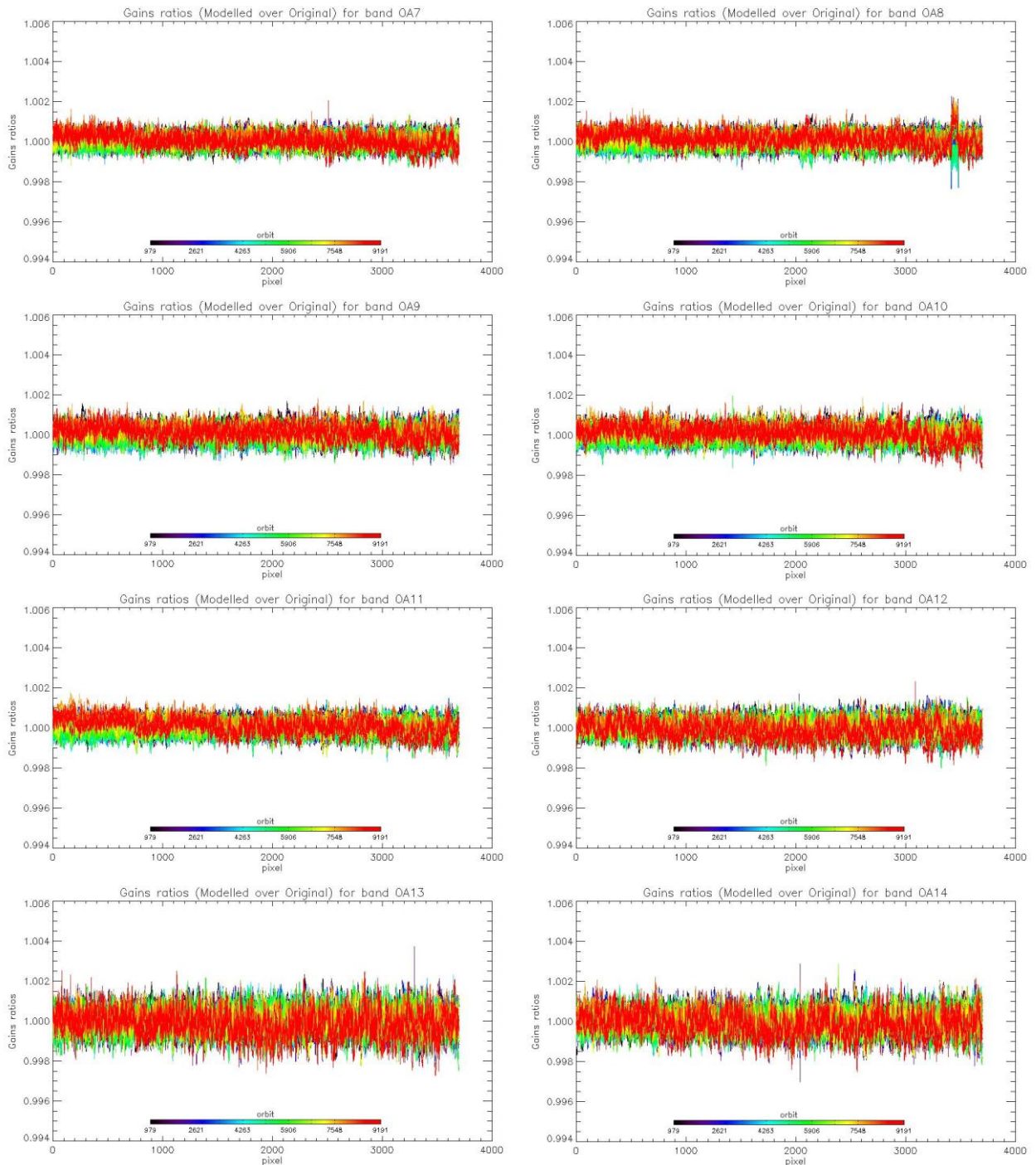


Figure 19: same as Figure 14 for channels Oa7 to Oa14.

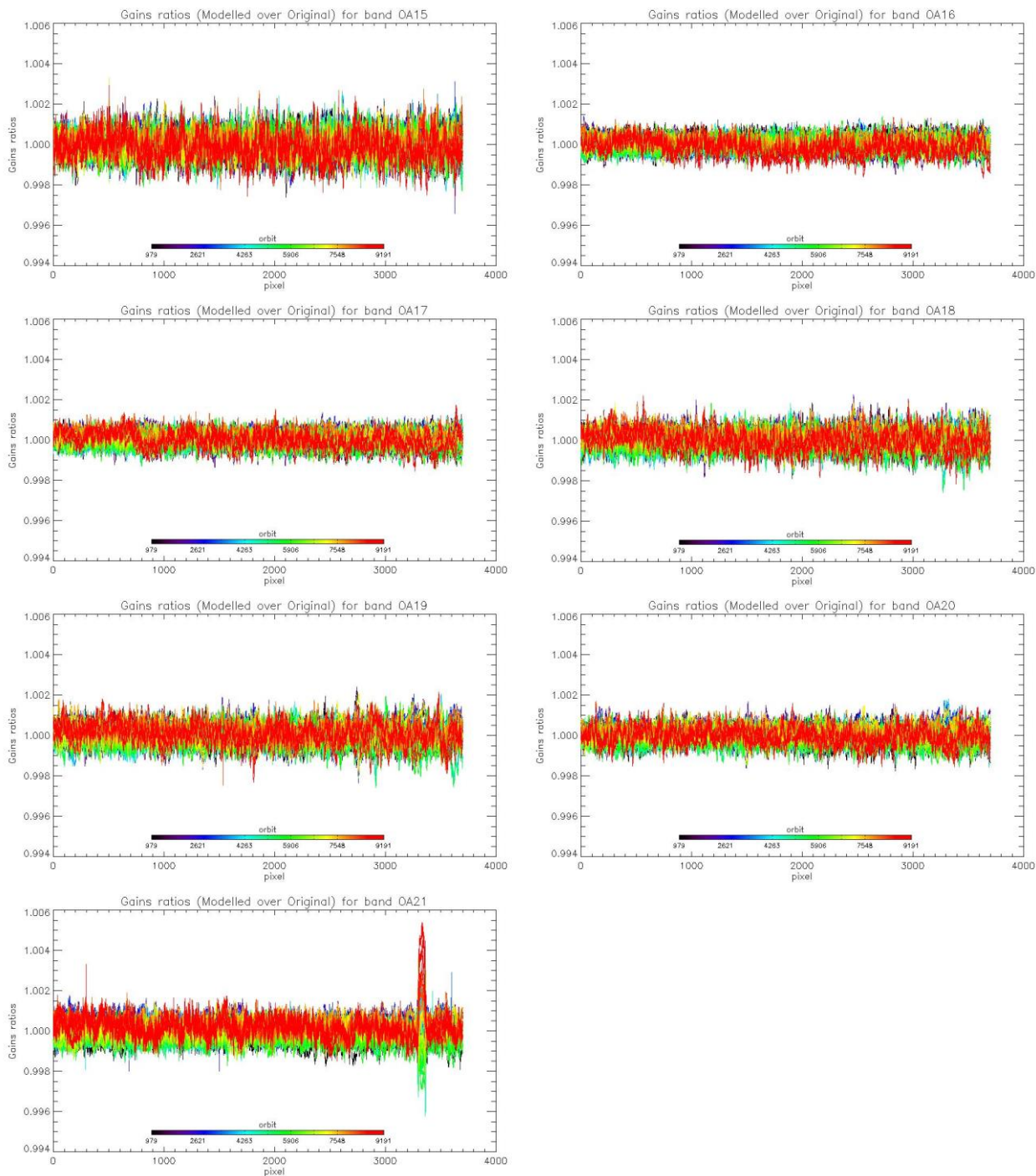


Figure 20: same as Figure 18 for channels Oa15 to Oa21.

1.2.3 Ageing of nominal diffuser [OLCI-L1B-CV-240]

There has been one calibration sequence S05 (reference diffuser) acquisition during cycle 024:

- ❖ S05 sequence (diffuser 2) on 22/11/2017 10:14 to 10:16 (absolute orbit 9192)

The diffuser 1 Ageing is computed for each 3700 detector and each spectral band by formula:

$$\text{Ageing}(\text{orb}) = G1(\text{orb})/G2(\text{orb}) - G1(\text{orb_ref})/G2(\text{orb_ref})$$

Where:

- ❖ G1 is the diffuser 1 (= nominal diffuser) Gain coefficients
- ❖ G2 is the diffuser 2 (= reference diffuser) Gain coefficients
- ❖ orb_ref is a reference orbit chosen at the beginning of the mission

Ageing is represented in Figure 21 for band Oa1 and in Figure 22 for band Oa16. The negative shift of the sequence at orbit 5832 (for which a slight increase would be expected instead) is not explained so far and still under investigation. It should be noted that the corresponding orbit of diffuser 1 (nominal) has also been detected as an outlier in the modelling of the radiometric long-term trend with an unexpected excess of brightness.

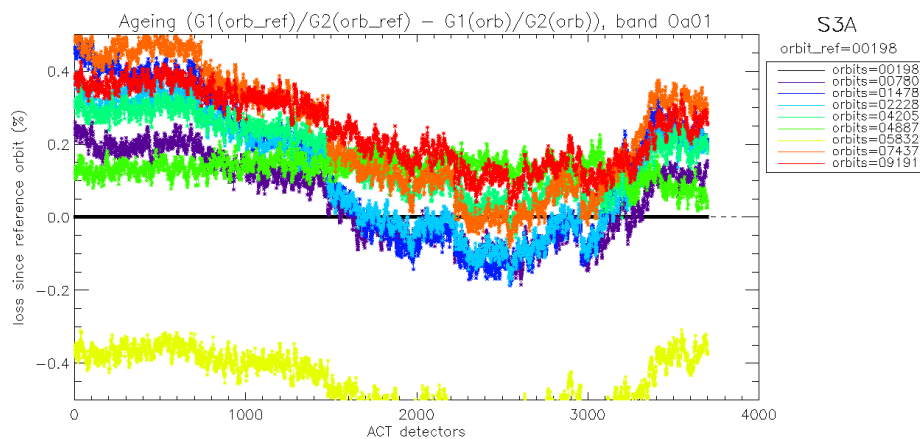


Figure 21: diffuser 1 ageing for spectral band Oa01. We see strong ACT low frequency structures that are due to residual of BRDF modelling.



Sentinel-3 MPC
S3-A OLCI Cyclic Performance Report
Cycle No. 024

Ref.: S3MPC.ACR.PR.01-024
 Issue: 1.0
 Date: 30/11/2017
 Page: 18

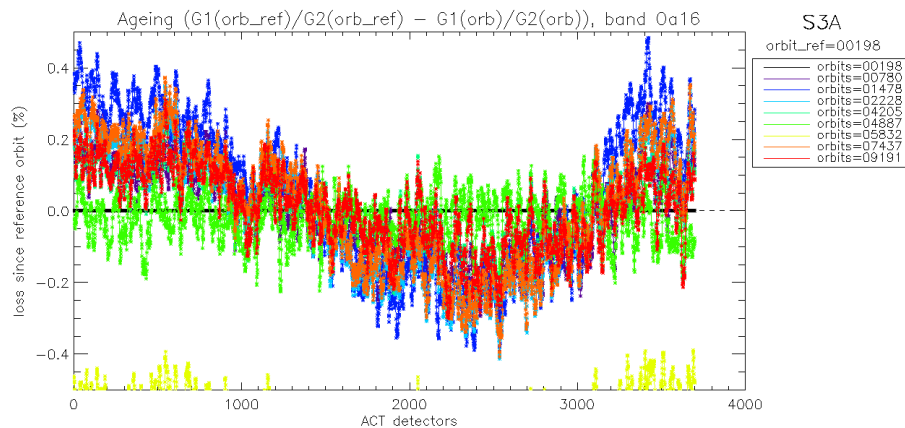


Figure 22: same as Figure 21 for spectral band Oa16. We use this band in order to normalize other bands and remove the ACT structures due to residual of BRDF modelling. Normalized curve for spectral band Oa01 is presented in Figure 23.

Figure 21 and Figure 22 show that the Ageing curves are impacted by a strong ACT pattern which is due to residuals of the bad modelling (on-ground) of the diffuser BRDF. This pattern is dependant of the azimuth angle. It is a 'white' pattern which means it is the same for all spectral bands. As such, we can remove this pattern by normalizing the ageing of all bands by the curve of band Oa16 which is expected not to be impacted by ageing because in the red part of the spectrum. We use an ACT smoothed version (window of 100 detectors) of band Oa16 in order to reduce the high frequency noise. Normalized ageing for spectral band Oa01 is represented in Figure 23 where we can see that this band is impacted by ageing of the diffuser.

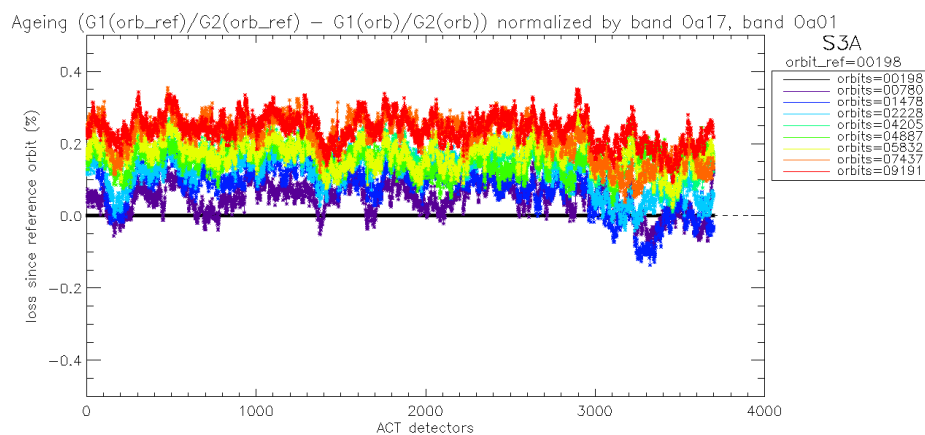


Figure 23: same as Figure 21 after normalization by band Oa16. Ageing of the diffuser 1 is now visible in the 5 cameras.

Camera averaged ageing (normalized by band Oa16) as a function of wavelength is represented in Figure 24 where we can see that ageing is stronger in the 'bluest' spectral bands (short wavelengths). Ageing is visible only for the 5 first spectral bands so far in the OLCI mission life.

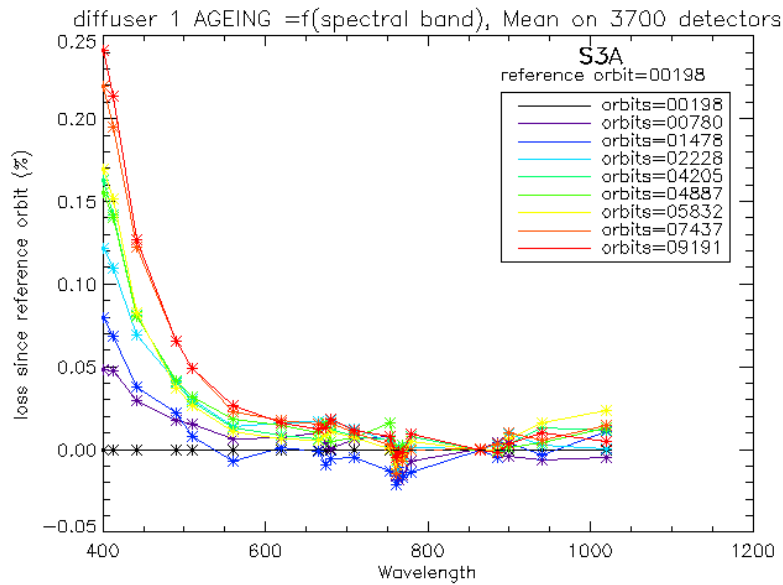


Figure 24: Diffuser 1 ageing as a function of wavelength (or spectral band). Ageing is visible in spectral band #1 to #5.

Figure 25 shows the evolution of the 5 camera averaged ageing as a function of time.

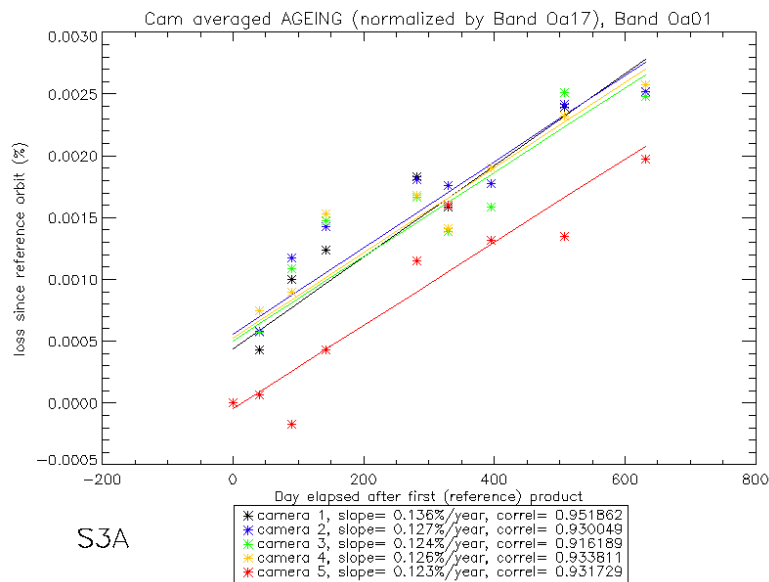


Figure 25: Camera averaged ageing (normalized by band Oa16) as a function of time. Linear fit for each camera is plotted. The slope (% loss per year) and the correlation coefficient

A model of diffuser ageing as a function of cumulated exposure time (i.e. number of acquisition sequence on nominal diffuser, regardless of the band setting) has been built and is described in Cyclic #23 Report. The results of this model confirm the need to model ageing against cumulated exposure

rather than elapsed time, as it provides a more linear trend, even if not perfect (see Figure 21 of Cyclic #23 Report) .

The slope of this ageing model (% of loss per exposure) as a function of wavelength is presented in Figure 26).

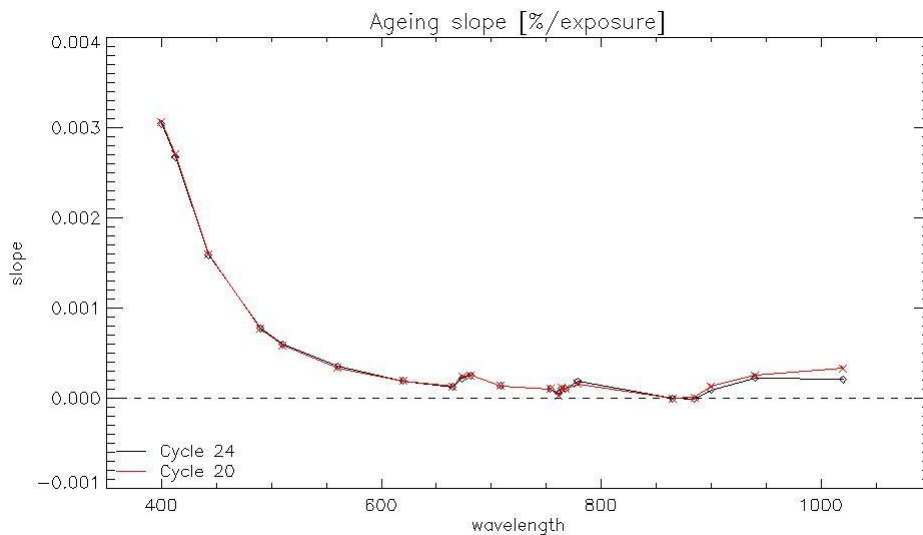


Figure 26: Slope of ageing fit (% of loss per exposure) vs wavelengths, using all the available ageing sequence at the time of the current cycle (black curve) and at the time of cycle #20 (red curve)


In Figure 26, we see that the Ageing slopes have not changed between the current Cycle and the last cycle with a S05 sequence (cycle #20), except for the last wavelength (band Oa21) for which the ageing slope is closer to 0 for the current cycle, as expected (No ageing expected in the NIR).

The exposure time dependent ageing model has been used to derive a new Gain Model, put in operations on 11th October 2017. A dedicated Verification Report has been issued (S3MPC.ACR.VR.025).

1.2.4 Updating of calibration ADF [OLCI-L1B-CV-260]

Six calibration ADFs have been generated to complement the Processing Baseline of the on-going global reprocessing. It includes Dark Correction tables with HEP filtering (see above) and the updated Gain Model, accounting for all available RC up to cycle 21 and the ageing of the nominal diffuser (see section 1.2.2). Another one could have been generated using the very last RC (22/11) but it is not required for the RP and its end validity date is not yet confirmed by the success of the next RC acquisition.

S3A_OL_1_CAL_AX_20170827T142237_20170908T173447_20171120T151915_____	MPC_O_AL_R03.SEN3
S3A_OL_1_CAL_AX_20170908T173447_20170922T012401_20171120T151915_____	MPC_O_AL_R03.SEN3
S3A_OL_1_CAL_AX_20170922T012401_20171004T075821_20171120T151915_____	MPC_O_AL_R03.SEN3
S3A_OL_1_CAL_AX_20171004T075821_20171021T104116_20171120T151915_____	MPC_O_AL_R03.SEN3
S3A_OL_1_CAL_AX_20171021T104116_20171105T041006_20171120T151915_____	MPC_O_AL_R03.SEN3
S3A_OL_1_CAL_AX_20171105T041006_20171122T083319_20171120T151915_____	MPC_O_AL_R03.SEN3

	<p>Sentinel-3 MPC</p> <p>S3-A OLCI Cyclic Performance Report</p> <p>Cycle No. 024</p>	<p>Ref.: S3MPC.ACR.PR.01-024</p> <p>Issue: 1.0</p> <p>Date: 30/11/2017</p> <p>Page: 21</p>
--	--	--

1.2.5 Radiometric Calibrations for sun azimuth angle dependency and Yaw Manoeuvres for Solar Diffuser on-orbit re-characterization [OLCI-L1B-CV-270 and OLCI-L1B-CV-280]

This activity has not evolved during cycle 024 and results presented in previous report are still valid.

1.3 Spectral Calibration [OLCI-L1B-CV-400]

There have been two Spectral Calibration acquisitions during cycle 024.

One S02/S03:

- ❖ S02 sequence (diffuser 1) on 04/11/2017 11:20 to 11:22 (absolute orbit 8936)
- ❖ S03 sequence (Erbium doped diffuser) on 04/11/2017 13:01 to 13:03 (absolute orbit 8937)

And one S09 (Fraunhofer lines)

- ❖ S09 sequence on 04/11/2017 08:59 to 09:04 (absolute orbit 8935)

The long term evolution of spectral calibration obtained with calibration sequence S02/S03 is presented in Figure 27 and Figure 28 and the one obtained with calibration sequence S09 is presented in Figure 29.



Sentinel-3 MPC
S3-A OLCI Cyclic Performance Report
Cycle No. 024

Ref.: S3MPC.ACR.PR.01-024
Issue: 1.0
Date: 30/11/2017
Page: 22

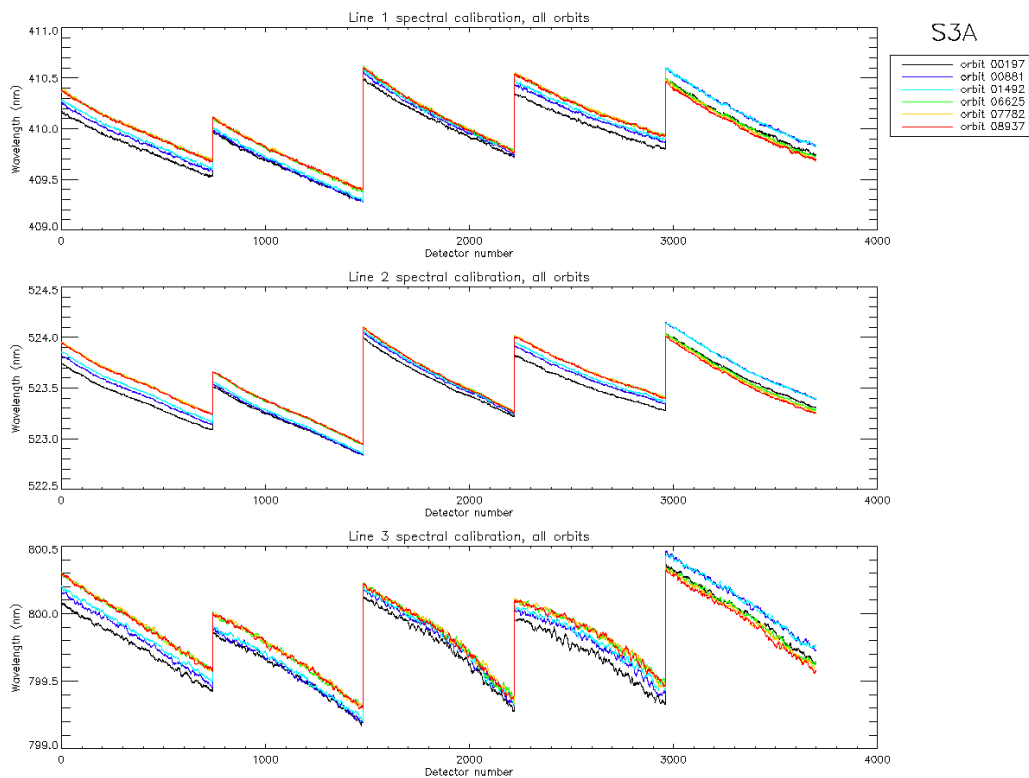


Figure 27: across track spectral calibration for all S02/S03 sequences since the beginning of the mission. Top plot is spectral line 1, middle plot is spectral line 2 and bottom plot spectral line 3.



Sentinel-3 MPC

S3-A OLCI Cyclic Performance Report

Cycle No. 024

Ref.: S3MPC.ACR.PR.01-024
 Issue: 1.0
 Date: 30/11/2017
 Page: 23

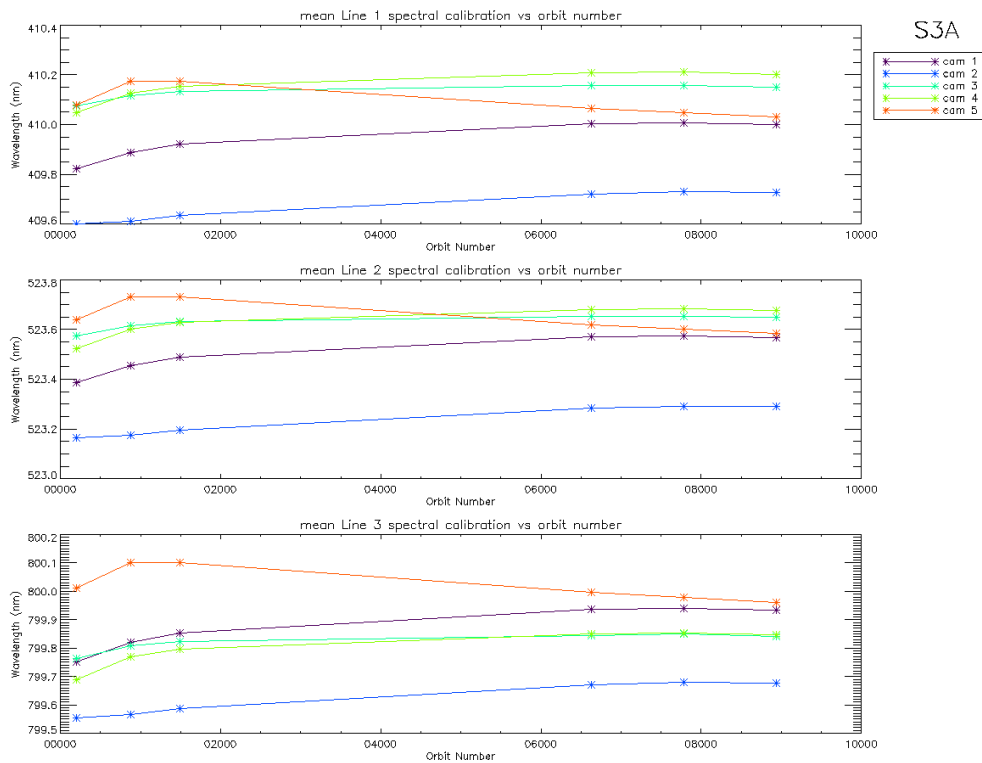


Figure 28: camera averaged spectral calibration as a function of orbit number (all spectral S02/S03 calibrations since the beginning of the mission are included). Top plot is spectral line 1, middle plot is spectral line 2 and bottom plot spectral line 3.

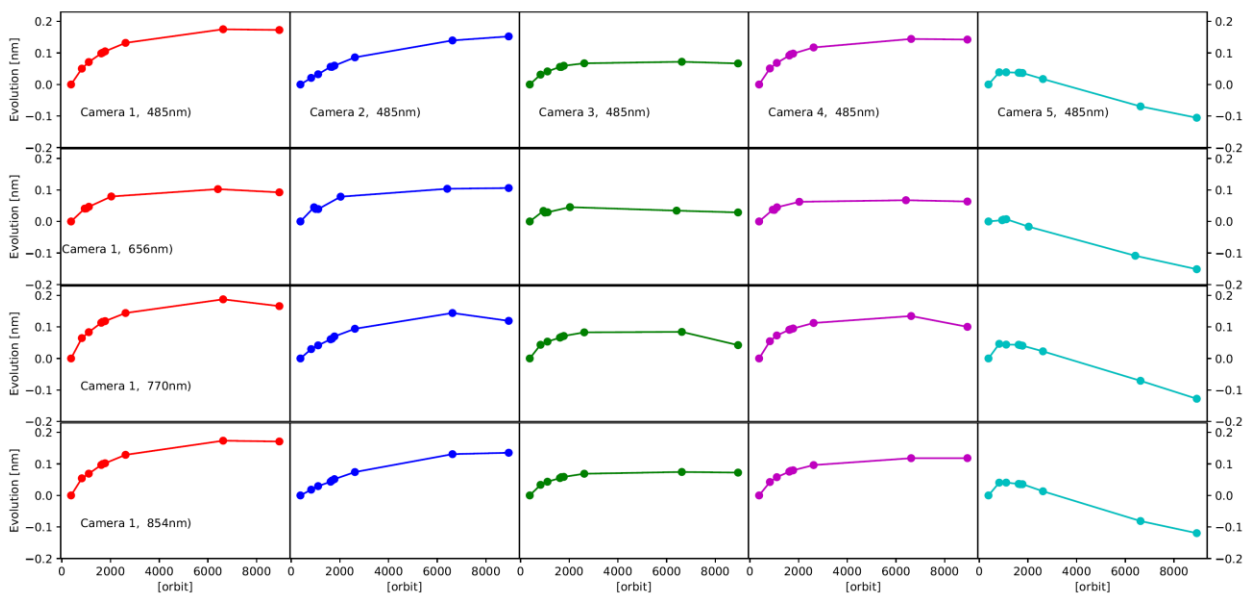



Figure 29: spectral calibration as a function of time derived from all S09 sequences. From left to right column: the 5 cameras. From top to bottom: Used absorption line: 485 nm, 656 nm, 770 nm and 854 nm.

	<p>Sentinel-3 MPC</p> <p>S3-A OLCI Cyclic Performance Report</p> <p>Cycle No. 024</p>	<p>Ref.: S3MPC.ACR.PR.01-024</p> <p>Issue: 1.0</p> <p>Date: 30/11/2017</p> <p>Page: 24</p>
--	--	--

We see that the long term evolution of the spectral calibration obtained with sequence S09 (Figure 29) is in rather good agreement with the one obtained with sequence S02/S03 (Figure 28). Indeed, we observe for both methods a general positive trend of the spectral calibration for camera 1, 2, 3 and 4 with a kind of stabilization at the end for camera 3 and perhaps camera 4. An obvious negative trend is present in camera 5 also in both methods. It should be noted that the outlying behaviour of the last S09 sequence for the O2A line at 770nm (more pronounced decrease than for other wavelengths) is attributed to the imaged Earth surface, a mix of water and desert, while previous one were only acquired over desert. A mechanism to exclude water pixels is put in place from now on.

In all cases, the spectral calibration drift is smaller than 0.2 nm and the change with respect to the values included in the Auxiliary Data files is less than 0.1 nm. However camera 5, and to a lesser extend cameras 1 2 and 4, do further evolve thus and an evolution of the Auxiliary Parameters impacted by the instrument spectral model, reflecting the current state of the instrument, has to be considered.

1.4 Signal to Noise assessment [OLCI-L1B-CV-620]

1.4.1 SNR from Radiometric calibration data.

SNR computed for all calibration data as a function of band number is presented in Figure 30.

SNR computed for all calibration data as a function of orbit number for band Oa01 (the less stable band) is presented in Figure 31.

There is no significant evolution of this parameter during the current cycle and the ESA requirement is fulfilled for all bands.

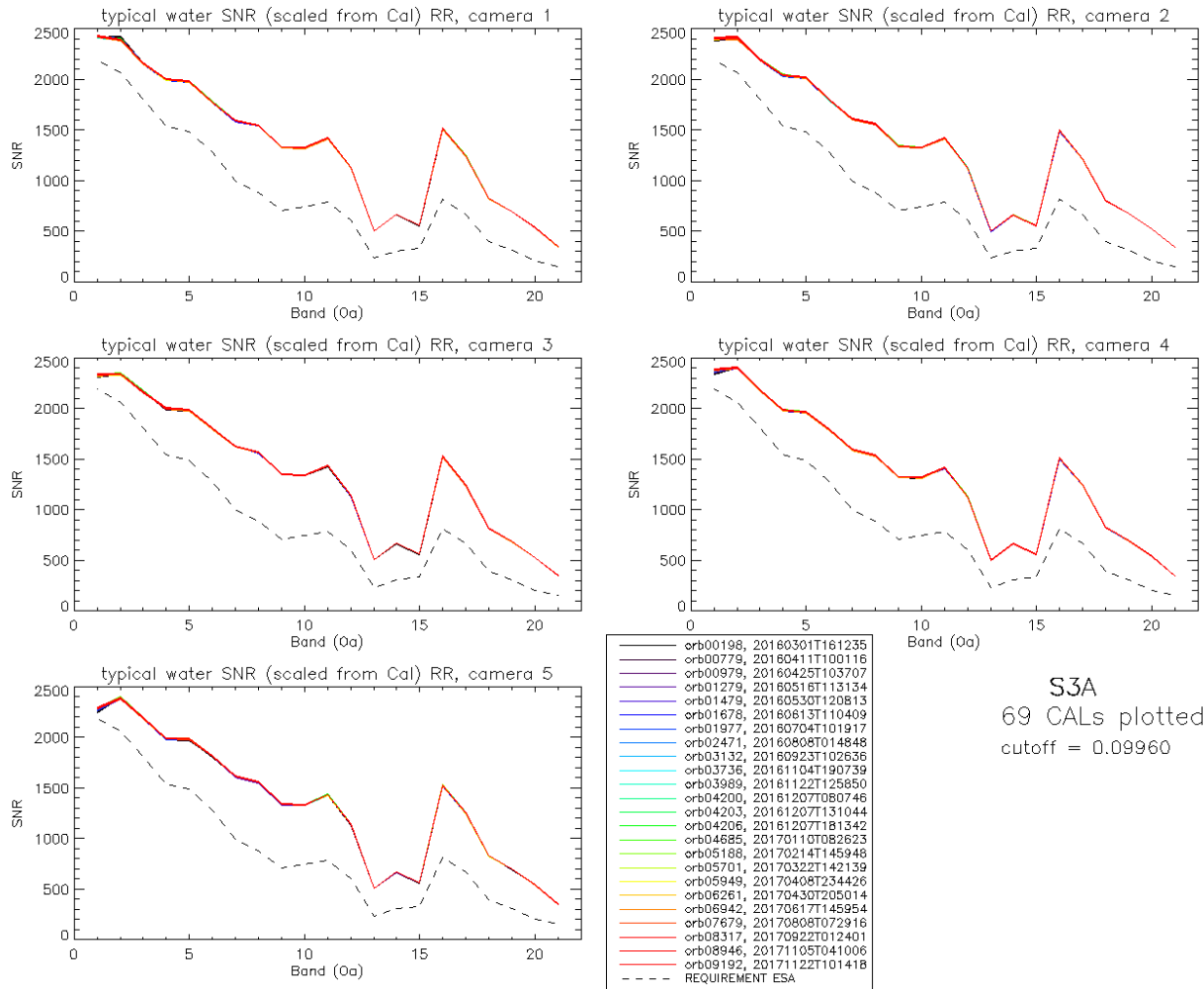


Figure 30: Signal to Noise ratio as a function of the spectral band for the 5 cameras. These results have been computed from radiometric calibration data. All calibrations except first one (orbit 183) are presents with the colours corresponding to the orbit number (see legend). The SNR is very stable with time: the curves for all orbits are almost superimposed. The dashed curve is the ESA requirement.

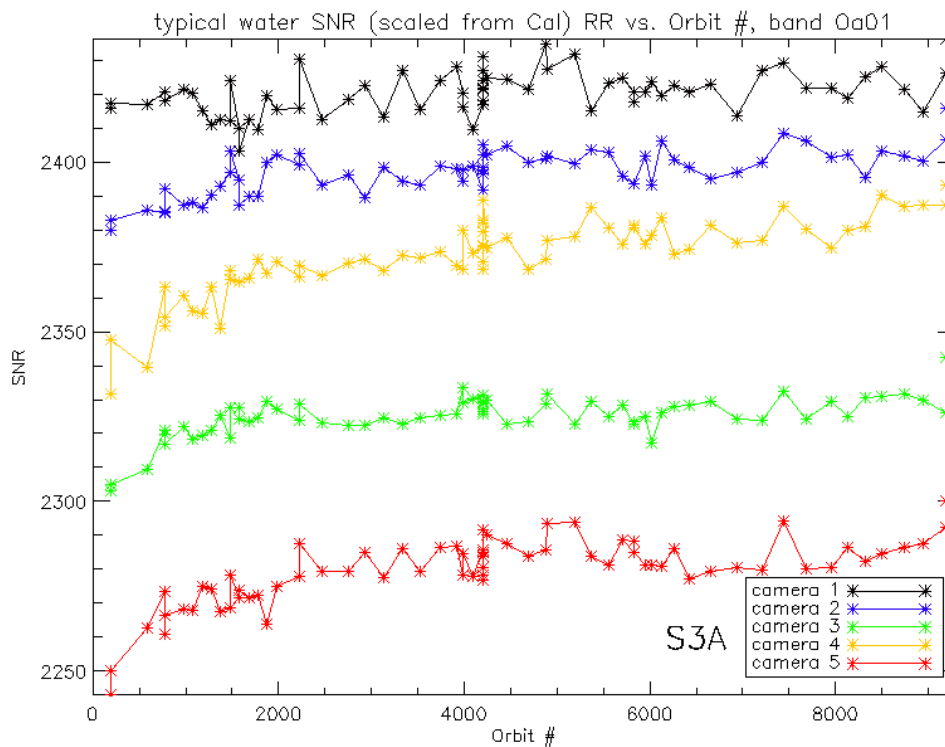


Figure 31: long-term stability of the SNR estimates from Calibration data, example of channel Oa01.

The mission averaged SNR figures are provided in Table 1 below, together with their radiance reference level. According to the OLCI SNR requirements, these figures are valid at these radiance levels and at Reduced Resolution (RR, 1.2 km). They can be scaled to other radiance levels assuming shot noise (CCD sensor noise) is the dominating term, i.e. radiometric noise can be considered Gaussian with its standard deviation varying as the square root of the signal; in other words: $SNR(L) = SNR(L_{ref}) \cdot \sqrt{\frac{L}{L_{ref}}}$. Following the same assumption, values at Full Resolution (300m) can be derived from RR ones as 4 times smaller.



Sentinel-3 MPC
S3-A OLCI Cyclic Performance Report
Cycle No. 024

Ref.: S3MPC.ACR.PR.01-024
 Issue: 1.0
 Date: 30/11/2017
 Page: 27

Table 1: SNR figures as derived from Radiometric Calibration data. Figures are given for each camera (time average and standard deviation), and for the whole instrument. The requirement and its reference radiance level are recalled (in $mW.sr^{-1}.m^{-2}.nm^{-1}$).

λ nm	L _{ref} LU	SNR RQT	C1		C2		C3		C4		C5		All	
			avg	std	avg	std	avg	std	avg	std	avg	std	avg	std
400.000	63.0	2188	2420	6.3	2396	6.6	2325	6.0	2372	11.5	2279	9.8	2358	6.9
412.000	74.1	2061	2395	7.6	2409	5.5	2340	4.8	2402	4.4	2385	6.8	2386	3.9
442.000	65.6	1811	2161	5.3	2199	5.7	2166	4.7	2186	4.1	2197	4.8	2182	3.3
490.000	51.2	1541	2000	5.0	2035	5.5	1996	3.7	1981	4.0	1987	5.0	2000	3.5
510.000	44.4	1488	1979	5.4	2013	5.0	1983	4.7	1965	4.6	1984	4.8	1985	3.9
560.000	31.5	1280	1775	4.3	1801	4.3	1801	4.8	1794	4.1	1818	3.7	1798	3.2
620.000	21.1	997	1591	4.2	1610	4.3	1625	3.1	1593	3.4	1614	3.5	1607	2.7
665.000	16.4	883	1546	4.7	1558	4.2	1566	3.9	1533	4.0	1560	3.8	1553	3.2
674.000	15.7	707	1329	3.3	1338	3.8	1350	2.9	1324	3.0	1341	3.8	1336	2.6
681.000	15.1	745	1320	3.7	1326	3.1	1337	2.9	1314	2.6	1332	3.7	1326	2.3
709.000	12.7	785	1420	4.7	1420	4.3	1434	3.6	1413	3.7	1429	3.1	1423	3.1
754.000	10.3	605	1127	3.5	1120	3.1	1134	3.6	1124	2.5	1138	2.9	1128	2.6
761.000	6.1	232	502	1.3	498	1.3	505	1.3	500	1.1	507	1.5	502	1.0
764.000	7.1	305	662	1.7	657	1.6	667	2.2	661	1.7	669	2.0	663	1.5
768.000	7.6	330	558	1.7	554	1.3	562	1.3	556	1.6	564	1.3	559	1.2
779.000	9.2	812	1514	5.2	1496	5.1	1523	5.5	1509	5.4	1524	4.9	1513	4.6
865.000	6.2	666	1243	3.8	1212	4.3	1237	4.3	1245	4.0	1249	2.9	1238	3.3
885.000	6.0	395	823	1.9	801	1.7	814	2.1	824	1.5	831	1.8	818	1.3
900.000	4.7	308	691	1.5	673	1.3	683	1.8	693	1.5	698	1.5	687	1.1
940.000	2.4	203	534	1.1	522	1.1	525	1.1	539	1.2	542	1.3	532	0.8
1020.000	3.9	152	345	0.7	337	0.7	348	0.8	345	0.8	351	0.7	345	0.5

1.4.2 SNR from EO data.

There has been no update on SNR assessment from EO data during the cycle. Last figures (cycle 9) are considered valid.

1.5 Geometric Calibration/Validation

Regular monitoring using the GeoCal Tool implemented within the MPMF continues. Late August results confirm good performance. Monitoring of the geolocation performance by correlation with GCP imagettes using the GeoCal tool over the period confirms that OLCI is compliant with its requirement: the centroid of the geolocation error is around 0.25 to 0.35 pixel in both along-track and across-track



directions (Figure 32 & Figure 33). The dispersion of the along-track errors in Figure 33 suggests however that a per-camera analysis is required, it is on-going. Completion of the time series (started using the partial reprocessing dedicated to validation: 4 days every month between 26/04/16 and 12/03/2017) confirms the slow AL trend (Figure 34).

Performing additional geometric Calibration has to be done in a near future. The required complete version of the GeoCal tool, allowing the Calibration mode, has recently been installed in the MPMF and Geometric Calibration will start has started.

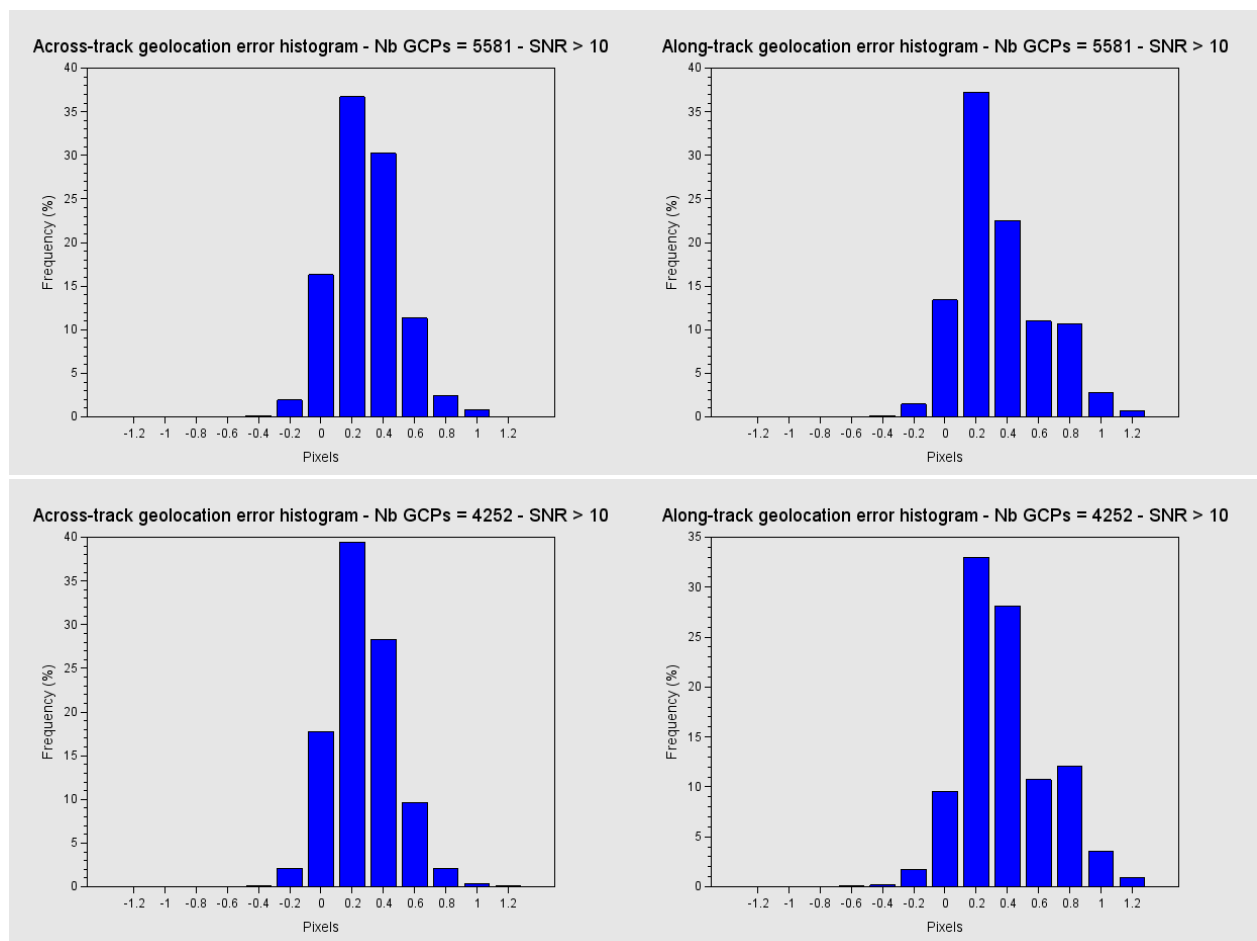


Figure 32: histograms of geolocation errors for the along-track (left) and across-track (right) directions, examples of 28/10/2017 (top) and 22/11/2017 (bottom).

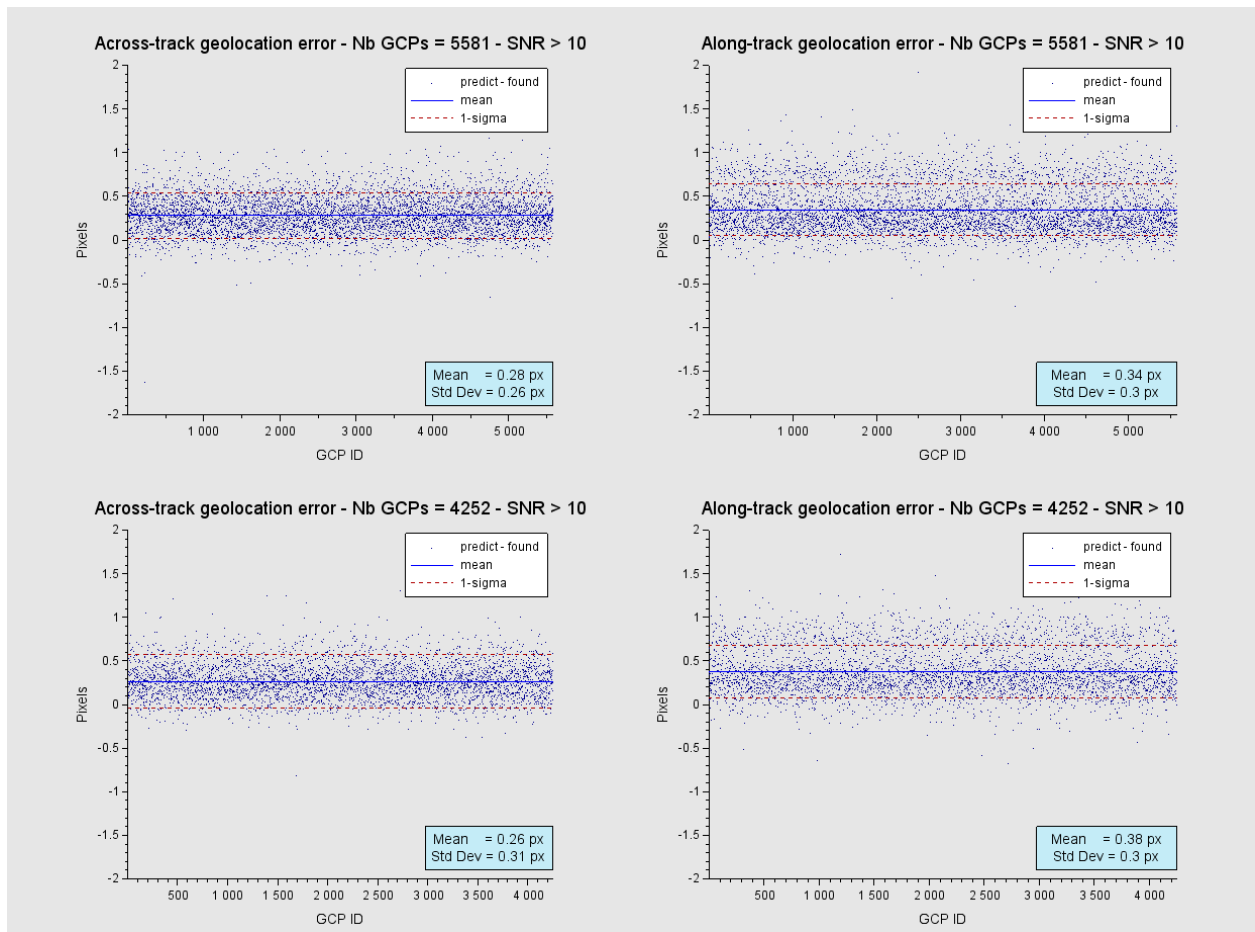


Figure 33: georeferencing error in along-track (left) and across-track (right) directions for all the GCPs, examples of 28/10/2017 (top) and 22/11/2017 (bottom).



Sentinel-3 MPC
S3-A OLCI Cyclic Performance Report
Cycle No. 024

Ref.: S3MPC.ACR.PR.01-024
Issue: 1.0
Date: 30/11/2017
Page: 30

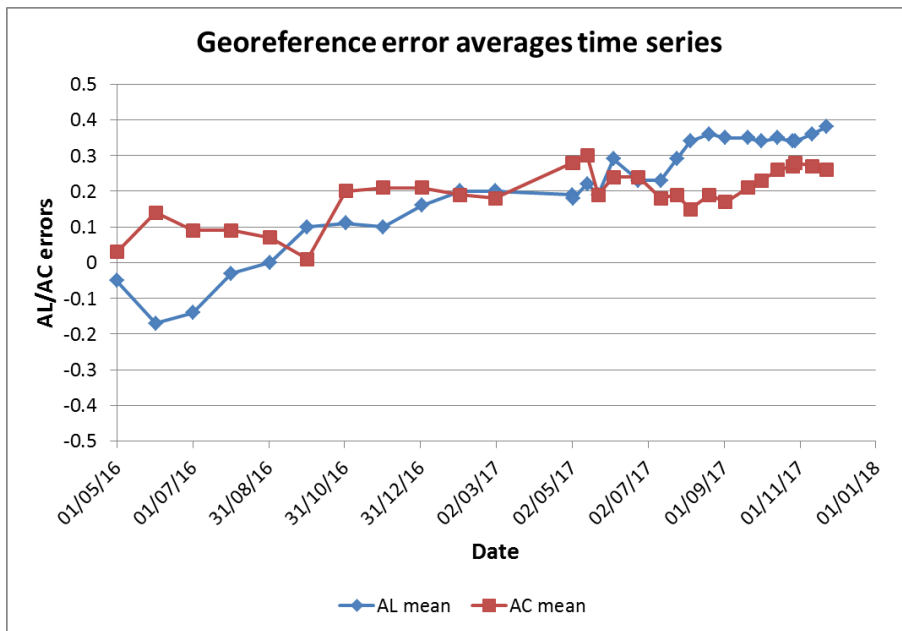



Figure 34: time series of geolocation errors for the along-track (blue) and across-track (red) directions over 18.7 months.

	Sentinel-3 MPC S3-A OLCI Cyclic Performance Report Cycle No. 024	Ref.: S3MPC.ACR.PR.01-024 Issue: 1.0 Date: 30/11/2017 Page: 31
--	---	---

2 OLCI Level 1 Product validation

2.1 [OLCI-L1B-CV-300], [OLCI-L1B-CV-310] – Radiometric Validation

2.1.1 S3ETRAC Service

Activities done

The S3ETRAC service extracts OLCI L1 RR and SLSTR L1 RBT data and computes associated statistics over 49 sites corresponding to different surface types (desert, snow, ocean maximizing Rayleigh signal, ocean maximizing sunglint scattering and deep convective clouds). The S3ETRAC products are used for the assessment and monitoring of the L1 radiometry (optical channels) by the ESLs.

All details about the S3ETRAC/OLCI and S3ETRAC/SLSTR statistics are provided on the S3ETRAC website <http://s3etrac.acri.fr/index.php?action=generalstatistics>

- ❖ Number of OLCI products processed by the S3ETRAC service
- ❖ Statistics per type of target (DESERT, SNOW, RAYLEIGH, SUNGLINT and DCC)
- ❖ Statistics per sites
- ❖ Statistics on the number of records

For illustration, we provide below statistics on the number of S3ETRAC/OLCI records generated per type of targets (DESERT, SNOW, RAYLEIGH, SUNGLINT and DCC).

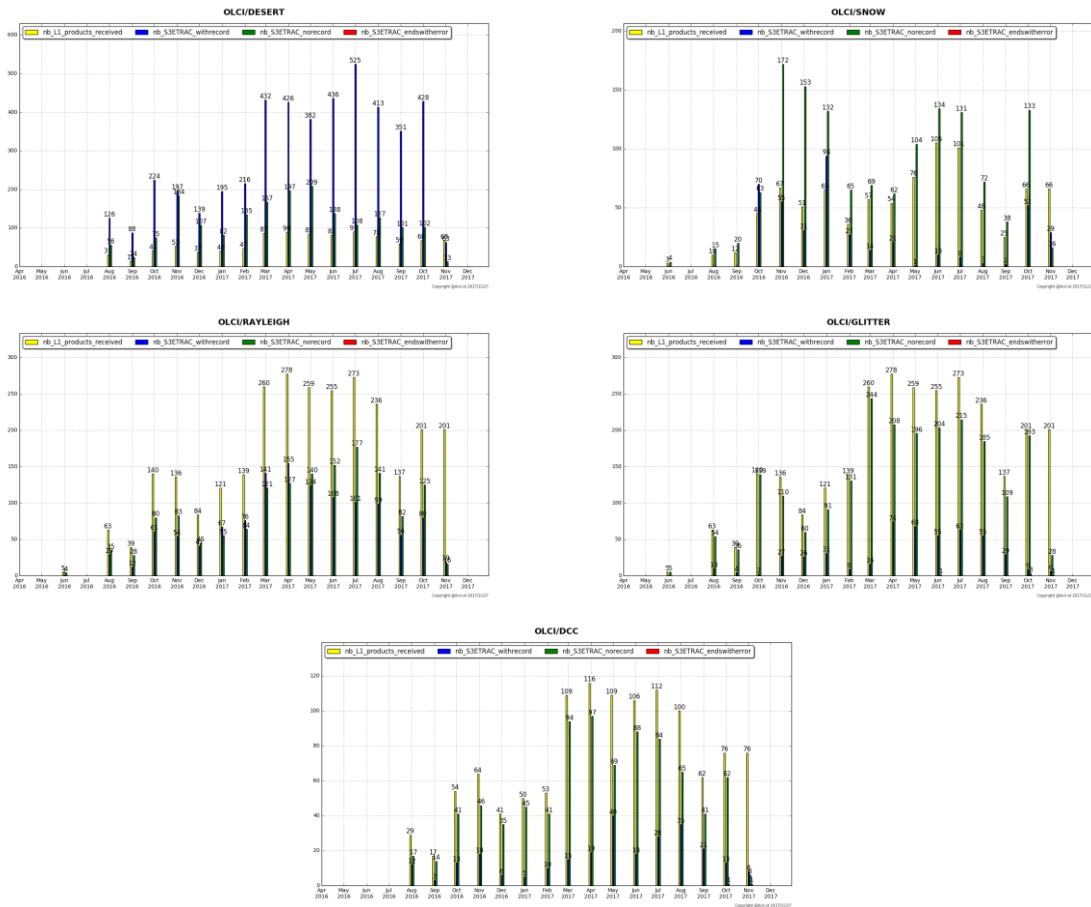


Figure 35: summary of S3ETRAC products generation for OLCI (number of OLCI L1 products Ingested, yellow – number of S3ETRAC extracted products generated, blue – number of S3ETRAC runs without generation of output product (data not meeting selection requirements), green – number of runs ending in error, red, one plot per site type).

2.1.2 Radiometric validation with DIMITRI

Highlights

- ❖ Run Rayleigh and Desert methods over the available products until 25th November 2017.
- ❖ About 44 new products from Cycle-24 were used in this analysis. The results (Rayleigh, Glint and PICS) are consistent with the previous cycle over the used CalVal sites.
- ❖ Good stability of the sensor could be observed, nevertheless, the time-series average shows higher reflectance over the VNIR spectral range with biases of 2%-4% except bands Oa06-Oa09
- ❖ Bands with high gaseous absorption are excluded.
- ❖ The results over Rayleigh and Glint methods need to be consolidated over ocean sites with more products from early mission period (before Dec 2016).



I-Validation over PICS

1. Downloading and ingestion of all the available L1B-LN1-NT products in the S3A-Opt database over the 6 desert CalVal-sites (Algeria3 & 5, Libya 1 & 4 and Mauritania 1 & 2) has been performed until 25th November 2017.
2. The results are consistent overall the six used PICS sites (Figure 36). OLCI reflectance shows a good stability over the mission life-time.
3. The temporal average over the period **April 2016** – November **2017** of the elementary ratios (observed reflectance to the simulated one) shows values higher than 2% (mission requirements) over all the VNIR bands (Figure 37). The spectral bands with significant absorption from water vapour and O₂ (Oa11, Oa13 and Oa14) are excluded.
4. Algeria-3 site shows lower reflectance over the bands Oa17 (865 nm) than the other PICS since May 2017. This event is observed on Sentinel-2/MSI images too. It is most likely related to human/industrial activity in the area.

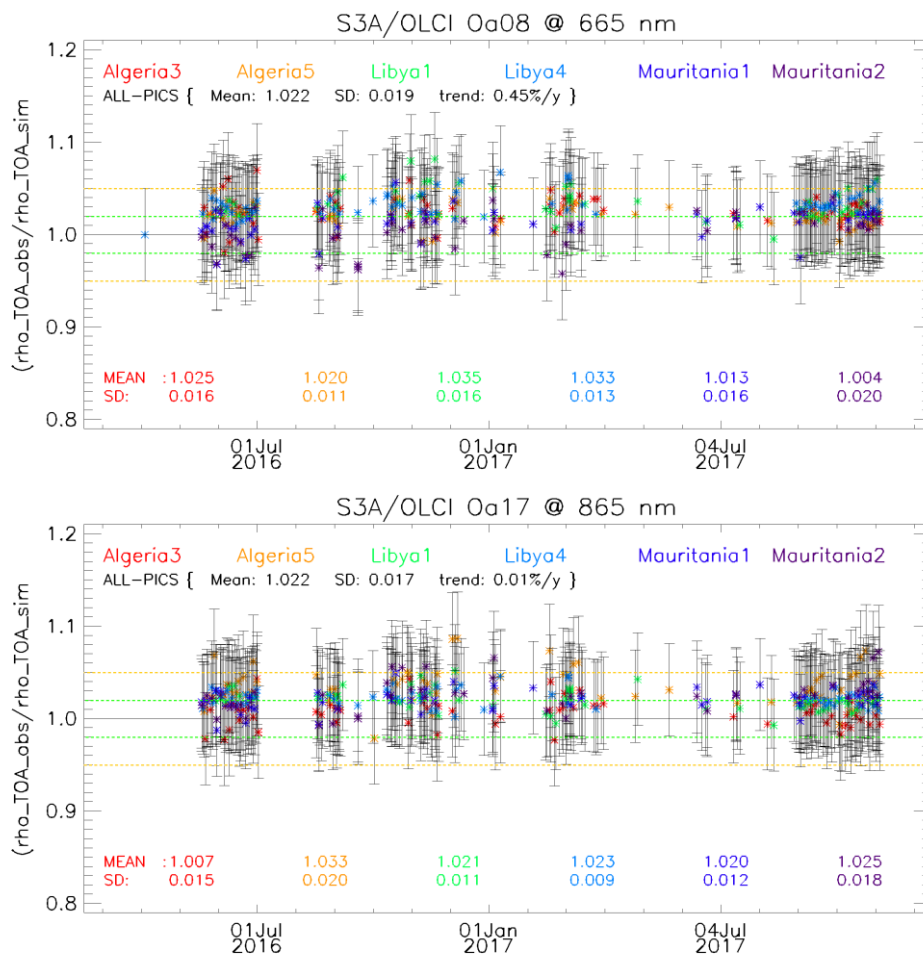


Figure 36: Time-series of the elementary ratios (observed/simulated) signal from S3A/OLCI for (top to bottom) bands Oa03, Oa8 and Oa17 respectively over Six PICS Cal/Val sites. Dashed-green and orange lines indicate the 2% and 5% respectively. Error bars indicate the desert methodology uncertainty.

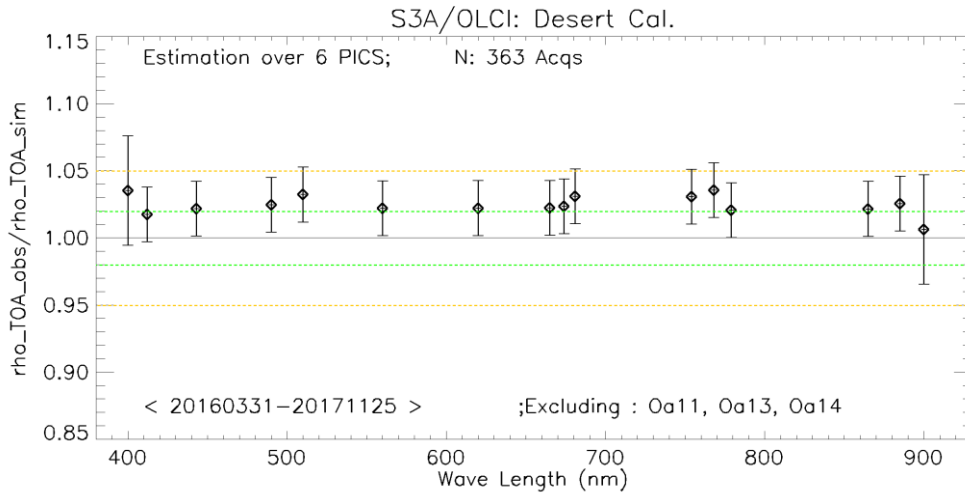


Figure 37: The estimated gain values for S3A/OLCI over the 6 PICS sites identified by CEOS over the period April 2016 – October 2017 as a function of wavelength. Dashed-green and orange lines indicate the 2% and 5% respectively. Error bars indicate the desert methodology uncertainty.

II-Intercomparison S3A/OLCI, S2A/MSI and Aqua/MODIS over PICS

X-mission Intercomparison with MSI-A and MODIS-A is performed until November 2017. Figure 38 shows time-series of the elementary ratios from S2A/MSI, Aqua/MODIS and S3A/OLCI over the LYBIA4 site over the period April-2016 until November -2017.

We observe a clear stability over both sensors, associated with higher reflectance from OLCI wrt to MSI and higher fluctuation of MODISA wrt to MSI and OLCI.

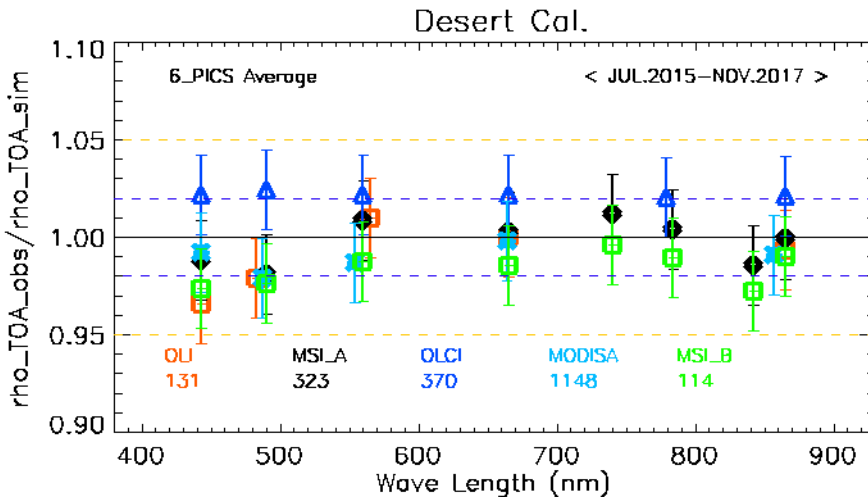


Figure 39 shows the estimated gain over the different time-series from different sensors (MODISA, MSIA, MSIB, OLCI and OLI) over PICS for the common bands with S2A/MSI. The spectral bands with significant absorption from water vapor and O₂ are excluded. Again Figure 31 confirms a systematic higher reflectance of OLCI wrt MSI and MODISA.

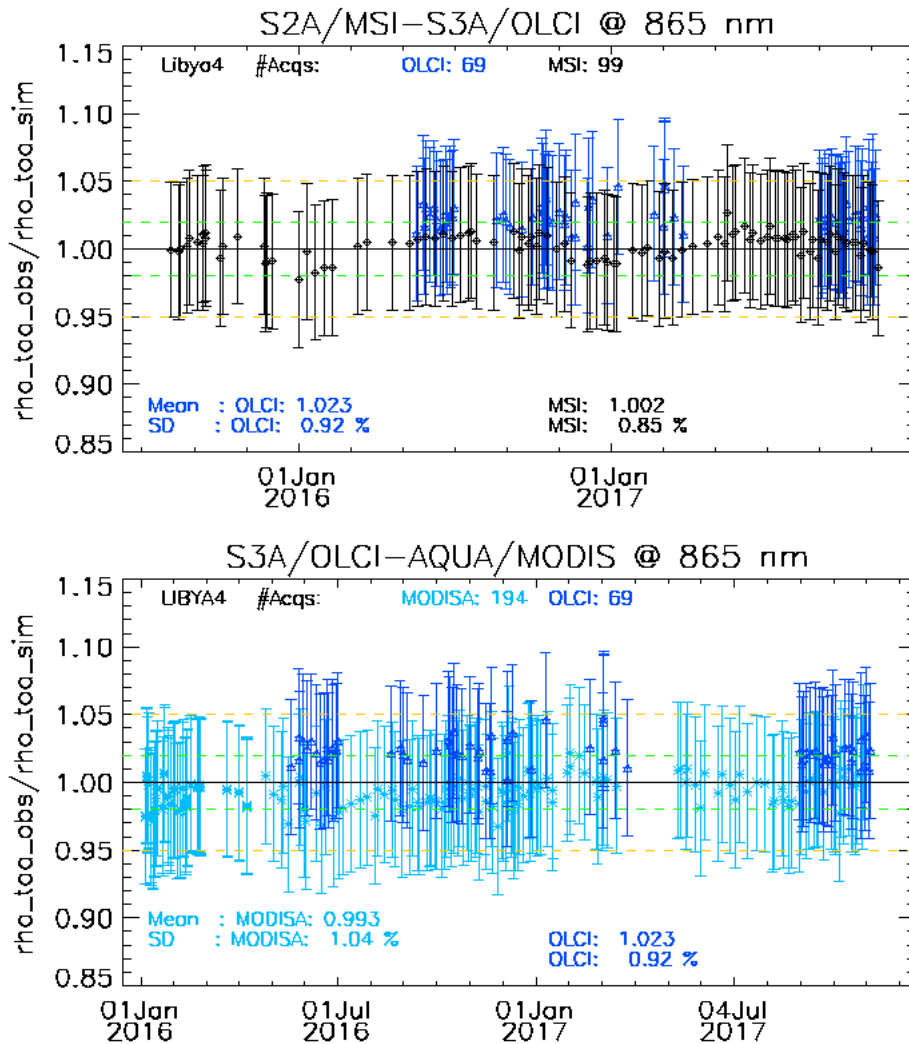


Figure 38: Time-series of the elementary ratios (observed/simulated) signal from (black) S2A/MSI, (blue) S3A/OLCI, and (Cyan) MODIS-A for band Oa17 (865nm) over the LIBYA4 site. Dashed-green and orange lines indicate the 2% and 5% respectively. Error bars indicate the desert methodology uncertainty.

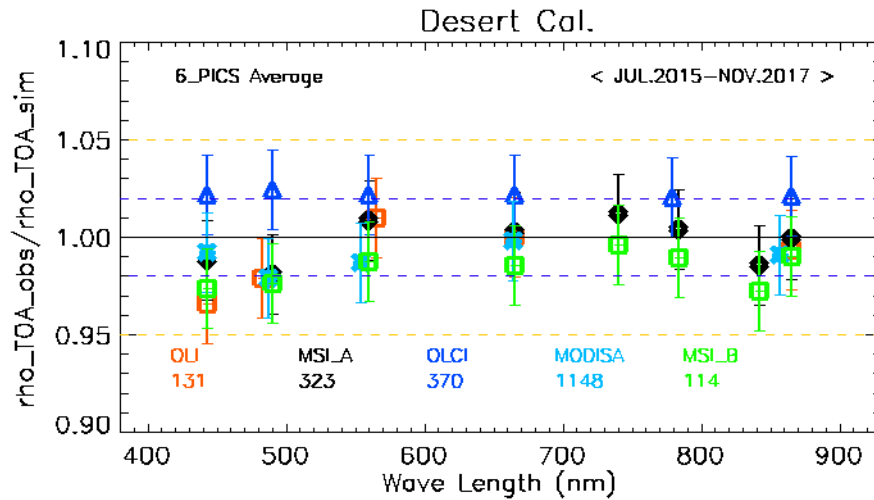


Figure 39: The estimated gain values (observed-signal / simulated-signal) averaged over different period from different sensors over PICS as function of wavelength. The number of used-acquisitions for each sensor within the period July 2015-October 2017 is indicated in the plot-legend.

III-Validation over Rayleigh

Rayleigh method has been performed over the available mini-files on the Opt-server until the cycle-24 period. The results produced with the configuration (ROI-AVERAGE) are consistent with the previous results of PICS method and from Cycles 22 & 23. While bands Oa01-Oa05 display a bias values between 2%-5%, bands Oa6-Oa9 exhibit biases within 2% (mission requirements) (Figure 40).

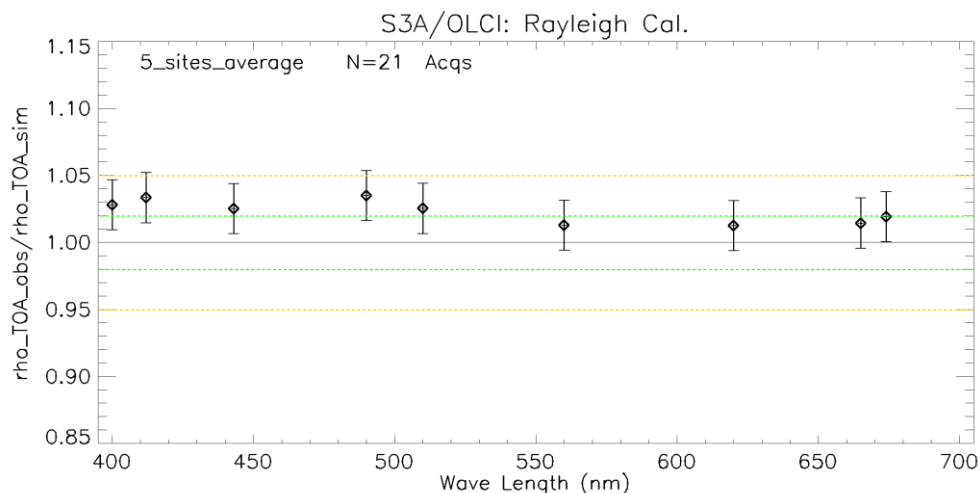


Figure 40: The estimated gain values for S3A/OLCI over the 6 Ocean CalVal sites (Atl-NW_Optimum, Atl-SW_Optimum, Pac-NE_Optimum, Pac-NW_Optimum, SPG_Optimum and SIO_Optimum) over the period December 2016 – October 2017 as a function of wavelength. Dashed-green, and orange lines indicate the 2%, 5% respectively. Error bars indicate the methodology uncertainty.

IV-Validation over Glint

Glint calibration method with the configuration (ROI-PIXEL) has been performed over the period December 2016 – end October 2017 from the available mini-files. The outcome of this analysis shows a good consistency with Rayleigh and the desert outputs over the NIR spectral range (see Figure 41).

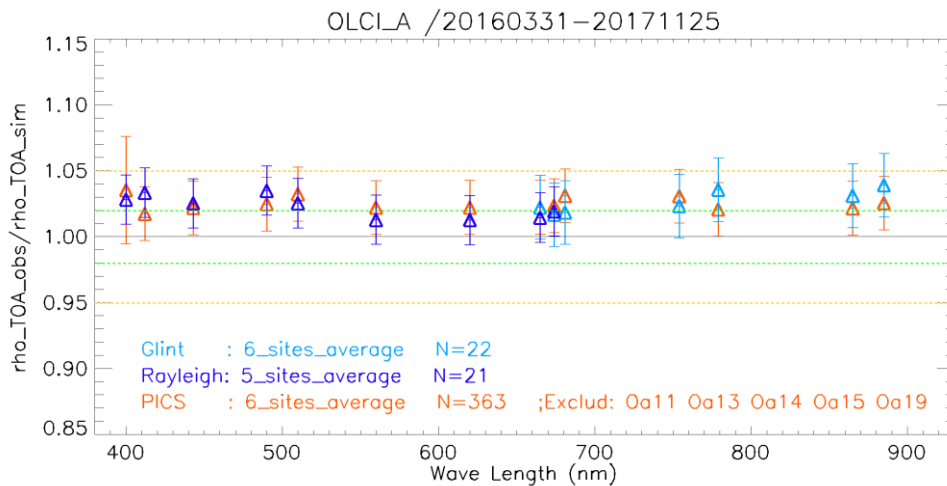


Figure 41: The estimated gain values for S3A/OLCI from Glint, Rayleigh and PICS over the period April 2016 – November 2017 for PICS and December 2016–October 2017 for Glint and December 2016–November 2017 for Rayleigh methods as a function of wavelength. We use the gain value of Oa8 from PICS method as reference gain for Glint. Dashed-green and orange lines indicate the 2% and 5% respectively. Error bars indicate the methods uncertainties.

2.1.3 Radiometric validation with OSCAR

The OSCAR Rayleigh method has been applied to the S3ETRAC data from the 6 oceanic calibration sites listed in Table 2, over the period January 2017 – September 2017. The average OSCAR Rayleigh results and the standard deviation calibration are shown below (Table 3, Figure 42), respectively for the whole period (i.e. Jan 2017 till Sept 2017) and for three most recent months which have been processed (i.e. Jul 2017 till Sept 2017). Please note that the OSCAR Rayleigh results for band Oa01 have to be considered with care due to larger uncertainty in the Radiative transfer calculation. When only considering the latest 3 months observed biases are less with for Oa01-Oa05 bias values between 2%-4%, for Bands Oa6-Oa9 observed biases are less (well within the 2 % mission requirement). It is at the moment unclear if the reduced biases for the latest results are related to the instrument or if it is due to possible seasonally dependent uncertainties in OSCAR Rayleigh approach.



Table 2: S3ETRAC Rayleigh Calibration sites

Site Name	Ocean	North Latitude	South Latitude	East Longitude	West Longitude
PacSE	South-East of Pacific	-20.7	-44.9	-89	-130.2
PacNW	North-West of Pacific	22.7	10	165.6	139.5
PacN	North of Pacific	23.5	15	200.6	179.4
AtIN	North of Atlantic	27	17	-44.2	-62.5
AtIS	South of Atlantic	-9.9	-19.9	-11	-32.3
IndS	South of Indian	-21.2	-29.9	100.1	89.5

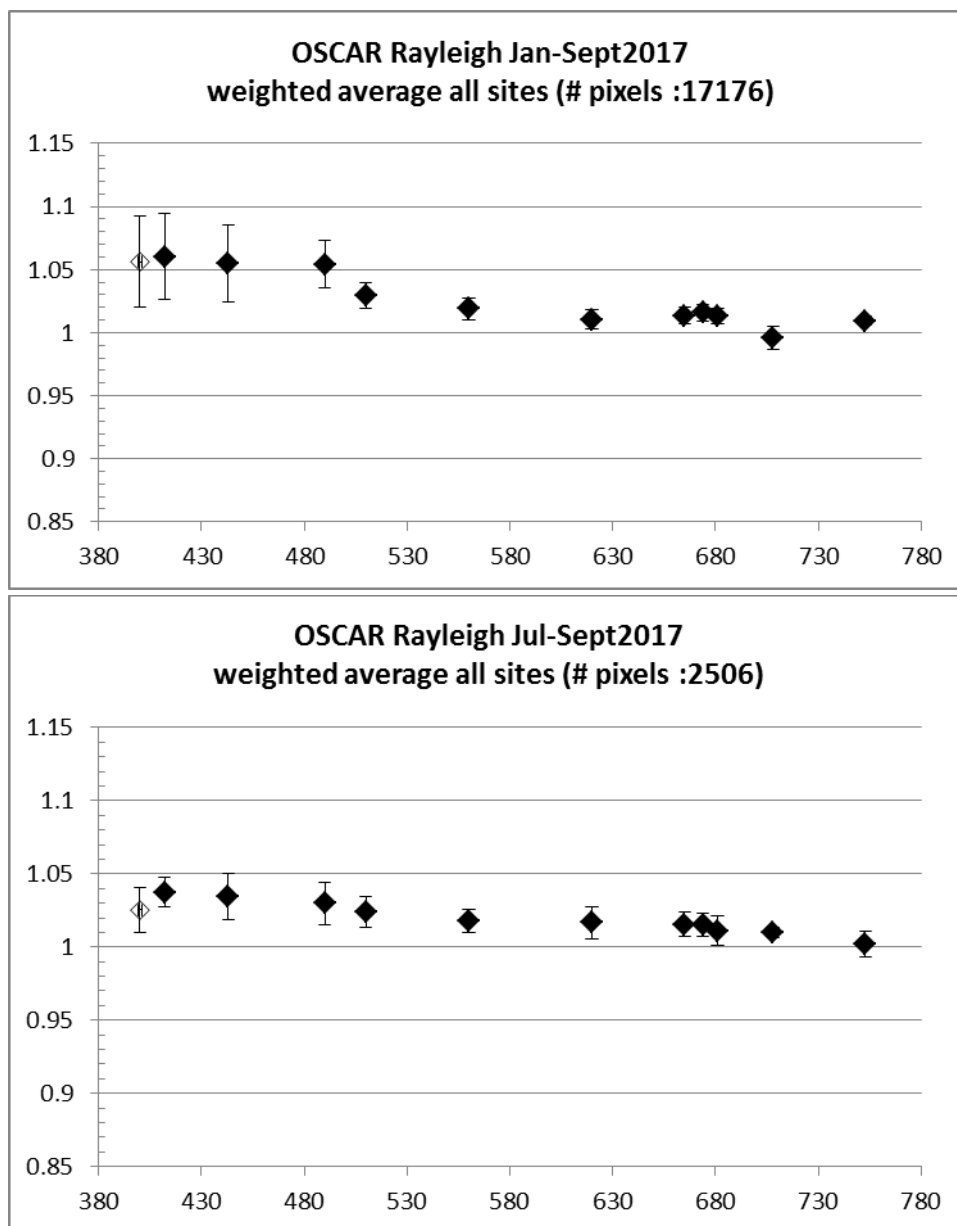


Figure 42: OSCAR Rayleigh Calibration results: weighted average over all sites and standard deviation for (a) period Jan 2017 till Sept 2017 and (b) July 2017 till Sept 2017


	Sentinel-3 MPC S3-A OLCI Cyclic Performance Report Cycle No. 024	Ref.: S3MPC.ACR.PR.01-024 Issue: 1.0 Date: 30/11/2017 Page: 39
--	---	---

Table 3: OSCAR Rayleigh Calibration results: weighted average over all sites and standard deviation for period Jan 2017 till Sept 2017 and July 2017 till Sept 2017

S3A-OLCI band	Wavelength(nm)	Oscar Rayleigh Over Jul 2017-Sept 2017		Oscar Rayleigh Over Jan2017-Sept 2017	
		Weighted average	standard deviation	Weighted average	standard deviation
Oa01	400	1.0253	0.0157	1.0563	0.0360
Oa02	412	1.0374	0.0103	1.0603	0.0339
Oa03	443	1.0344	0.0157	1.0546	0.0304
Oa04	490	1.0299	0.0144	1.0542	0.0192
Oa05	510	1.0240	0.0104	1.0295	0.0102
Oa06	560	1.0177	0.0080	1.0190	0.0088
Oa07	620	1.0169	0.0110	1.0105	0.0078
Oa08	665	1.0156	0.0082	1.0135	0.0066
Oa09	674	1.0151	0.0083	1.0157	0.0064
Oa10	681	1.0112	0.0099	1.0131	0.0064
Oa11	709	1.0100	0.0039	0.9955	0.0090
Oa12	754	1.0020	0.0091	1.0095	0.0037

2.2 [OLCI-L1B-CV-320] – Radiometric Validation with Level 3 products

There has been no new result during the cycle. Last figures (cycle 20) are considered valid

3 Level 2 Land products validation

3.1 [OLCI-L2LRF-CV-300]

In the frame of the validation of OTCI and OGVI, a specific study has been conducted regarding the impact of Cloud masking on the Land products. **The current report presents a consolidated version of the results and conclusion with respect to that of Cycle 23 report.**

Study Sites

Seven different study areas were chosen for this study. They were chosen to cover a range of land cover conditions including; desert, bare soil, vegetated regions, tropical forests and an ice sheet. The imagery was downloaded from the SciHub data hub. Both L-1 and L-2 datasets were downloaded for each of the scenes. The scene details can be seen within Table 4.

Table 4: Scene definitions

Study Site	Date of product
France - Europe	28/09/2017
Los Angles - North America	25/09/2017
Queensland - Australia	02/10/2017
Denmark - Northern Europe	14/08/2017
Greenland	04/10/2017
Congo	30/07/2017
Rondonia – Brazil	27/08/2017

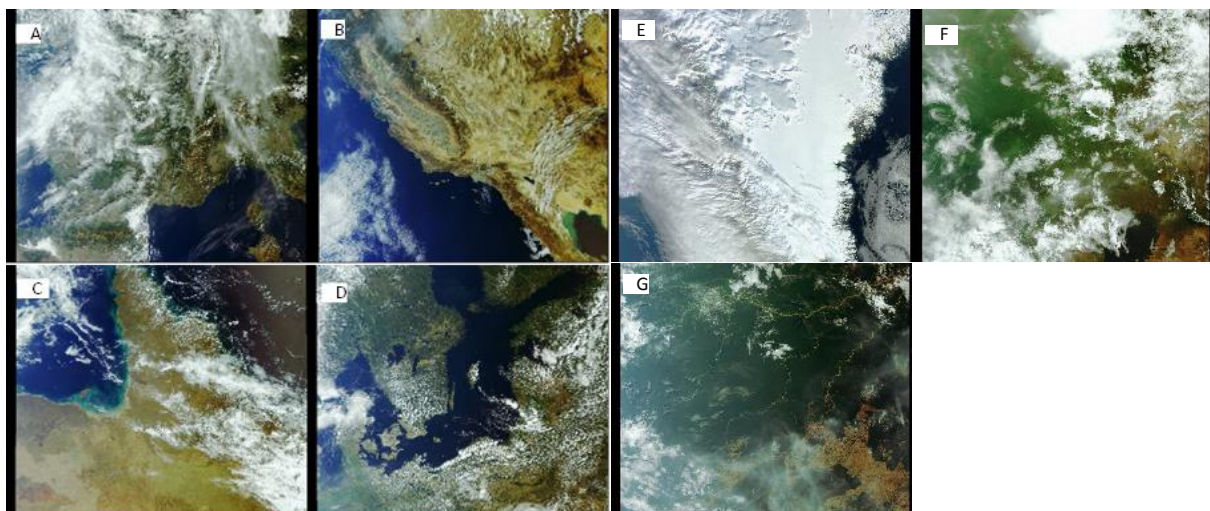


Figure 43: RGB composites of the study sites. A) France B) Los Angles C) Queensland, Australia D) Denmark E) Greenland F) Congo G) Rondonia

Analysis

The total number of pixels identified by each of the different cloud masks can be seen within Table 5. The higher numbers within the Greenland image can be expected due to the difficulty in distinguishing cloud from snow using coarse resolution imagery due to the similar spectral signals.

Table 5: Number of pixels identified by the different cloud masks within the images.

	Cloud		Cloud - Ambiguous		Cloud - Margin	
	Number of pixels	% of image	Number of pixels	% of image	Number of pixels	% of image
France - Europe	9745347	48.96%	141548	0.71%	2236645	11.24%
Los Angles - North America	2214502	11.13%	306970	1.54%	1750391	8.79%
Queensland - Australia	4824985	24.24%	174179	0.88%	2577830	12.95%
Denmark - Northern Europe	3777443	18.98%	193917	0.97%	4459148	22.40%
Greenland	14087467	70.78%	108262	0.54%	2744620	13.79%
Congo	9417263	47.32%	156567	0.79%	1870915	9.40%
Rondonia	1651842	8.30%	105872	0.53%	1272816	6.40%

One observation was that in some situations sections of inland water, such as rivers or edges of lakes, were being classified as cloud or cloud ambiguous pixels as well as inland water. The total number of pixels that were classified as both inland water and cloud can be seen within Table 6. The image focused over Denmark had the highest number of inland water pixels identified within each of the different cloud masks. It is important to note, that in some instances the classification of both inland water and cloud was correct. However, there were instances, as seen within Figure 44, where the pixels were incorrectly identified as cloud. This had implications on OTCI estimates along the banks of rivers as additional pixels nearby were normally classified as ambiguous clouds and as such were removed from OTCI calculations. This issue was present within all of the images involved within the study.

Table 6: Number of pixels that were classified as both inland water and cloud.

	Inland water + Cloud	Inland water + Ambiguous cloud	Inland water + Cloud margin
France - Europe	81312	1766	16198
Los Angles - North America	33084	2053	26550
Queensland - Australia	13929	824	7044
Denmark - Northern Europe	120436	6264	110332
Greenland	71416	149	2069

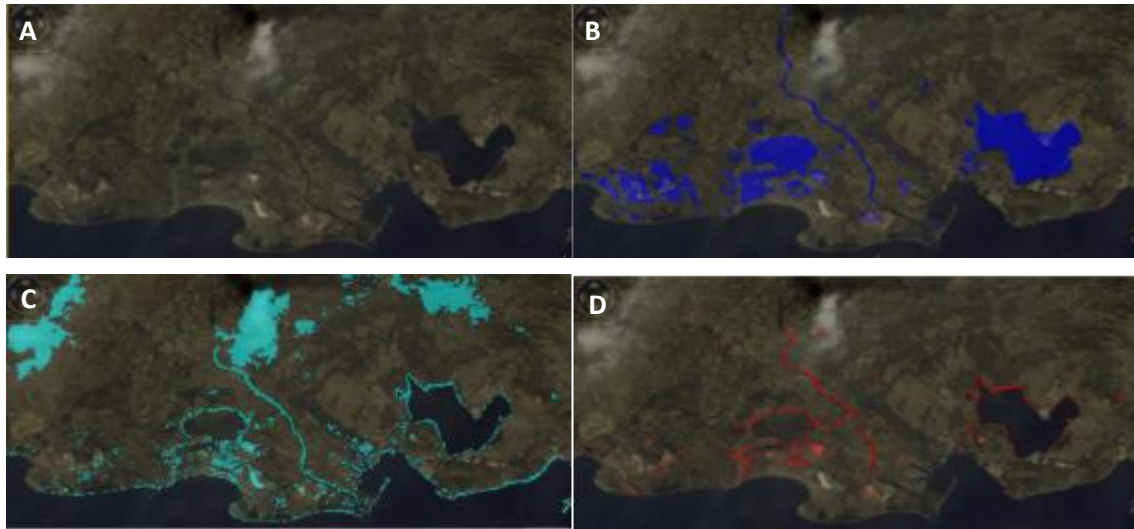


Figure 44: A) RGB image of the River Rhone, France (43°32'02" N, 4°43'06" E). B) Inland water flagged pixels. C) Cloud flagged Pixels. D) Pixels classified as both inland water and cloud.

Within the Queensland imagery there were patches of identified cloud upon the edges of sections of cloud that were not being correctly classified by the cloud tagging. An example of this can be seen within Figure 45. Highlighted within the red square are areas of cloud that have not been detected, therefore OTCI values have been produced for these pixels as shown in Figure 45.

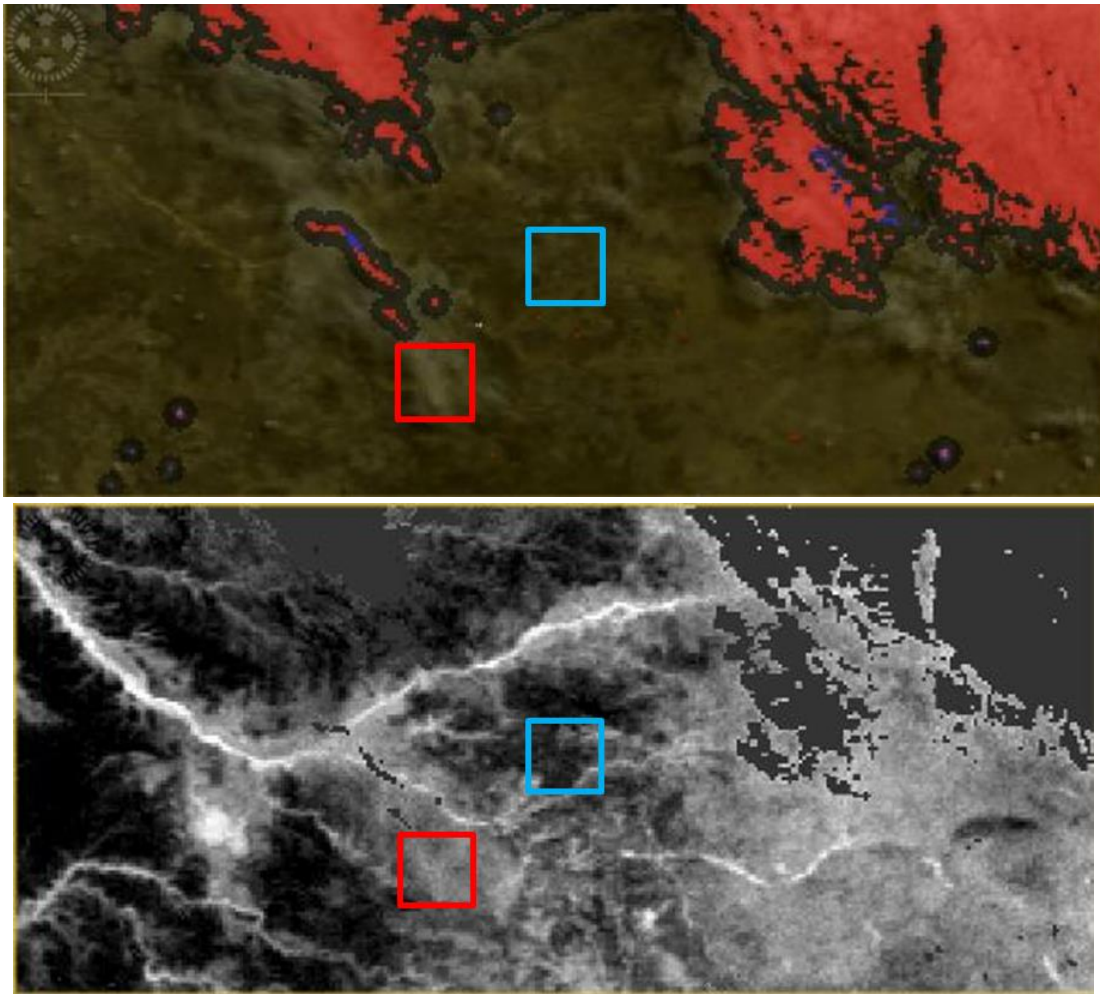


Figure 45: RGB and OTCI bands for Queensland Australia (17°26'04" S, 143°47'15" E).

50 pixels were selected from each of the areas identified in Figure 45. The blue square indicates an area of bare soil and the red square shows an area of cloud. The resulting histograms showing the spread of the different OTCI values recorded within these sections can be seen in Figure 46. The range of OTCI values is substantially lower for the section of cloud in comparison to the bare soil, with ranges of 0.23 and 0.51 respectively. This uniformity in OTCI values for the cloud can be seen within the histogram in Figure 46.

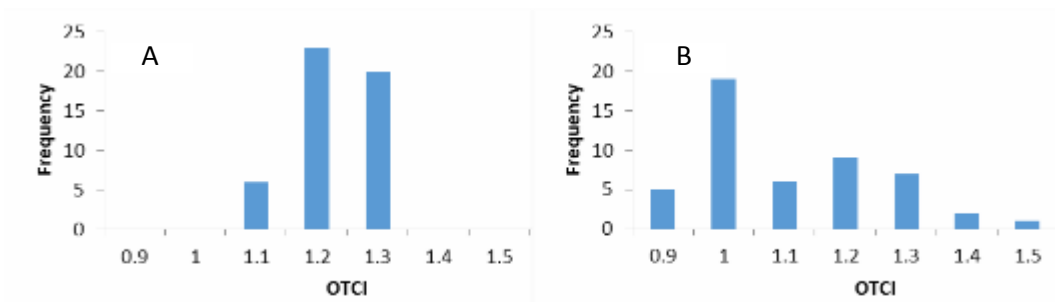


Figure 46: A) Histogram of OTCI values for cloud pixels. B) Histogram of OTCI values for bare soil pixels.



Spectrum View

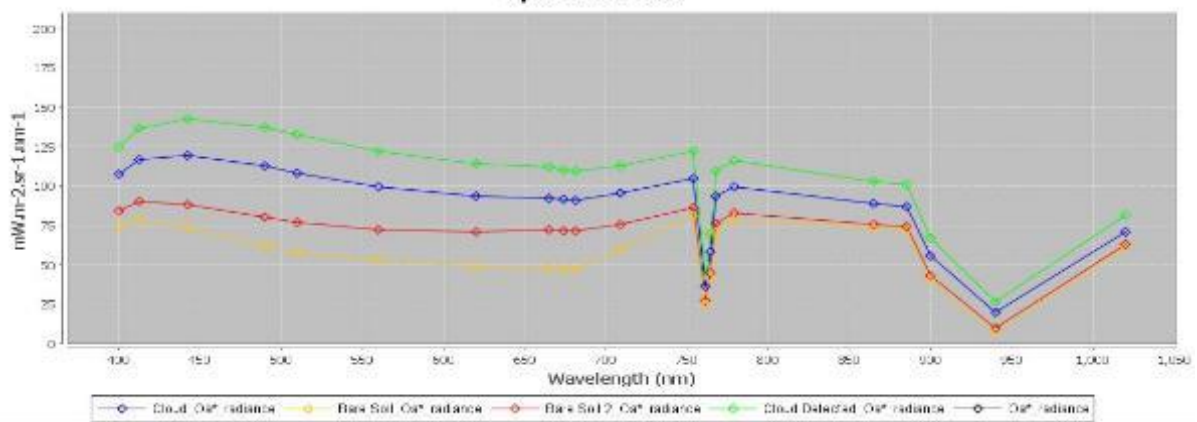


Figure 47: Spectral signals of the different classifications within the image Queensland Australia (17°26'04" S, 143°47'15" E).

The spectral signals for different sections of the image can be seen within Figure 47. The areas of dark and light soil have spectra's with a similar shape but with lower reflectance values for the darker soil. The spectra profiles of areas of identified cloud and non-identified cloud are similar in shape. Therefore, this shows that the thresholds for detecting cloud may need to be adapted to reflect the lower reflectance values obtained from cloud within the imagery. Within this image there are sections of haze cloud that are not be detected by the flagging.

Conversely in the Los Angeles image areas of bare soil were being misclassified as cloud when no cloud was present due to being a bright white soil. An example of this is shown in Figure 49. This led to pixels being unnecessarily removed from the OTCI band. However, it is important to note that the spectral signals between the area of non-detected cloud in Figure 47 and the misidentified cloud in Figure 48 have very similar reflectance values. Therefore further investigation will be carried out to properly assess the effectiveness of the cloud tagging over bare soils.

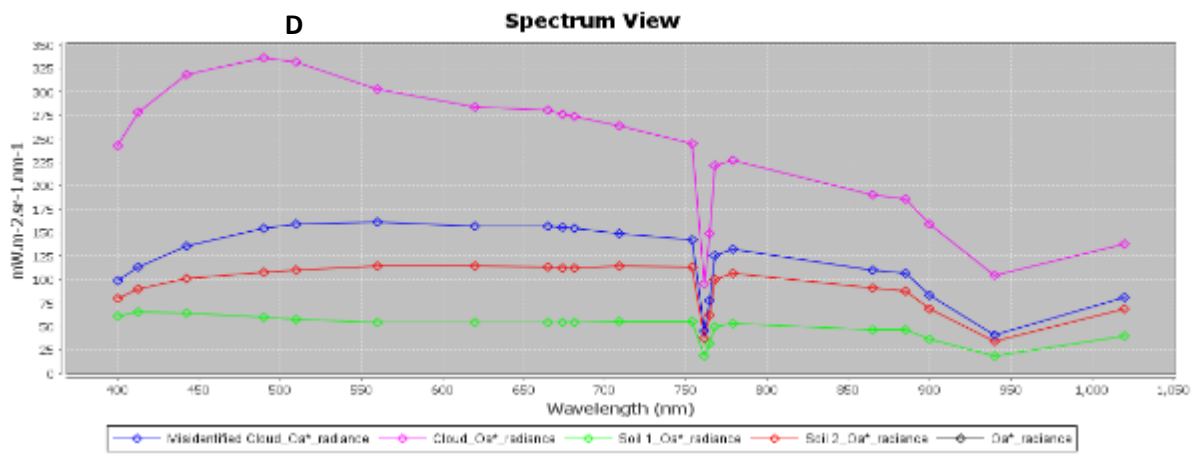
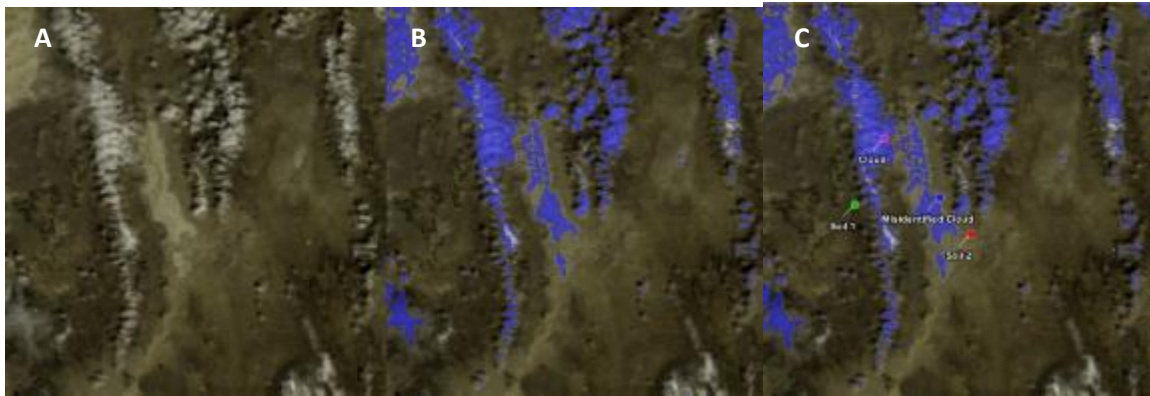


Figure 48: A) RGB composite (39°39'01" N, 115°54'46" W) B) Cloud mask C) Location of Pins. D) Spectral signals of the different pins.

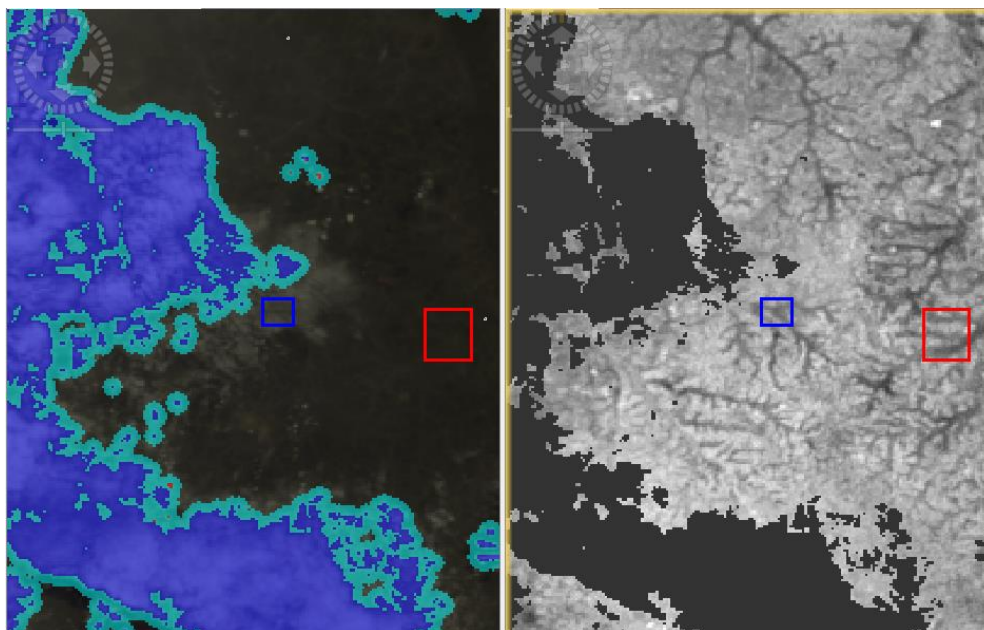


Figure 49: RGB and OTCI bands for the Congo (0°55'28" N, 32°37'17" E). Within the RGB image the Cloud, Cloud_ambiguous and Cloud_edge masks have been turned on.

A similar issue of haze not being detected at the edge of cloud sections was observed in the Congo imagery. 140 pixels were selected from both of the areas shown in Figure 49. The areas highlighted show areas of forest (red) and cloud (blue). These areas were selected as they are homogeneous and were not detected as cloud as shown in Figure 49.

Histograms were produced showing the distribution of values for OTCI and OGVI for each section. For both OTCI and OGVI the section of cloud which was not identified had lower values recorded, as seen in Figure 50. Cloud had a larger range of OTCI values in comparison to the forest pixels with ranges of 1.78 and 0.72 respectively. There was also a greater spread of OGVI value recorded for cloud pixels in comparison to forest pixels, with all of the forest pixels recording OGVI values between 0.54 and 0.35. The spectral signals for the different ROIs can be seen within Figure 51.

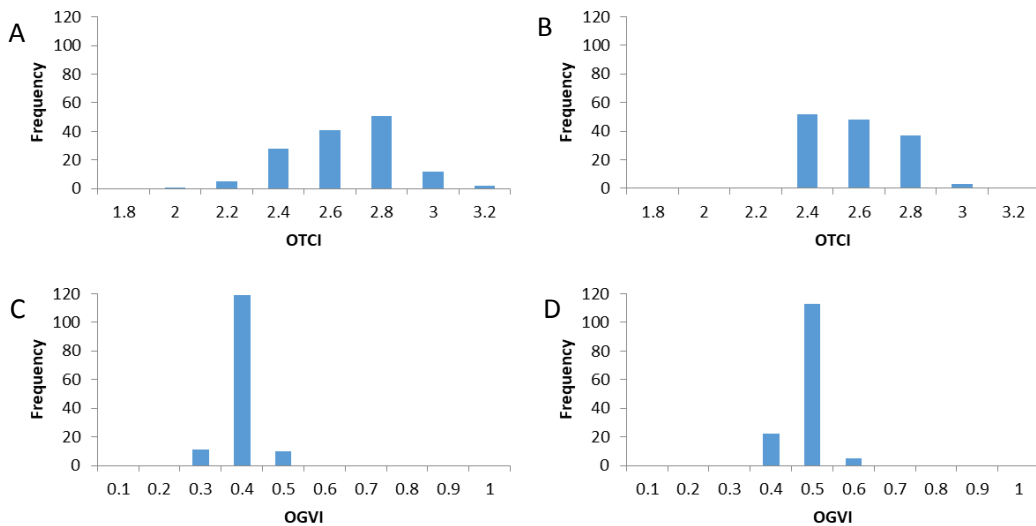


Figure 50: A) Histogram of OTCI values for cloud pixels. B) Histogram of OTCI values for forest pixels. C) Histogram of OGVI values for cloud pixels. D) Histogram of OGVI values for forest pixels

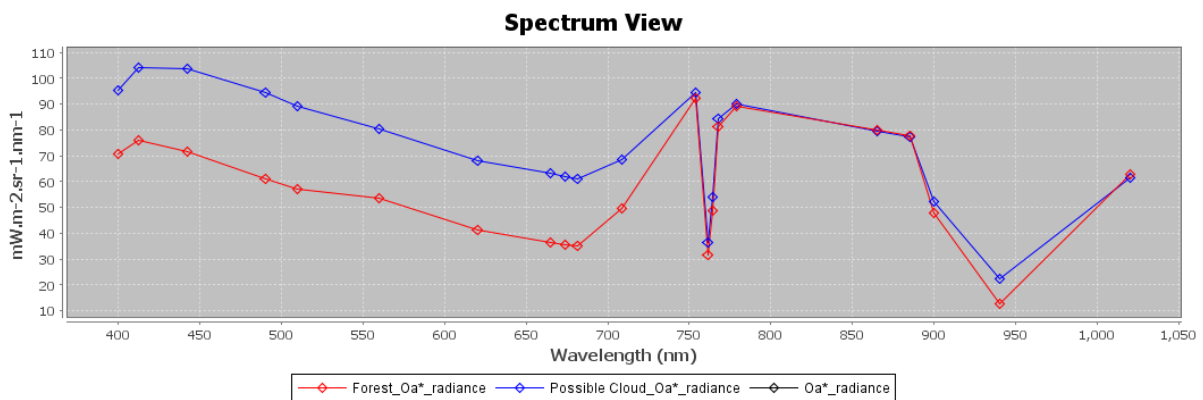


Figure 51: Spectral signals taken from the ROIs identified in Figure 7.

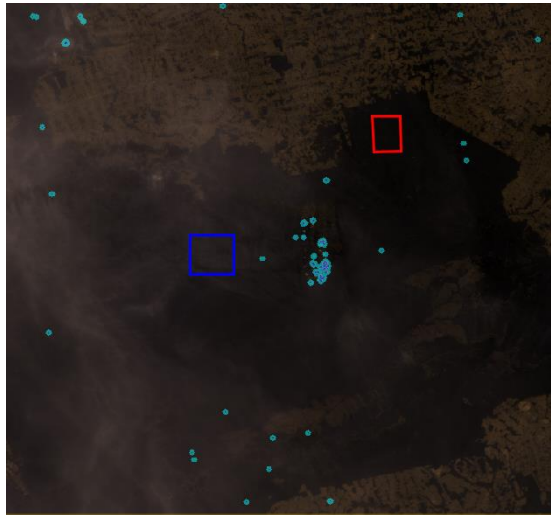


Figure 52: RGB image of the ROI in Rondonia, Brazil (10°58'10" S, 64°00'12" W).

Figure 10:

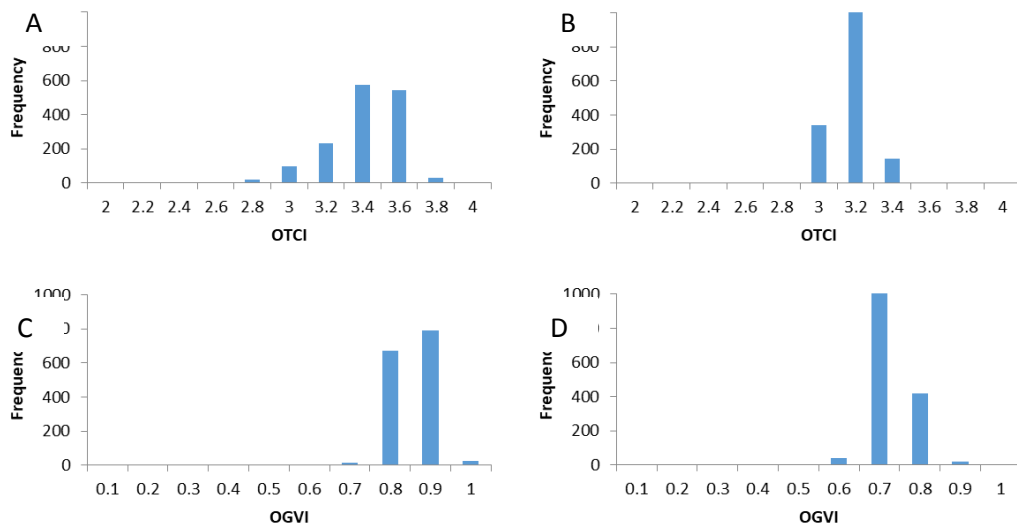


Figure 53: A) Histogram of OTCI values for cloud pixels. B) Histogram of OTCI values for forest pixels. C) Histogram of OGVI values for cloud pixels. D) Histogram of OGVI values for forest pixels.

A similar investigation was carried out to see the impact that unidentified areas of cloud have upon OTCI and OGVI values within a forested region in Rondonia, Brazil. The areas chosen for study can be seen in Figure 52. The areas highlighted show areas of forest (red) and cloud (blue).

However, in this instance there is little difference between the OTCI and OGVI values for the cloud and forest pixels. The cloud pixels have a larger range of OTCI values with a maximum of 3.69 and a minimum value of 2.25. The forest pixels have a maximum value of 3.78 and a minimum value of 2.38.

There is a slightly different pattern in the spread of OGVI values between the cloud and forest pixels. 66% of the forest pixels have an OGVI value between 0.6 - 0.7 and 96% of the forest pixels fall between the 0.6-0.8 OGVI values. In comparison, 97% of the cloud pixels have OGVI values between 0.7 – 0.9. The spectral signals of the two different sites are very similar as shown by Figure 54.

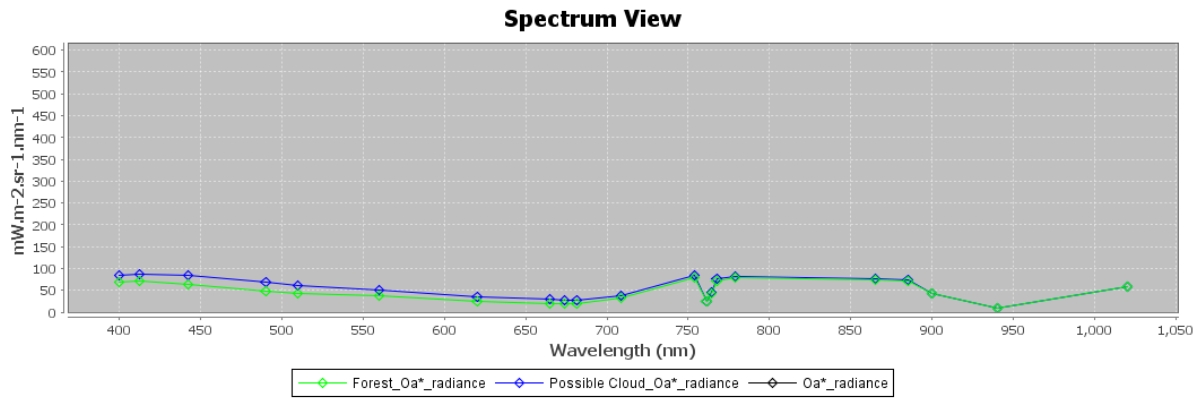


Figure 54: Spectral signals of a cloud and forest pixel.

Summary

Four separate issues that will require further investigation have been found during this study. There is the known issue of cloud detection over ice sheets as observed over Greenland. A second issue is where pixels are being flagged as both cloud and inland water pixels when they should only be inland water. This occurred around the edges of lakes and rivers and as a result OTCI values were not available for pixels adjacent to these features. In some of the images sections of haze/sparse cloud were not being detected by the flagging, these sections normally happened in patches at the edges of detected cloud. Furthermore, in sparsely vegetated environments some areas of bright white soil were being incorrectly classified as cloud pixels due to having similar spectral signals as the cloud in the image. It is still too early to recommend any changes to the cloud flagging algorithm until further investigation has been carried out upon these last two issues.

3.2 [OLCI-L2LRF-CV-410 & OLCI-L2LRF-CV-420] – Cloud Masking & Surface Classification for Land Products

A quantitative validation of the current OLCI cloud flag was conducted using a dedicated pixel collection (PixBox dataset). After significant efforts had been made to improve the OLCI cloud masking over water and land and the new version had been put to production for the S3VT and at the PDGS in July. The processing of an OLCI validation dataset has been finished in October. Afterwards, the PixBox dataset had been used to make a quantitative validation of the OLCI cloud mask.

For the PixBox validation dataset 10000 pixels have been collected. The collected pixels are well distributed temporally and spatially.

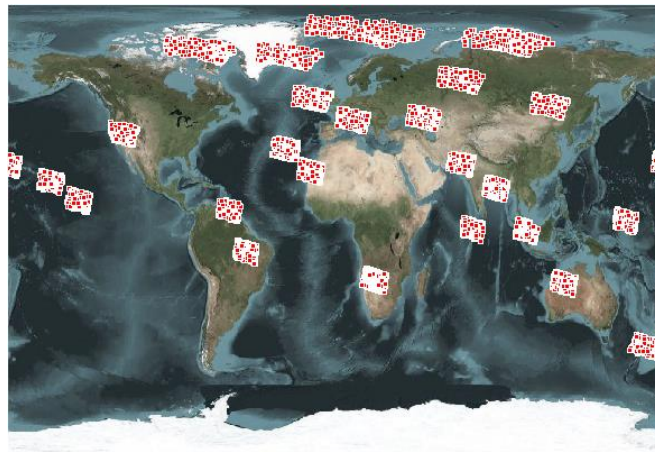


Figure 55: spatial distribution of the PiBox validation dataset samples

The collection distinguishes between different cloud types which have been combined to one cloud category for the validation. The same has been done for the OLCI cloud flags (CLOUD, CLOUD_AMBIGUOUS, CLOUD_MARGIN), as there is no straightforward correlation between the collected cloud types and the three OLCI cloud flags.

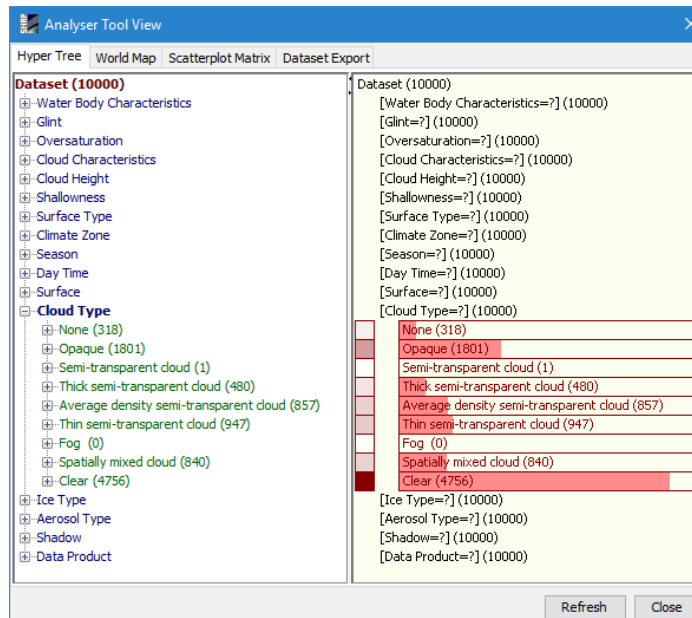


Figure 56: PiBox validation dataset samples Cloudiness classification overview

This means there have only been two classes been used in the validation process. These classes are clear and cloud. For the PiBox dataset the three semi-transparent cloud classes as well as opaque pixels have been combined to the class “**Cloud**” while the collected clear pixels represent the “**Clear**” observations. The PiBox dataset is represented as “**In-Situ Database**” in the confusion matrices and plotted on horizontal axis. The OLCI cloud flags (CLOUD, CLOUD_AMBIGUOUS and CLOUD_MARGIN) have been

combined the class “**CLOUD**” and all pixels not affected by any of these flags has been classified as “**CLEAR**”. The extracted OLCI pixels are represented as “**OLCI FR**” and plotted on the vertical axis.

The validation of the cloud flag over all surfaces (land & water) has shown an overall accuracy (OAA) of over 86% and an user accuracy (UA) for clear pixels of over 92%. The level of significance (0.72) is substantial. From the user perspective the cloud flags have a good accuracy in identifying clear observations, but from the producer perspective there is room for improvements, as the producer accuracy (PA) of clear pixels is only a little above 81%. This means, there is a commission error of clear pixels of above 19% and an omission error of cloud pixels of 8.1%.

OLCI LFR cloud val. - all surface (Insitu 1-5 vs CLD Flags)
In-Situ Database

		Class	Clear	Cloud	Sum	U A	E
OLCI FR		CLEAR	3856	330	4186	92.1	7.9
		CLOUD	900	3756	4656	80.7	19.3
		Sum	4756	4086	8842		
		P A	81.1	91.9		OAA:	86.09
	E	18.9	8.1				

Scotts Pi: 0.721

Krippendorfs alpha: 0.721

Cohens kappa: 0.722

Figure 57: Validation dataset Confusion Matrix for all underlying surfaces

Although there is room for improvements, the current version of the cloud flag is a strong improvement compared to the previous version without the neural net. The previous version had an OAA of only 83.6% and a user accuracy for clear pixels of 91%. The commission error of clear pixels, with nearly 23% was also a bit bigger compared to the current version, as well as the omission error of cloud pixels with 8.7%.

When analyzing only land surfaces the accuracies are distributed a bit different. The OOA is a bit lower (85%) while the UA for clear pixels is a lot higher, with only 97%. The omission error of cloud pixels over water is 4% lower (4%) compared to all surfaces (8.1%). On the other hand, the commission error of clear pixels increases over land surfaces nearly 8%. With 27% the commission error over land is relatively high, but as previous analyses have shown, the commission error occurs predominantly over bare surfaces which do not have values for OTCI or OGV. However, here is some room for improvement.


OLCI LFR cloud val. - land surface (Insitu 1-5 vs CLD Flags)
In-Situ Database

		Class	Clear	Cloud	Sum	U A	E
OLCI LFR		CLEAR	2178	67	2245	97.0	3.0
		CLOUD	596	1603	2199	72.9	27.1
		Sum	2774	1670	4444		
		P A	78.5	96.0		OAA:	85.08
	E	21.5	4.0				

Scotts Pi: 0.696
Krippendorfs alpha: 0.696
Cohens kappa: 0.7

Figure 58: Validation dataset Confusion Matrix for Land underlying surfaces

Anyhow, the current version of the cloud flag over land surfaces is a small improvement compared to the previous version without the neural net. The previous version had an OAA of only 84.9% while the user accuracy for clear pixels was already 97%. The commission error of clear pixels, with above 27.9% was only slightly bigger compared to the current version, as well as the omission error of cloud pixels which was 0.1% higher (4.1% previous version).

	Sentinel-3 MPC S3-A OLCI Cyclic Performance Report Cycle No. 024	Ref.: S3MPC.ACR.PR.01-024 Issue: 1.0 Date: 30/11/2017 Page: 52
--	---	---

4 Level 2 Water products validation

4.1 [OLCI-L2-CV-210, OLCI-L2-CV-220] – Vicarious calibration of the NIR and VIS bands

There has been no update of the SVC (System Vicarious Calibration) during Cycle 024. Last figures (cycle 17) are considered valid.

4.2 [OLCI-L2WLR-CV-300, OLCI-L2WLR-CV-310, OLCI-L2WLR-CV-32, OLCI-L2WLR-CV-330, OLCI-L2WLR-CV-340, OLCI-L2WLR-CV-350, OLCI-L2WLR-CV-360 and OLCI-L2WLR-CV-370] – Level 2 Water-leaving Reflectance product validation.

Activities done

- ❖ The focus for this time period has been on the None Time Critical (NT) data from September 4th to November 21th 2017. The switch from Near Real Time (NR) to None Time Critical data is motivated but the lack of provision of the NR rolling archive.
- ❖ All extractions and statistics have been regenerated from September 4th onward (rolling archive availability) for WFR and WRR data. The available matchups therefore cover the end of summer to fall situation. Time range available for last processing period covered September 13th to November 4th time period. The overlap is due to the switch between Near Real Time (not regularly provisioned) to None Time Critical data.
- ❖ An MPMF data provision failure has is not yet fully resolved. The amount of available data for routine validation is still limited.
- ❖ Only a few matchups with AERONET-OC stations are available for this time period. These stations are located in the North Pacific (MOBY), Gulf of Mexico (WaveCIS) and Black Sea (Galata and Gloria). Aqua Alta Oceanographic Station hosting AERONET-OC AAOT has return to full operation late October after 5 months of full refurbishment. No Matchups are yet available.
- ❖ To put forward the representativeness of each validation dataset, the number of matchups per stations has been added on standard validation plots. RPD in addition to |RPD| has been added on the plots.

Overall Water-leaving Reflectance performance

Figure 59 and Figure 60 below presents the scatterplots with statistics of OLCI FR and RR versus in situ reflectance computed for the NT dataset. The data considered correspond to the latest processing baseline i.e. including SVC. FR and FR statistics provide consistent results. Table 7 to Table 14 below summarise the statistics over the previous and current reporting.



Sentinel-3 MPC

S3-A OLCI Cyclic Performance Report

Cycle No. 024

Ref.: S3MPC.ACR.PR.01-024
 Issue: 1.0
 Date: 30/11/2017
 Page: 53

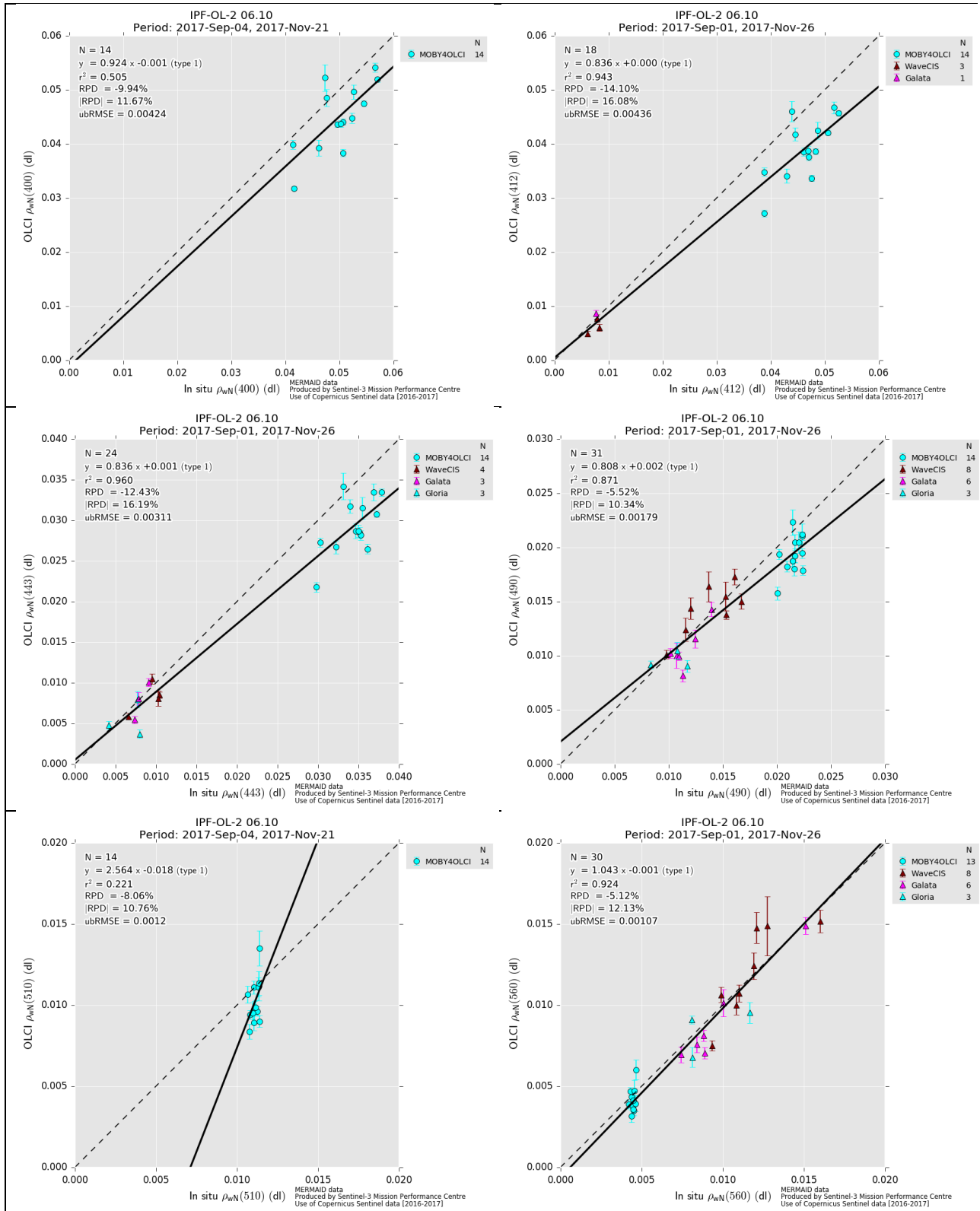


Figure 59: Scatter plots of OLCI versus in situ radiometry (FR data)



Sentinel-3 MPC
S3-A OLCI Cyclic Performance Report
Cycle No. 024

Ref.: S3MPC.ACR.PR.01-024
 Issue: 1.0
 Date: 30/11/2017
 Page: 54

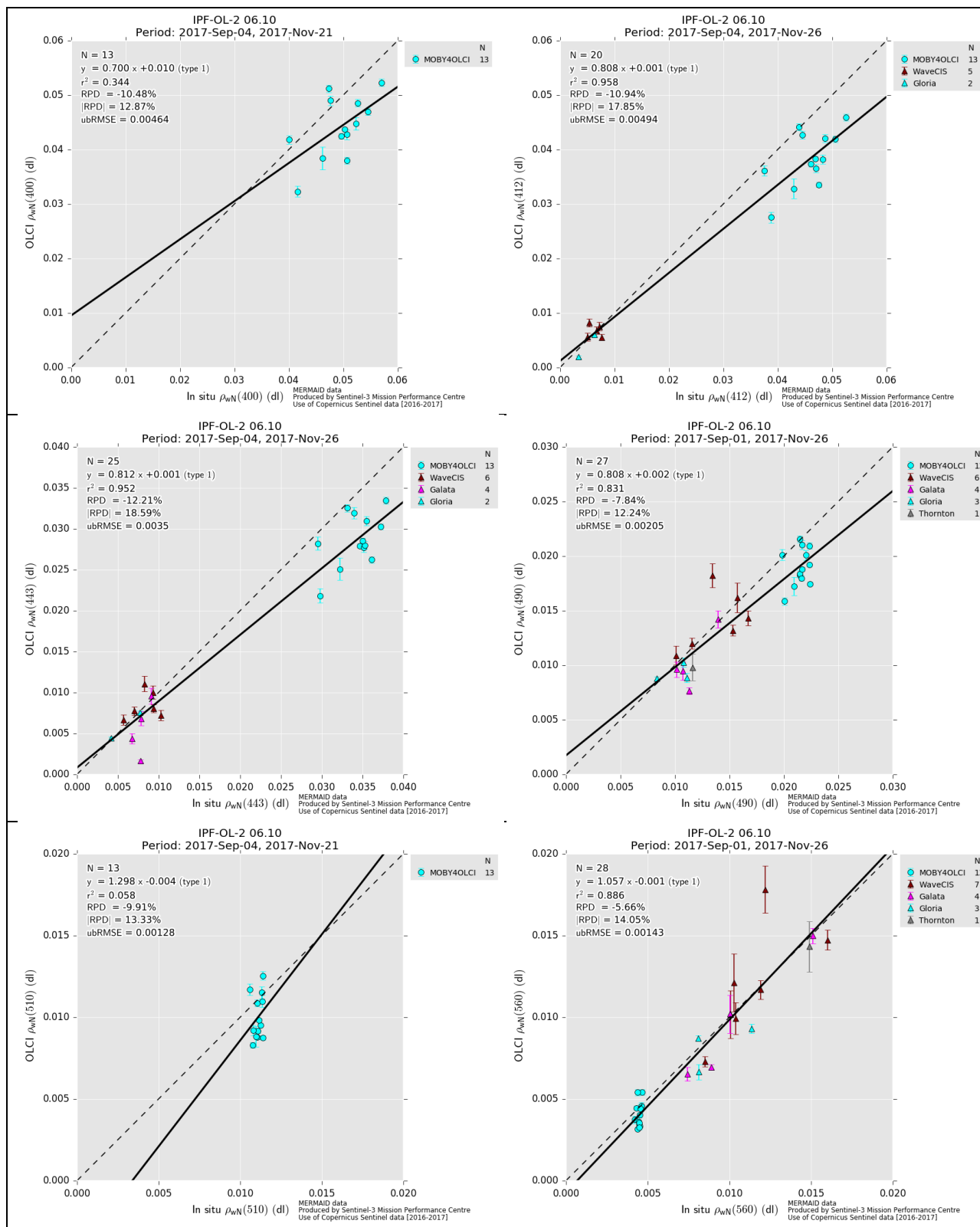


Figure 60: Scatter plots of OLCI versus in situ radiometry (RR data)



Sentinel-3 MPC

S3-A OLCI Cyclic Performance Report

Cycle No. 024

Ref.: S3MPC.ACR.PR.01-024

Issue: 1.0

Date: 30/11/2017

Page: 55

Table 7: FR statistics over December 2016-March 2017 reporting period

lambda	N	RPD	RPD	MAD	RMSE	slope	int.	r2
412	25	70,55%	77,47%	0,0055	0,0071	0,9486	0,0061	0,6787
443	25	43,34%	44,27%	0,0045	0,0056	1,1251	0,0028	0,9037
490	24	28,53%	28,53%	0,0048	0,0059	1,1634	0,0016	0,9611
510	2	31,69%	31,69%	0,0091	0,0093	2,0459	-0,0207	1,0000
560	17	15,44%	16,95%	0,0037	0,0052	1,1350	0,0003	0,9655
665	25	10,56%	34,24%	0,0010	0,0032	1,3661	-0,0013	0,9236

Table 8: FR statistics over February 2017-April 2017 reporting period

lambda	N	RPD	RPD	MAD	RMSE	slope	int.	r2
412	60	88.15%	93.77%	0.0052	0.0066	1.0404	0.0048	0.6176
443	60	46.70%	50.43%	0.0038	0.0049	1.1195	0.0026	0.8046
490	59	31.38%	32.56%	0.0039	0.0046	1.1397	0.0019	0.9263
510	19	27.06%	27.06%	0.0050	0.0055	1.1474	0.0021	0.9486
560	53	13.42%	16.58%	0.0024	0.0035	1.1281	0.0001	0.9379
665	51	1.02%	29.79%	0.0000	0.0012	1.0202	-0.0001	0.7892

Table 9 FR statistics over April 2017-June 2017 reporting period

lambda	N	RPD	RPD	MAD	RMSE	slope	intercept	r2
400	2	17.9%	17.9%	0.0088	0.0100	-2.3992	0.1784	1.0000
412	15	66.3%	66.3%	0.0055	0.0062	1.0618	0.0046	0.9611
443	15	36.7%	37.0%	0.0037	0.0044	1.1107	0.0023	0.9454
490	20	32.1%	32.3%	0.0038	0.0044	1.0153	0.0036	0.8224
510	10	35.9%	35.9%	0.0045	0.0048	0.8626	0.0064	0.7505
560	21	17.0%	21.9%	0.0020	0.0034	1.0925	0.0006	0.9205

Table 10: FR statistics over May 1st to July 10th reporting period

lambda	N	RPD	RPD	MAD	RMSE	slope	intercept	r2
412	35	30.5%	38.2%	0.0025	0.0060	0.9699	0.0033	0.9364
443	43	25.2%	32.9%	0.0023	0.0061	1.0444	0.0012	0.9546
490	52	15.2%	22.2%	0.0020	0.0055	1.0462	0.0007	0.9756
510	21	24.1%	24.9%	0.0026	0.0039	1.1577	0.0004	0.9946
560	52	2.4%	11.1%	0.0004	0.0045	1.0196	-0.0002	0.9701
665	32	-6.9%	17.7%	-0.0002	0.0023	0.9830	-0.0001	0.8423

Table 11: FR statistics over the current reporting period (July 11th to August 23rd)

lambda	N	RPD	RPD	MAD	RMSE	slope	intercept	r2
412	19	18.0%	32.2%	0.0008	0.0066	1.0075	0.0006	0.9346
443	24	10.2%	24.1%	0.0012	0.0072	1.0752	-0.0012	0.9524
490	32	8.0%	18.8%	0.0012	0.0062	1.0504	-0.0005	0.9743
510	10	17.6%	19.3%	0.0011	0.0014	0.9560	0.0014	0.6316
560	32	-1.0%	13.0%	-0.0002	0.0055	1.0179	-0.0008	0.9618
665	22	-10.8%	18.4%	-0.0004	0.0027	0.9028	0.0003	0.7552

Table 12: FR Statistics over the current reporting period (July 1st to September 7th)

lambda	N	RPD	RPD	MAD	RMSE	slope	intercept	r2
412	6	81.5%	95.7%	0.0017	0.0064	0.6848	0.0063	0.7589
443	7	31.6%	49.7%	0.0003	0.0041	0.8661	0.0026	0.9401
490	11	5.8%	20.1%	0.0003	0.0022	0.9909	0.0004	0.9818
510	3	13.0%	20.2%	0.0009	0.0015	1.1289	0.0000	0.1477
560	11	-4.5%	12.9%	-0.0009	0.0021	0.9270	0.0004	0.9784
665	7	-22.5%	22.5%	-0.0008	0.0009	1.0191	-0.0009	0.9618

Table 13: FR Statistics over the current reporting period (September 13th to November 4th)

lambda	N	RPD	RPD	MAD	RMSE	slope	intercept	r2
400	0	None	None	None	None	None	None	None
412	7	-2.1%	32.6%	0.0006	0.0049	2.7334	-0.0157	0.7427
443	10	-2.2%	22.0%	-0.0001	0.0030	1.4778	-0.0043	0.5329
490	16	0.4%	11.9%	0.0000	0.0019	0.9282	0.0008	0.5065
560	16	-5.9%	13.7%	-0.0004	0.0014	1.0994	-0.0013	0.8961
665	4	-24.8%	24.8%	-0.0003	0.0003	1.0428	-0.0004	0.9994

Table 14; Statistics over the current reporting period (September 1st to November 26th), FR (top) and RR (bottom).

lambda	N	RPD	RPD	MAD	RMSE	slope	intercept	r2
400	14	-9.9%	11.7%	-0.0049	0.0065	0.9241	-0.0012	0.5049
412	18	-14.1%	16.1%	-0.0057	0.0072	0.8357	0.0005	0.9427
443	24	-12.4%	16.2%	-0.0033	0.0046	0.8364	0.0005	0.9605
490	31	-5.5%	10.3%	-0.0011	0.0021	0.8081	0.0021	0.8710
510	14	-8.1%	10.8%	-0.0009	0.0015	2.5638	-0.0183	0.2207
560	30	-5.1%	12.1%	-0.0003	0.0011	1.0427	-0.0006	0.9236

lambda	N	RPD	RPD	MAD	RMSE	slope	intercept	r2
400	13	-10.5%	12.9%	-0.0053	0.0070	0.6998	0.0095	0.3440
412	20	-10.9%	17.8%	-0.0049	0.0070	0.8083	0.0012	0.9581
443	25	-12.2%	18.6%	-0.0032	0.0048	0.8116	0.0008	0.9525
490	27	-7.8%	12.2%	-0.0015	0.0025	0.8077	0.0017	0.8308
510	13	-9.9%	13.3%	-0.0011	0.0017	1.2975	-0.0044	0.0579
560	28	-5.7%	14.0%	-0.0003	0.0015	1.0567	-0.0007	0.8855

Figure 61 below shows illustrate the lack of both is situ and OLCI data on the current reporting period..

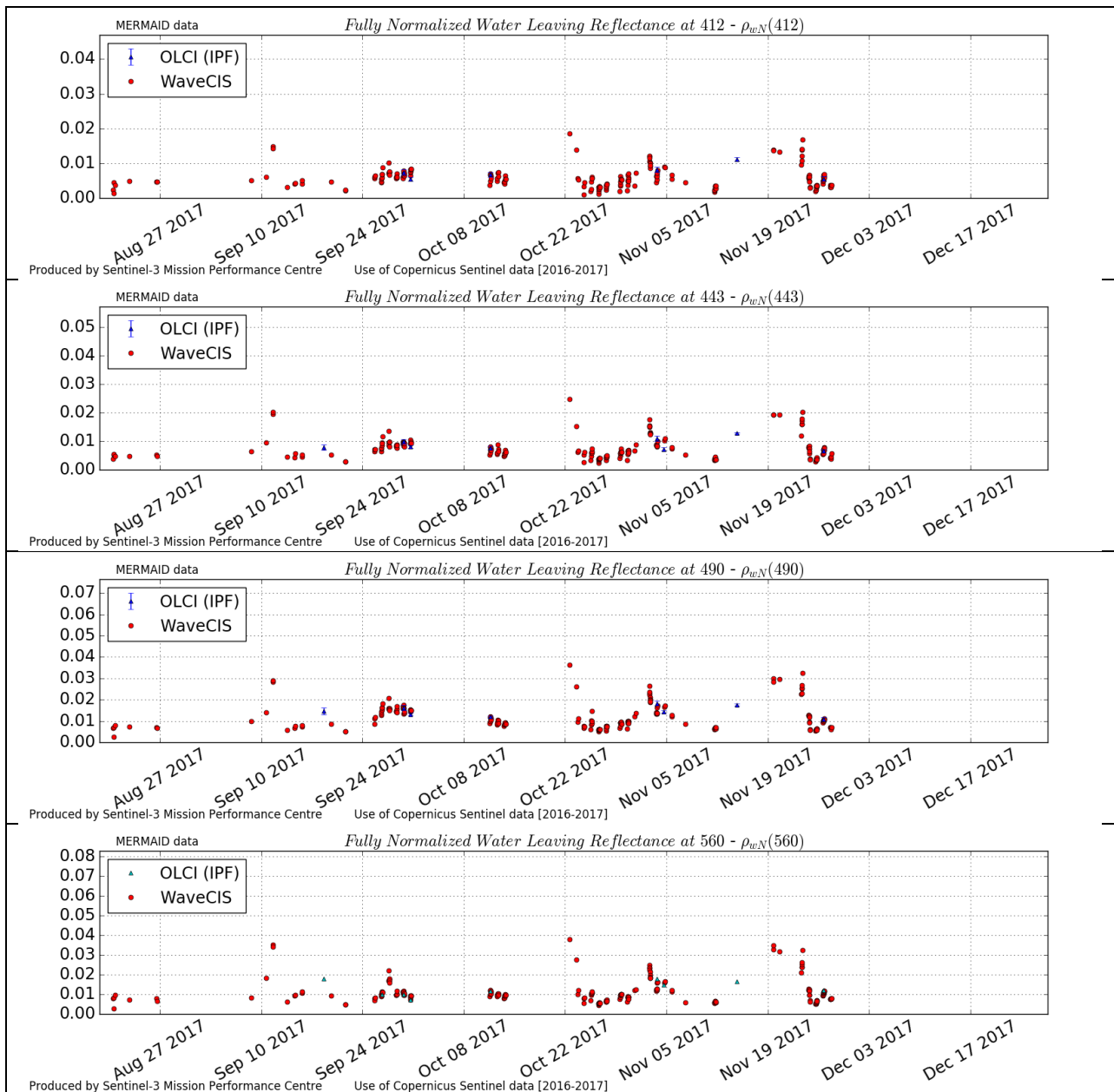


Figure 61: OLCI and AERONET-OC radiometric time series on WaveCIS station.

4.3 [OLCI-L2WLR-CV-510 & 520] – Cloud Masking & Surface Classification for Water Products

A quantitative validation of the current OLCI cloud flag was conducted using a dedicated pixel collection (PixBox dataset). After significant efforts had been made to improve the OLCI cloud masking over water and land and the new version had been put to production for the S3VT and at the PDGS in July. The processing of an OLCI validation dataset has been finished in October. Afterwards, the PixBox dataset had been used to make a quantitative validation of the OLCI cloud mask.

For the PixBox validation dataset 10000 pixels have been collected. The collected pixels are well distributed temporally and spatially.

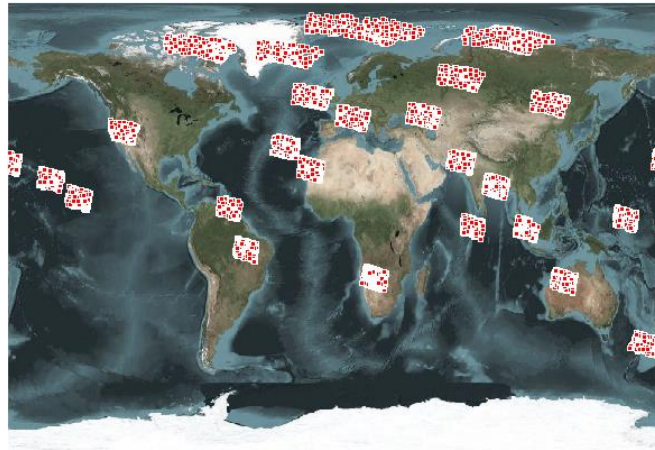


Figure 62: spatial distribution of the PixBox validation dataset samples

The collection distinguishes between different cloud types which have been combined to one cloud category for the validation. The same has been done for the OLCI cloud flags (CLOUD, CLOUD_ambiguous, CLOUD_Margin), as there is no straight forward correlation between the collected cloud types and the three OLCI cloud flags.

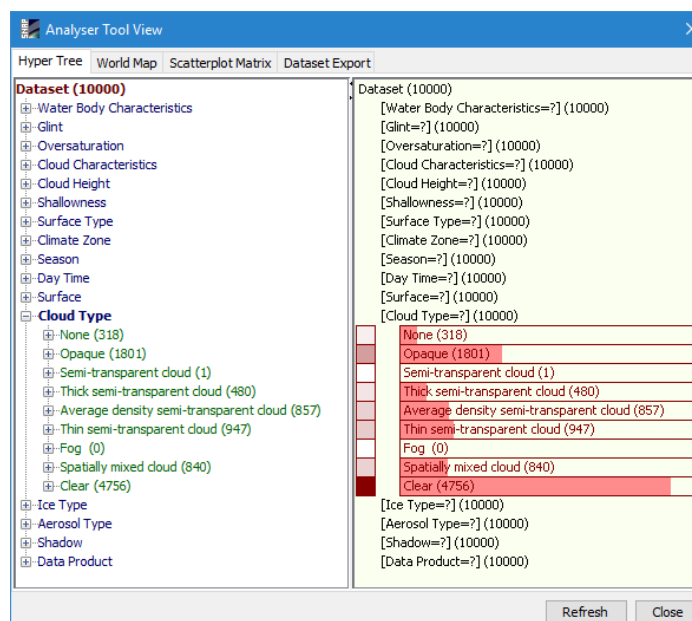


Figure 63: PixBox validation dataset samples Cloudiness classification overview

This means there have only been two classes been used in the validation process. These classes are clear and cloud. For the PixBox dataset the three semi-transparent cloud classes as well as opaque pixels have been combined to the class **“Cloud”** while the collected clear pixels represent the **“Clear”** observations. The PixBox dataset is represented as **“In-Situ Database”** in the confusion matrices and plotted on horizontal axis. The OLCI cloud flags (CLOUD, CLOUD_AMBIGUOUS and CLOUD_MARGIN) have been combined the class **“CLOUD”** and all pixels not affected by any of these flags has been classified as **“CLEAR”**. The extracted OLCI pixels are represented as **“OLCI FR”** and plotted on the vertical axis.

The validation of the cloud flag over all surfaces (land & water) has shown an overall accuracy (OAA) of over 86% and an user accuracy (UA) for clear pixels of over 92%. The level of significance (0.72) is substantial. From the user perspective the cloud flags have a good accuracy in identifying clear observations, but from the producer perspective there is room for improvements, as the producer accuracy (PA) of clear pixels is only a little above 81%. This means, there is a commission error of clear pixels of above 19% and an omission error of cloud pixels of 8.1%.

OLCI LFR cloud val. - all surface (Insitu 1-5 vs CLD Flags)

In-Situ Database

		Class	Clear	Cloud	Sum	U A	E
OLCI FR	CLEAR		3856	330	4186	92.1	7.9
	CLOUD		900	3756	4656	80.7	19.3
	Sum		4756	4086	8842		
	P A		81.1	91.9		OAA:	86.09
	E		18.9	8.1			

Scotts Pi: 0.721

Krippendorfs alpha: 0.721

Cohens kappa: 0.722

Figure 64: Validation dataset Confusion Matrix for all underlying surfaces

Although there is room for improvements, the current version of the cloud flag is a strong improvement compared to the previous version without the neural net. The previous version had an OAA of only 83.6% and a user accuracy for clear pixels of 91%. The commission error of clear pixels, with nearly 23% was also a bit bigger compared to the current version, as well as the omission error of cloud pixels with 8.7%.

When analyzing only water surfaces the accuracies are distributed a bit different. The OOA is a bit higher (87%) while the UA for clear pixels is a lot lower, with only 86.7%. The omission error of cloud pixels

over water is nearly 3% higher (10.9%) compared to all surfaces (8.1%). On the other hand, the commission error of clear pixels decreased over water surfaces nearly 7%.

OLCI WFR cloud val. - water surface (Insitu 1-5 vs CLD Flags)
In-Situ Database

		Class	Clear	Cloud	Sum	U A	E
OLCI FR	CLEAR		1710	263	1973	86.7	13.3
	CLOUD		305	2153	2458	87.6	12.4
	Sum		2015	2416	4431		
	P A		84.9	89.1		OAA:	87.18
	E		15.1	10.9			

Scotts Pi: 0.741
Krippendorfs alpha: 0.741
Cohens kappa: 0.741

Figure 65: Validation dataset Confusion Matrix for Water underlying surfaces

Nevertheless, the current version of the cloud flag over water surfaces is a strong improvement compared to the previous version without the neural net. The previous version had an OAA of only 82.3% and a user accuracy for clear pixels of only 84%. The commission error of clear pixels, with above 18% was also much bigger compared to the current version, as well as the omission error of cloud pixels which was nearly 12% (10.9% current version).

4.4 [OLCI-L2WLR-CV530] Validation of Aerosol Product

4.4.1 Validation by AERONET data

AERONET (AERosol RObotic NETwork) (Holben et al 1998) is a network of ground-based sun photometers which measure atmospheric aerosol properties. The measurement system is a solar-powered CIMEL Electronique 318A spectral radiometer that measures Sun and sky radiances at a number of fixed wavelengths within the visible and near-infrared spectrum. Up to now only a small number of AERONET data, can be used for the validation of OLCI's maritime aerosol products. First, the majority of the AERONET stations are on land, and second, the cloud screened and quality assured (**level 2**) products need some time (several months (up to 12)) to be provided by the resp. station PIs. The AERONET stations, which could be used so far, are plotted in Figure 66. The stations are located close to or on the



Sentinel-3 MPC
S3-A OLCI Cyclic Performance Report
Cycle No. 024

Ref.: S3MPC.ACR.PR.01-024
 Issue: 1.0
 Date: 30/11/2017
 Page: 61

ocean, however, depending on wind direction and atmospheric circulation the impact of the continent cannot be excluded.

We analysed 513 OLCI scenes with respect to be applicable for a comparison with the AERONET measurements, but only a very few fulfilled the criteria for a solid validation. A subset of 146 OLCI observations have been found in temporal and spatial vicinity of one of the indicated AERONET stations as displayed in Figure 66. This sub-set reduces to 74 observations when the criteria of less than 1 hour between AERONET and OLCI observations is applied. But for only 10 of them valid OLCI aerosol products could be extracted, all others are cloud contaminated.

The aerosol optical thickness (T865) and the Angstrom coefficient (A865) as derived from OLCI and AERONET are displayed in Figure 67. The retrieved aerosol optical thicknesses at 865 nm are low between 0.02 and 0.08, which fit in the range of ship-borne and other satellite observations above ocean. The two cases with significant higher OLCI T865 retrievals could be identified to be impacted by undetected clouds and sun-glint. The Ångström coefficients derived from OLCI and AERONET measurements deviate much more (Figure 67, right). Actually, the Ångström coefficient, could not be verified by AERONET measurements, however, A865 might be very sensitive to disturbances from continental aerosols, coastal waters and cirrus.

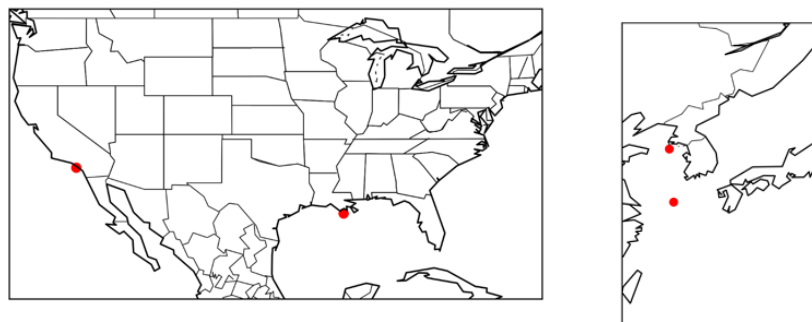


Figure 66 Map of the U.S.A., showing the used AERONET-OC stations (red bullets)

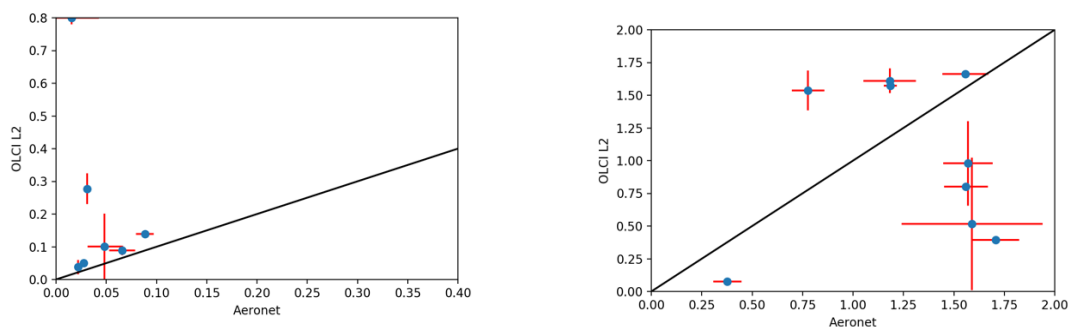


Figure 67: Comparison of AERONET and OLCI derived aerosol optical thickness at 865 nm (left) and Ångström coefficient (right); match-ups only taken when no clouds in the vicinity of 30 km.

We further analysed the 513 OLCI images with respect to AERONET measurements taken during ship cruises (MAN). Here only 3 cases fulfilled the criteria for a solid validation (less than 1 hour between AERONET and OLCI measurements, and no OLCI flags indicating a reduced product confidence). The aerosol optical thickness T865 are fairly comparable between OLCI and AERONET retrievals, the Ångström coefficient is not comparable (Figure 69).

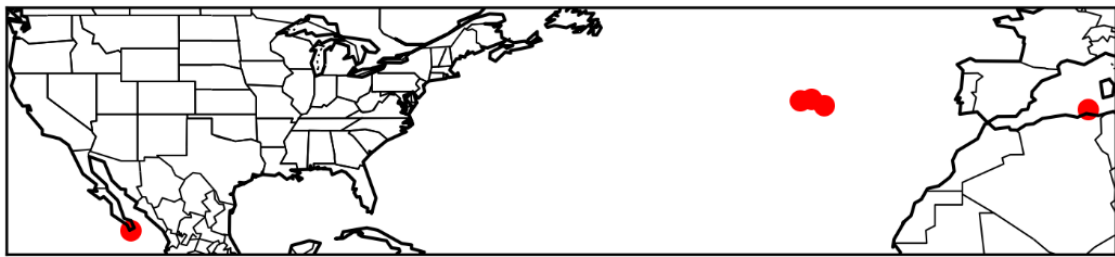


Figure 68: AERONET MAN measurements from ship cruises (red bullets).

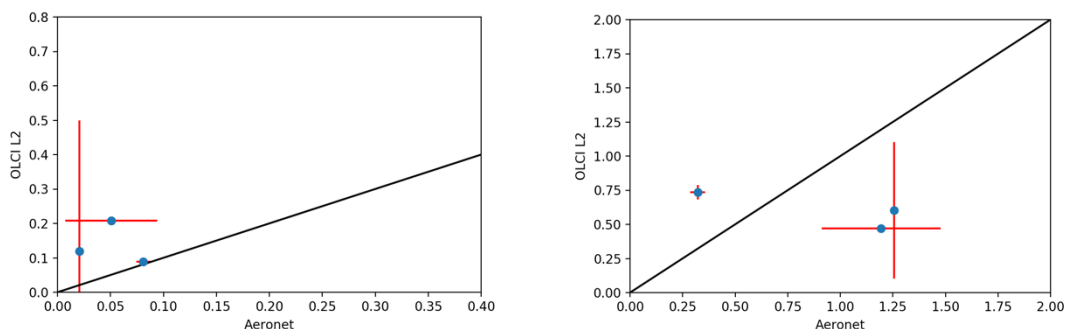



Figure 69: Comparison of AERONET and OLCI derived aerosol optical thickness at 865 nm (left) and Ångström coefficient (right). The error bars indicate the variability within a 30 km radius (OLCI) the and a 1h window (AERONET)

To conclude the results of this investigation, we can state, that the aerosol properties, estimated within the atmospheric correction process, are consistent with AERONET measurements. But, the number of match-ups between OLCI and AERONET observations are too low, in order to draw general conclusions yet. Further investigations are necessary to make a rigorous and solid validation. We learnt, that a careful selection of the match-ups is a prerequisite of a successful validation, considering cloud contamination, especially by thin cirrus.

With the beginning of routine production of OLCI's maritime L2 products in June 2017, the number of match-ups will grow rapidly. We know, that most AERONET level 2 data can be provided within few month after acquisition (up to 12 months), thus with the beginning of 2018 for June 2017.

	<p>Sentinel-3 MPC</p> <p>S3-A OLCI Cyclic Performance Report</p> <p>Cycle No. 024</p>	<p>Ref.: S3MPC.ACR.PR.01-024</p> <p>Issue: 1.0</p> <p>Date: 30/11/2017</p> <p>Page: 63</p>
--	--	--

4.4.2 Verification by OLCI image analysis

Beside the validation of the OLCI aerosol products by means of AERONET observations, we analysed a number of OLCI scenes with respect to consistent retrievals of T865 and A865. We selected only OLCI scenes which are taken and processed after August 2017, to investigate products already affected by the update of the OLCI ground processor.

For the analysis, we discuss the OLCI products T865 and A865, derived from a scene taken at the 6th of October 2017 above the Pacific Ocean (Figure 70). The OLCI scene has been selected to demonstrate the impact of cirrus clouds on the retrieval of aerosol properties.

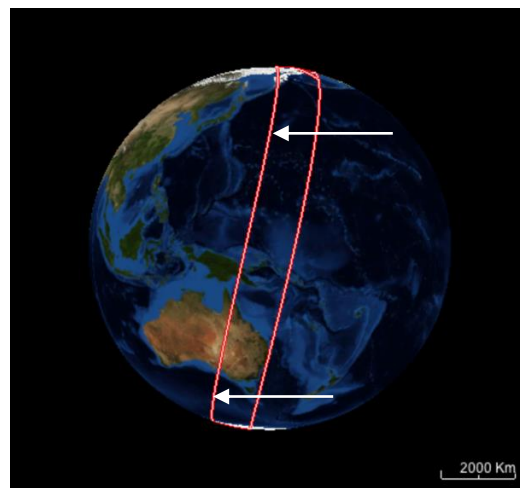


Figure 70: OLCI scene from 6th of October 2017, arrows are pointing to study areas

The selected sub-scene in the southern Pacific Ocean, south of Tasmania, has been analysed with respect to T865 and A865 (Figure 71). An area with high aerosol optical thickness values between 0.5 and 0.75 has been identified. The colour image of T865 shows clearly the regions of different aerosol optical thicknesses. The area of low T865 are quite homogeneous with values lower than 0.1, which have been observed during ship cruises in remote ocean regions. The different areas of T865 values could be explained by cirrus contamination. We calculated the ratio of radiances at 753 nm and 761 nm, which nicely shows structures which are related to cirrus (Figure 70, middle). The profile plot of the ratio L_{761}/L_{753} contains the information of the O₂ absorption and the modified optical path length due to atmospheric molecules, aerosols and clouds. The lower ratio values are correlated to the high T865 values, which are caused by the increased backscattering by the higher elevated cirrus particles lowering the ratio of the O₂ absorption (L_{761}) and the reference channel (L_{753}).

The Ångström coefficient A865 also varies highly in the considered region between 0.2 and 1.5, which covers realistically maritime aerosols, but also cirrus clouds (Figure 71, A865 plot). T865 and A865 are also correlated along the studied profile, which further supports the hypothesis that undetected thin cirrus might be the cause of the high derived T865 values. The low Ångström coefficient values A865 correspond to the high T865 values, which could be explained only by unrealistic high maritime aerosol optical thickness values or cirrus particles.

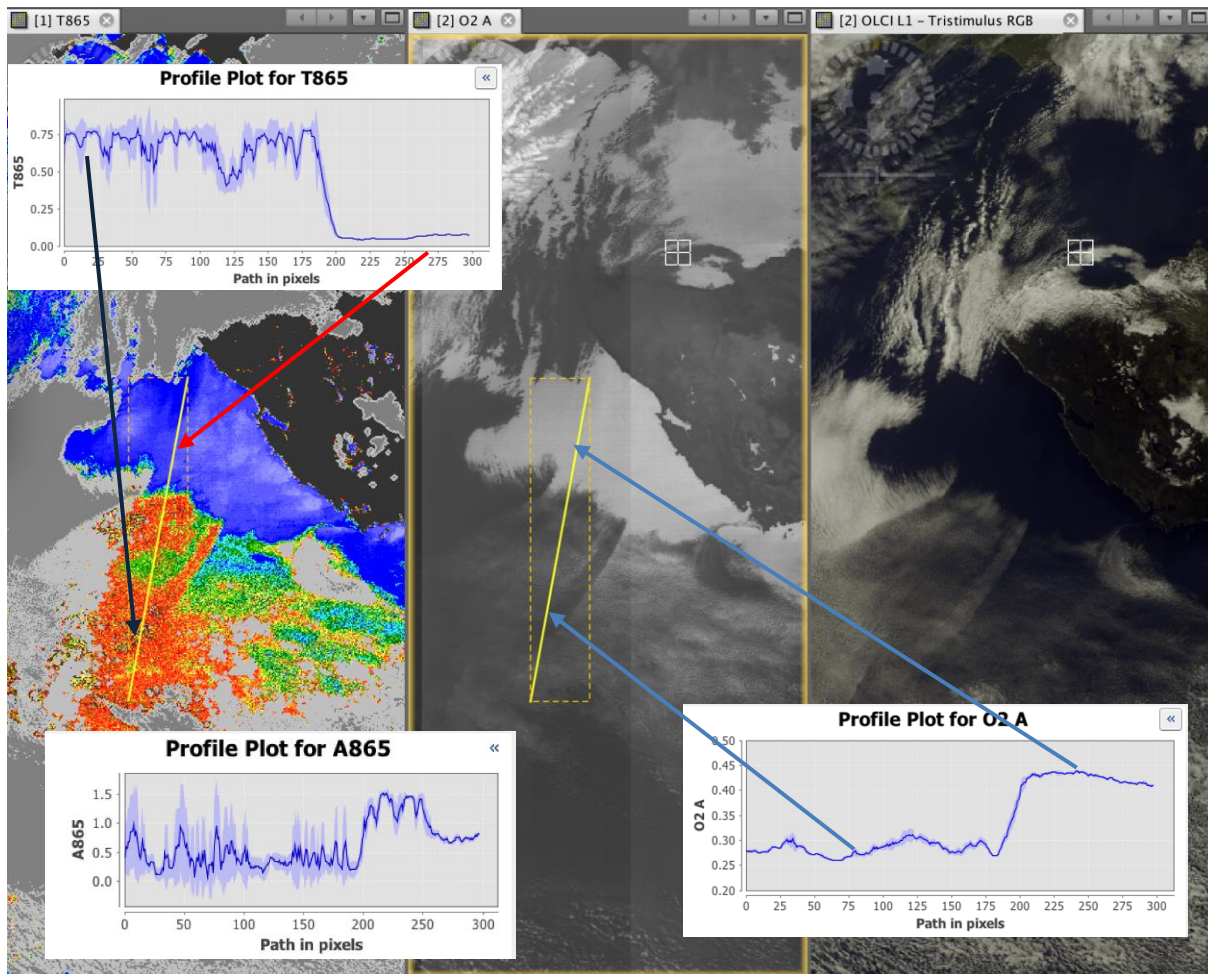


Figure 71: OLCI scene from 6th of October 2017 and derived properties: T865 (left), O2 A-band (middle), RGB-image (right); profile plots of T865, A865 and O2 A-band (L761/L753); see also Figure 70 for geo-location.

A second region in the northern Pacific to further analyse areas with high and variable T865 and A865 values has been selected (Figure 72). There are two distinct areas, but with less pronounced differences in T865 and A865 as described in the upper case. The lower values of T865 are around 0.2 with increasing values beyond 0.5. The corresponding O2 A-band measurements, expressed via the ratio L761/L7653, show higher values in the region with lower T865 and lower values in the area with higher T865 values. This is expected when cirrus is suspected as the reason for higher T865 values. This case shows less pronounced the effect of cirrus in the T865 and O2 A-band values, but might be still measurable.

Conclusions and Recommendations

The main sources of misinterpretation corresponding with unrealistic high aerosol optical thickness T865 and Ångström A865 values are due to glint and clouds. The glint area is well captured and flagged, and

the cloud mask does identify most of the clouds. However, cirrus is not always well detected and leads to wrong estimations of the aerosol properties and thus to failures in the atmospheric correction. Measurements of the O2 A-band, in this study expressed as the ratio of L761/L753, seem to be a clear indicator of the existence of cirrus clouds. Thus, an identification of cirrus and further on a consideration can be achieved by developing appropriate procedures which use consequently the information of the O2 A-band measurements.

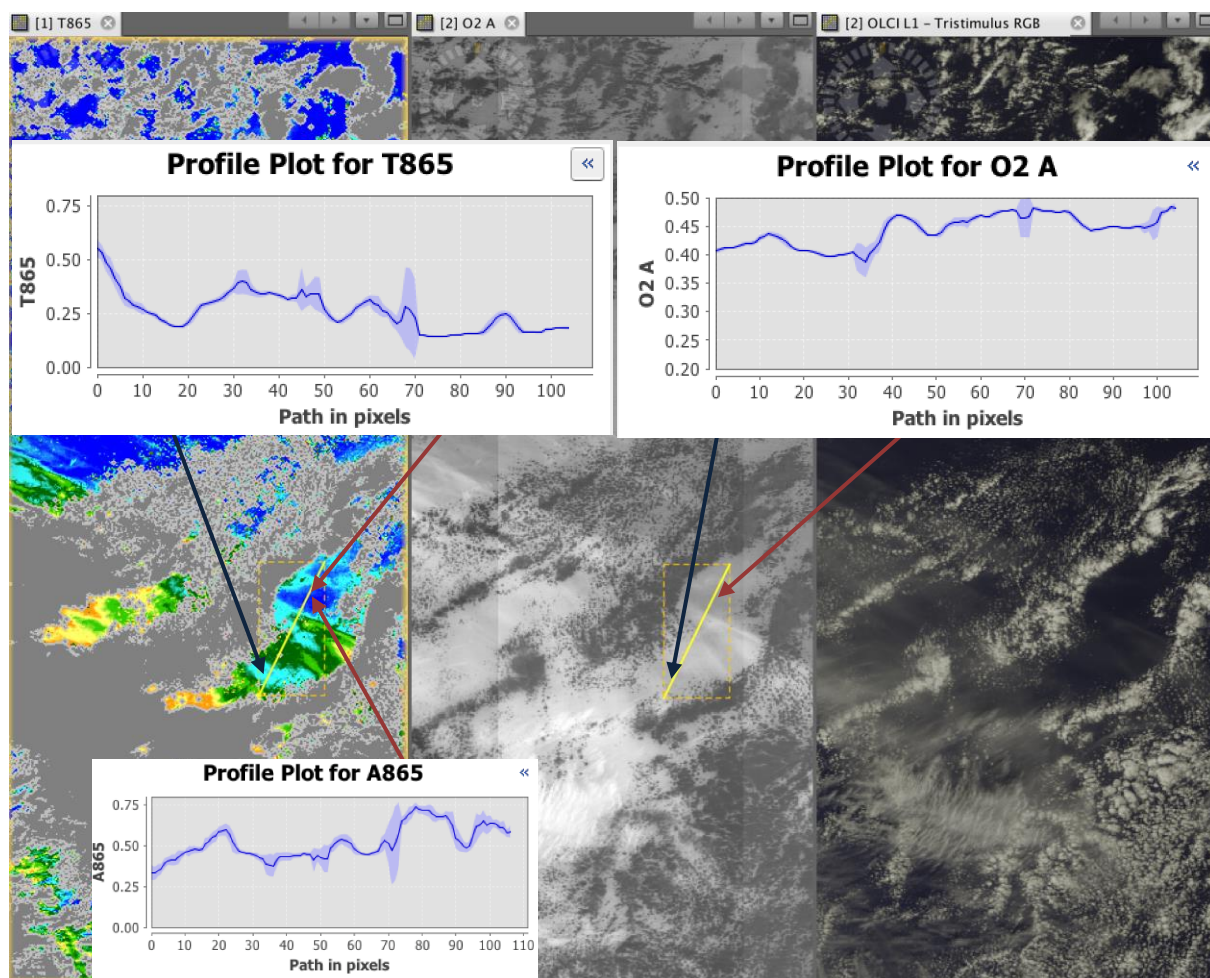



Figure 72: OLCI scene from 6th of October 2017 and derived properties: T865 (left), O2 A-band (middle), RGB-image (right); profile plots of T865, O2 A-band (L761/L753);

4.4.3 References:

- Holben, B. N., et al., AERONET—A federated instrument network and data archive for aerosol characterization, Remote Sens. Environ.,66, 1–16, 1998.),
- Smirnov, A., Holben, B.N., Slutsker, I., Giles, D.M., McClain, C.R., Eck, T.F., Sakerin, S.M., Macke, A., Croot, P., Zibordi, G., Quinn, P.K., Sciare, J., Kinne, S., Harvey, M., Smyth, T.J., Piketh, S., Zielinski, T., Proshutinsky, A., Goes, J.I., Nelson, N.B., Larouche, P., Radionov, V.F., Goloub, P., Krishna Moorthy, K., Matarrese, R., Robertson, E.J., Jourdin, F., 2009. Maritime aerosol network


	<p>Sentinel-3 MPC</p> <p>S3-A OLCI Cyclic Performance Report</p> <p>Cycle No. 024</p>	<p>Ref.: S3MPC.ACR.PR.01-024</p> <p>Issue: 1.0</p> <p>Date: 30/11/2017</p> <p>Page: 66</p>
--	--	--

as a component of aerosol robotic network. J. Geophys. Res. 114, 1–10, <http://dx.doi.org/10.1029/2008JD011257>.

- G.Zibordi, B.Holben, I.Slutsker, D.Giles, D.D’Alimonte, F.Mélin, J.-F. Berthon, D. Vandemark, H.Feng, G.Schuster, B.Fabbri, S.Kaitala, J.Seppälä. AERONET-OC: a network for the validation of Ocean Color primary radiometric products. Journal of Atmospheric and Oceanic Technology, 26, 1634-1651, 2009.

4.5 [OLCI-L2WLR-CV-380] Development of calibration, product and science algorithms

There has been no new developments on **calibration, product and science algorithms** during the cycle

	<p>Sentinel-3 MPC</p> <p>S3-A OLCI Cyclic Performance Report</p> <p>Cycle No. 024</p>	<p>Ref.: S3MPC.ACR.PR.01-024</p> <p>Issue: 1.0</p> <p>Date: 30/11/2017</p> <p>Page: 67</p>
--	--	--

5 Validation of Integrated Water Vapour over Land & Water

5.1 Highlight

A verification of the IWV (integrated water vapour, resp. total column water vapour) product quality is achieved via visual inspection.

Further, a quantitative validation of the IWV retrievals over land has been performed, whereby a high correlation between IWV products derived from OLCI, GNSS data and AERONET resp. has been found.

5.2 Preface

The OLCI L2 IWV processor distinguishes between ocean and land surfaces, as described in the ATBD. The validation of the IWV product above land is performed via comparisons with ground based GNSS (Ware et al 2000) measurements and water vapor from AERONET (Holben et al 1998). Above ocean a first verification using AERONET has been performed, but the amount of matchups is very low. Sentinel 3 MWR measurements (*rad_liquid_wate r_01_plrm_ku*) will be used in future which are available since June 2017 however no validation information about this product is available yet.

5.3 Visible Inspection

A number of OLCI L2 IWV scenes have been inspected and analysed. For the ocean retrieval a scene above the Pacific Ocean is shown and discussed herein in some detail. OLCI IWV is compared with the IWV from ECMWF analysis. It should be mentioned, that water vapour above Ocean from Model-analysis is already of high quality, in particular it is bias free. Small spatial features may be not be reflected precisely, but the total amount is correct in average.

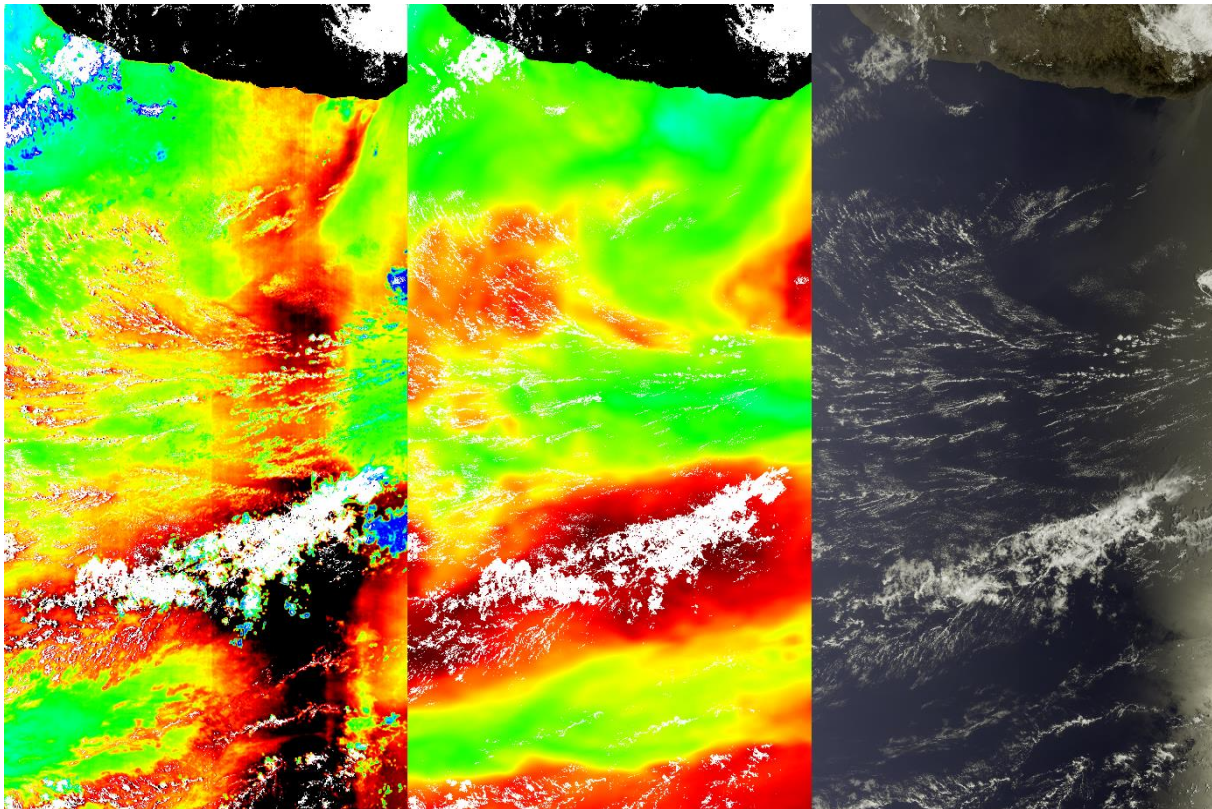


Figure 73: I WV, estimated from OLCI at 03/March/2017, above the Pacific, south-west of Baja California. Left: I WV from OLCI, middle: ECMWF Analysis, right: RGB. The color coding ranges from 0 kg/m² (blue) to 60 kg/m² (black). Land and clouds are masked out (black and white, resp.)

The most prominent artefact is the huge overestimation of water vapour in the transition between the glint and off glint region. Further, an underestimation (blue spots on the east side) above undetected clouds is perceivable. All other features are well represented and the amounts are in well agreement. For the land retrieval a scene above North America is shown in Figure 74. A prominent atmospheric feature, atmospheric lee waves, has been found above the Great Plains in the lee of the Rocky Mountains (see Figure 75 and Figure 76). A comparison of the I WV fields as derived from OLCI observations and from ECMWF analysis shows, that the main structures of the I WV field is caught by ECMWF analysis, but small scale features are missing (compare Figure 75 middle and right). Such as before mentioned lee waves.

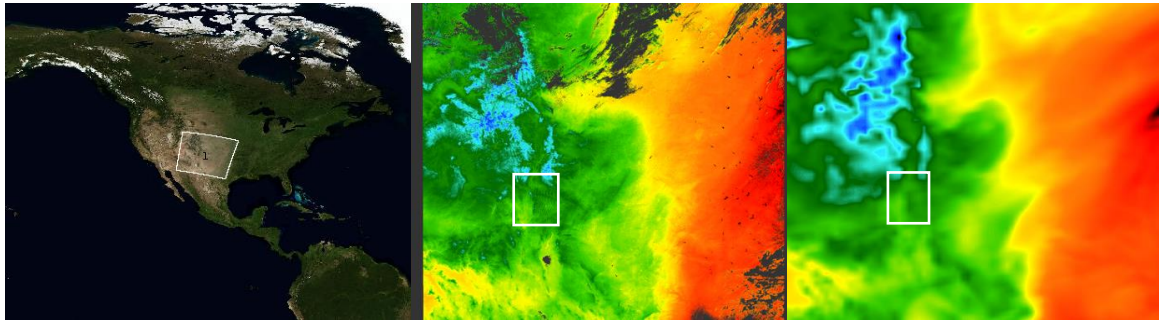


Figure 74: OLCI scene from 19.10.2016 (19:05), marked in the white box (left), IWV derived from OLCI (middle), IWV estimated by ECMWF (right)

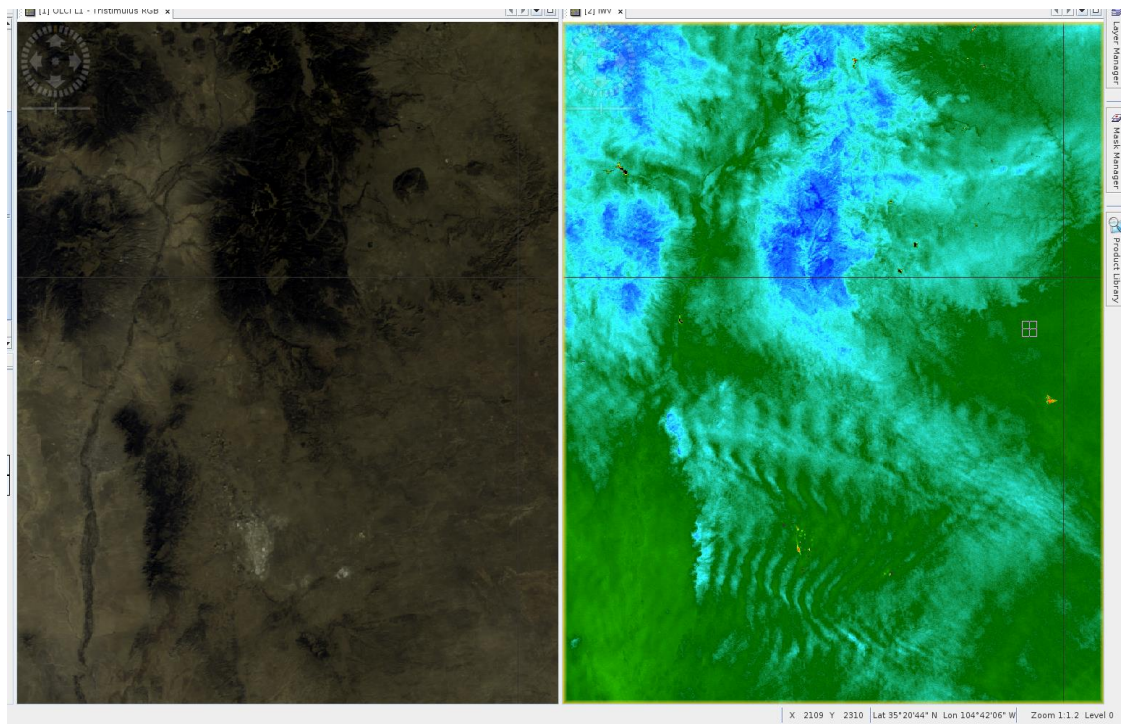


Figure 75: OLCI scene from 19.10.2016 (19:05), IWV product of marked scene (left, see also figure 4), RGB image of a selected region above the Rocky Mountains (left), IWV field above the Rocky Mountains, see the lee waves in lower part of the image (right)

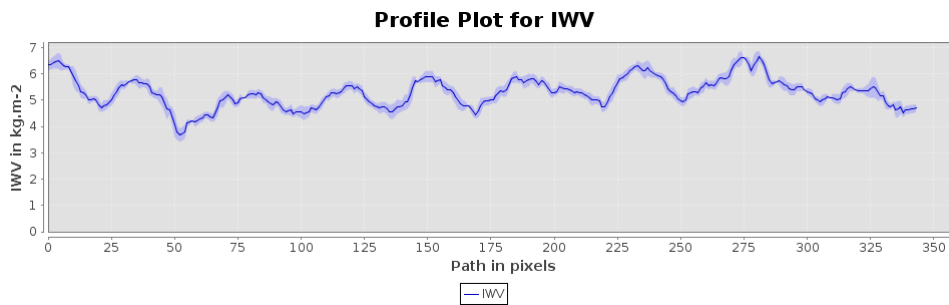


Figure 76 : Transect along the lee waves (see Figure 75).

5.4 Quantitative validation using GNSS

The OLCI IWV above land surface product is validated via global GNSS (Ware et al. 2000) measurements (see Figure 77). Hundreds of OLCI scenes within the period of October 2016 to October 2017 have been analysed. The OLCI observations comprise very humid air-masses at the equator and very dry and cold atmospheres above the Rocky Mountains and polar regions. The scenes cover high and low elevations. Only OLCI measurements are taken for the validation which are cloud-free in an area of about 10 km around the GNSS stations. For the cloud detection, the standard L2 cloud-mask has been applied.

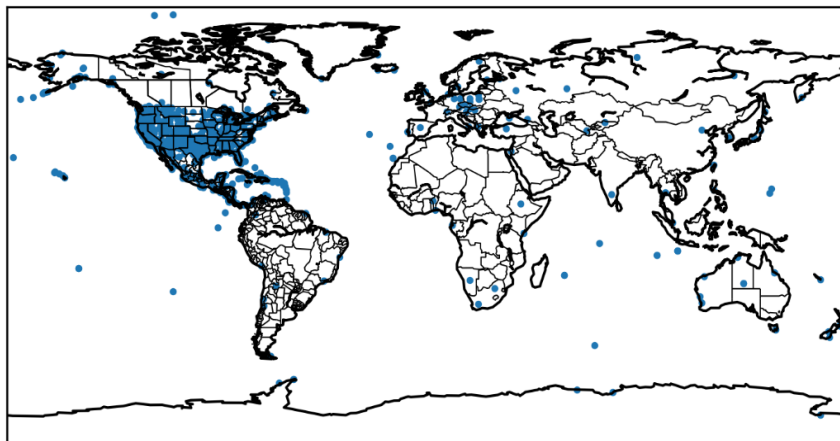


Figure 77: Position of the GNSS stations used for the IWV validation.

The validation of the TCWC product shows a high agreement between the OLCI and the GNSS derived IWV (Figure 78). The correlation between both quantities is 0.93. The root-mean-squared-difference (rmsd) is 3.9 kg/m². However, there is a systematic overestimation by OLCI of 14%, which leads to a bias of 2.0 kg/m². The bias corrected rmsd is 3.1 kg/m². Those results do not reach the quality, which already have been achieved from MERIS, so far.

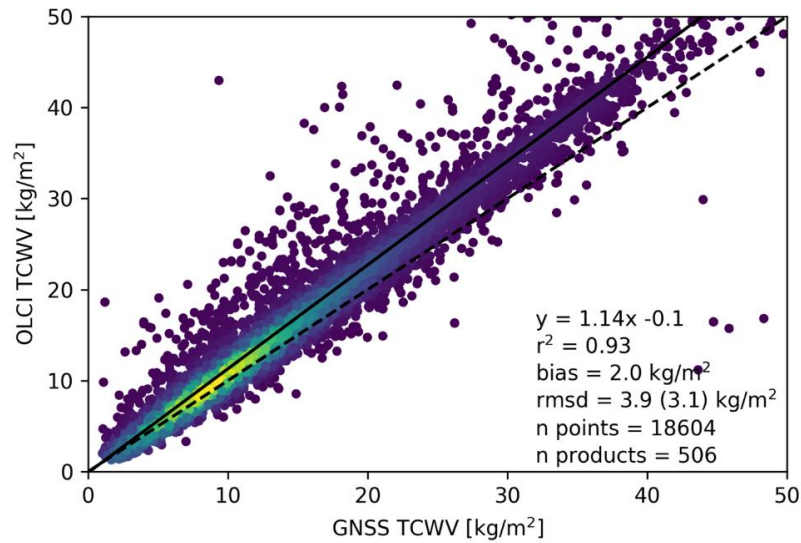


Figure 78: Scatter plot of the IWV products, derived from OLCI and from GNSS measurements.

The wet bias of OLCI and of MERIS IWV retrievals might indicate an insufficient description of the measurements within the retrieval. The reasons could be either insufficient description of the instrument, in particular the stray-light correction, or the absorption of atmospheric water vapour.

A selection of only US GNSS stations and the comparison with OLCI IWV retrievals achieve slightly better results (Figure 79). The correlation between GNSS and OLCI IWV is 0.92. The root-mean-squared-difference is 2.3 kg/m². However, there is still a systematic overestimation by OLCI of 10%, which leads to a bias of 1.1 kg/m². The bias corrected rmsd is 1.9 kg/m². Comparable results have been achieved from MERIS data as well.

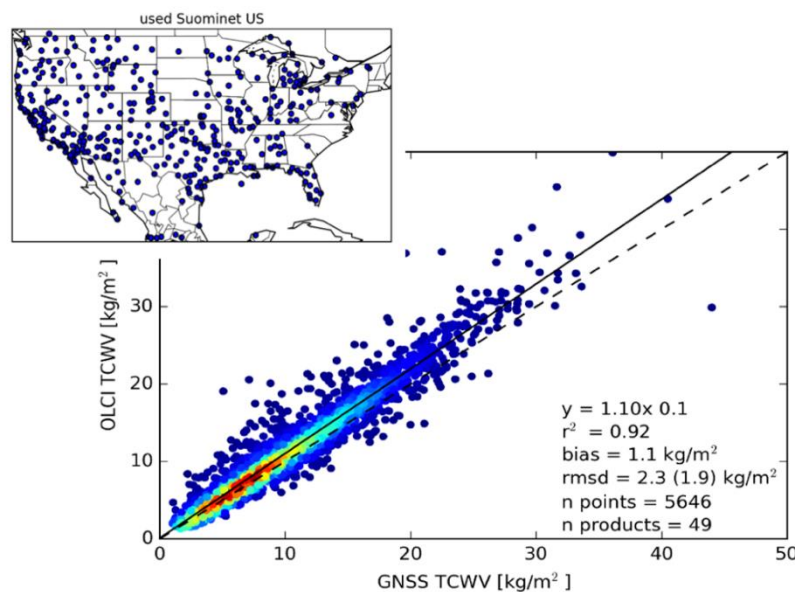


Figure 79: Scatter plot of the IWV products, derived from OLCI and from US GNSS measurements.

The better validation results of the selected US data may be caused by more solid retrieval at the US stations (Background: for the retrieval of water vapour from GPS, the profile of temperature and the surface pressure must be known to a certain accuracy. This data may be more uncertain outside the US)

5.5 Quantitative validation using AERONET IWV Retrievals – Land

A further step in the validation process is realised by using IWV retrieval, derived from spectral AERONET measurements. The used AERONET (Holben et al 1998.) match-ups are displayed in Figure 80. Solely *level2* products have been used which are cloud screened and quality assured.

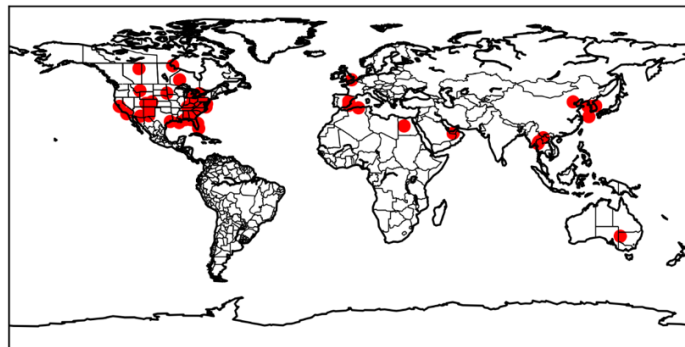


Figure 80: Position of the AERONET stations used for the IWV validation.

The comparison of the TCWC AERONET product shows a high agreement with the OLCI IWV product (Figure 81). The correlation between both quantities is 0.98. The root-mean-squared-difference is 3.0 kg/m². However, there is a systematic overestimation by OLCI of 15%, which leads to a bias of 2.0 kg/m². The bias corrected *rmsd* is 1.7 kg/m². The bias is comparable with the GNSS comparisons, the *rmsd* is smaller, probably due to the more rigid cloud detection inherent of the AERONET level 2.

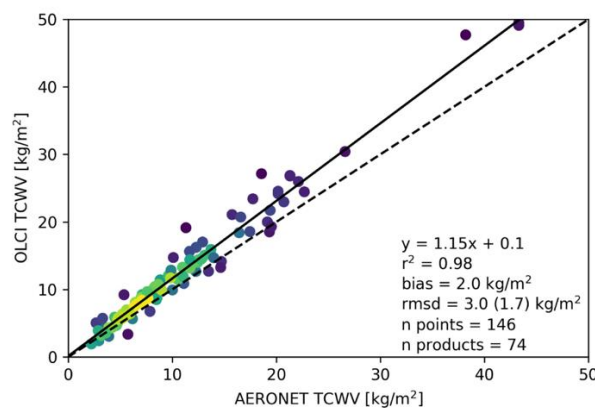



Figure 81 OLCI IWV against AERONET IWV retrievals for the sites displayed in Figure 80.

	<p>Sentinel-3 MPC</p> <p>S3-A OLCI Cyclic Performance Report</p> <p>Cycle No. 024</p>	<p>Ref.: S3MPC.ACR.PR.01-024</p> <p>Issue: 1.0</p> <p>Date: 30/11/2017</p> <p>Page: 73</p>
--	--	--

Perez-Ramirez et al. (2014) found a dry-bias of AERONET IWV product with respect to GNSS and MW based IWV retrievals of 5-6%. Even though only three ARM sites have been used in this study, we conclude that the wet-bias of the OLCI IWV might not be caused by spectroscopic deficiencies. However, we further will inspect the corresponding differences in the transmission functions, because the AERONET IWV retrieval is based on HITRAN 2000 and the OLCI procedure on HITRAN 2008.

5.6 Validation by AERONET IWV Retrievals – Ocean

Selected marine AERONET sites have been used to further inspect the quality of the OLCI IWV above ocean product. The position of the AERONET sites are displayed in Figure 82.



Figure 82: Position of the AERONET sites used for the IWV validation.

The comparison of the TCWC AERONET product shows a fair agreement with the OLCI IWV product (figure 12). The correlation between both quantities is 0.87 and thus lower than for the comparison above land. The root-mean-squared-difference is 6.1 kg/m^2 . Again, a systematic overestimation by OLCI of 9% has been found. The bias corrected rmsd is 3.8 kg/m^2 . Even though the number of data points is very low (4 data points only), the general findings are as in the previous investigations.

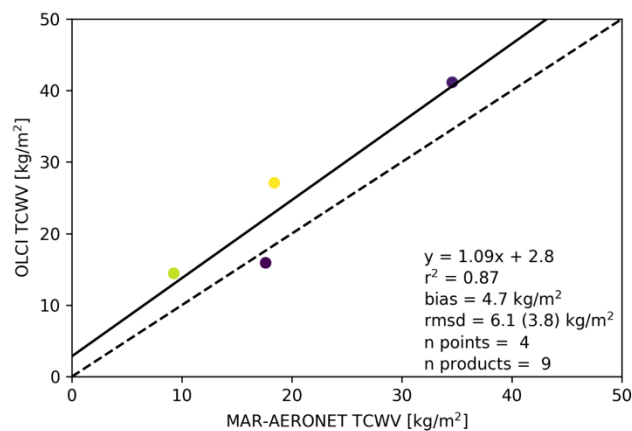



Figure 83: OLCI IWV against AERONET IWV retrievals for the sites displayed in Figure 82.

5.7 Summary and recommendations

- ❖ The validation exercise of the OLCI IWV product has been successful. It demonstrates that the product is of high quality for retrievals above land surfaces. But there is a systematic overestimation of 10% to 15%. The few marine AERONET co-locations indicate also a wet bias for the ocean retrievals. There could be several reasons for the found systematic overestimation, deficits in spectroscopy or over-corrected stray-light on the instrument. Both hypotheses need deeper investigation.
- ❖ Retrievals above ocean show an overestimation in transition zones between glint and off glint. This is a clear deficit of the description of the scattering-absorption interaction. A redesigned algorithm may be necessary to overcome this.
- ❖ The IWV OLCI algorithm uses measurements at 865, 885 and 900 nm, while the bands at 935 and 1040 nm are not used. We expect better results, in particular less noise, if all relevant bands are used.


5.8 References:

- Holben, B. N., et al., AERONET—A federated instrument network and data archive for aerosol characterization, *Remote Sens. Environ.*,66, 1–16, 1998.)
- Pérez-Ramírez, D., D. N. Whiteman, A. Smirnov, H. Lyamani, B. N. Holben, R. Pinker, M. Andrade, and L. Alados- Arboledas (2014), Evaluation of AERONET precipitable water vapor versus microwave radiometry, GPS, and radiosondes at ARM sites, *J. Geophys. Res. Atmos.*, 119, 9596–9613, doi:10.1002/2014JD021730
- Smirnov, A., Holben, B.N., Slutsker, I., Giles, D.M., McClain, C.R., Eck, T.F., Sakerin, S.M., Macke, A., Croot, P., Zibordi, G., Quinn, P.K., Sciare, J., Kinne, S., Harvey, M., Smyth, T.J., Piketh, S., Zielinski, T., Proshutinsky, A., Goes, J.I., Nelson, N.B., Larouche, P., Radionov, V.F., Goloub, P.,

	<p>Sentinel-3 MPC</p> <p>S3-A OLCI Cyclic Performance Report</p> <p>Cycle No. 024</p>	<p>Ref.: S3MPC.ACR.PR.01-024</p> <p>Issue: 1.0</p> <p>Date: 30/11/2017</p> <p>Page: 75</p>
--	--	--

Krishna Moorthy, K., Matarrese, R., Robertson, E.J., Jourdin, F., 2009. Maritime aerosol network as a component of aerosol robotic network. *J. Geophys. Res.* 114, 1–10, <http://dx.doi.org/10.1029/2008JD011257>.


- Ware, R. H., D. W. Fulker, S. A. Stein, D. N. Anderson, S. K. Avery, R. D. Clark, K. K. Droegemeier, J. P. Kuettnner, J. B. Minster, and S. Sorooshian (2000), SuomiNet: A real-time national GPS network for atmospheric research and education, *Bull. Am. Meteorol. Soc.*, 81(4), 677–694.
- Zibordi G., B. Holben, I. Slutsker, D. Giles, D. D'Alimonte, F. Mélin, J.-F. Berthon, D. Vandemark, H. Feng, G. Schuster, B. Fabbri, S. Kaitala, J. Seppälä. AERONET-OC: a network for the validation of Ocean Color primary radiometric products. *Journal of Atmospheric and Oceanic Technology*, 26, 1634-1651, 2009.

 <p>The logo for the Sentinel-3 Mission Performance Centre. It features a central blue satellite icon with the text 'SENTINEL 3' above it. To the left, there are four small square images: a sunset, a satellite view of Earth, a person, and a green checkmark. To the right, the text 'Mission Performance Centre' is written vertically.</p>	<p>Sentinel-3 MPC</p> <p>S3-A OLCI Cyclic Performance Report</p> <p>Cycle No. 024</p>	<p>Ref.: S3MPC.ACR.PR.01-024</p> <p>Issue: 1.0</p> <p>Date: 30/11/2017</p> <p>Page: 76</p>
--	--	--

6 Level 2 SYN products validation

6.1 [SYN-L2-CV-100]

There has been no new result during the cycle. Last figures (cycle 21) are considered valid

	<p>Sentinel-3 MPC</p> <p>S3-A OLCI Cyclic Performance Report</p> <p>Cycle No. 024</p>	<p>Ref.: S3MPC.ACR.PR.01-024</p> <p>Issue: 1.0</p> <p>Date: 30/11/2017</p> <p>Page: 77</p>
--	--	--

7 Events

Three OLCI Radiometric Calibration Sequences have been acquired during Cycle 024:

- ❖ S01 sequence (diffuser 1) on 05/11/2017 04:10 to 04:11 (absolute orbit 8946)
- ❖ S04 sequence (diffuser 1) on 22/11/2017 08:33 to 08:35 (absolute orbit 9191)
- ❖ S05 sequence (diffuser 2) on 22/11/2017 10:14 to 10:16 (absolute orbit 9192)


Two Spectral Calibration acquisitions have been acquired during Cycle 024.

One S02/S03:

- ❖ S02 sequence (diffuser 1) on 04/11/2017 11:20 to 11:22 (absolute orbit 8936)
- ❖ S03 sequence (Erbium doped diffuser) on 04/11/2017 13:01 to 13:03 (absolute orbit 8937)

And one S09 (Fraunhofer lines)

- ❖ S09 sequence on 04/11/2017 08:59 to 09:04 (absolute orbit 8935)

	Sentinel-3 MPC S3-A OLCI Cyclic Performance Report Cycle No. 024	Ref.: S3MPC.ACR.PR.01-024 Issue: 1.0 Date: 30/11/2017 Page: 78
--	---	---

8 Appendix A

Other reports related to the Optical mission are:

- ❖ S3-A SLSTR Cyclic Performance Report, Cycle No. 024 (ref. S3MPC.RAL.PR.02-024)

All Cyclic Performance Reports are available on MPC pages in Sentinel Online website, at:
<https://sentinel.esa.int>

End of document